THREE-DIMENSION COLE-COLE MODEL INVERSION OF INDUCED POLARIZATION DATA BASED ON REGULARIZED CONJUGATE GRADIENT METHOD

by

Zhengwei Xu

A dissertation submitted to the faculty of
The University of Utah
in partial fulfillment of the requirements for the degree of

Doctor of Philosophy

in

Geophysics

Department of Geology and Geophysics

The University of Utah

May 2013

Copyright © Zhengwei Xu 2013

All Rights Reserved

The University of Utah Graduate School

STATEMENT OF DISSERTATION APPROVAL

The dissertation of **Zhengwei Xu**

has been approved by the following supervisory committee members:

Michael S. Zhdanov	, Chair	**03/12/2013** Date Approved
Erich U. Petersen	, Member	**03/05/2013** Date Approved
Michael Thorne	, Member	**03/05/2013** Date Approved
Alexander V. Gribenko	, Member	**03/07/2013** Date Approved
Martin Cuma	, Member	**03/08/2013** Date Approved

and by **D. Kip Solomon**, Chair of the Department of **Geology and Geophysics**

and by Donna M. White, Interim Dean of The Graduate School.

ABSTRACT

Modeling of induced polarization (IP) phenomena is important for developing effective methods for remote sensing of subsurface geology and is widely used in mineral exploration. However, the quantitative interpretation of IP data in a complex 3D environment is still a challenging problem of applied geophysics.

In this dissertation I use the regularized conjugate gradient method to determine the 3D distribution of the four parameters of the Cole-Cole model based on surface induced polarization (IP) data. This method takes into account the nonlinear nature of both electromagnetic induction (EMI) and IP phenomena. The solution of the 3D IP inverse problem is based on the regularized smooth inversion only. The method was tested on synthetic models with DC conductivity, intrinsic chargeability, time constant, and relaxation parameters, and it was also applied to the practical 3D IP survey data. I demonstrate that the four parameters of the Cole-Cole model, DC electrical resistivity, ρ_0 (or electrical conductivity $\sigma_0 = 1/\rho_0$), chargeability, η; time constant, τ; and the relaxation parameter, C, can be recovered from the observed IP data simultaneously.

There are four Cole-Cole parameters involved in the inversion, in other words, within each cell, there are DC conductivity (σ_0), chargeability (η), time parameters (τ), and relaxation parameters (C) compared to conductivity only, used in EM only inversion.

In addition to more inversion parameters used in IP survey, dipole-dipole configuration which requires more sources and receivers. One the other hand, calculating

Green tensor and Fréchet matrix time consuming and storing them requires a lot of memory. So, I develop parallel computation using MATLAB parallel tool to speed up the calculation.

To my parents and my wife Yun

TABLE OF CONTENTS

LIST OF TABLES

ACKNOWLEDGMENTS

Before I joined the Consortium for Electromagnetic Modeling and Inversion (CEMI) at the Department of Geology and Geophysics, University of Utah, I did not have much knowledge about geophysics and geology, especially for EM, which requires good math skills. There are too many people to be grateful to. Therefore, I will be lengthy here and brief elsewhere.

I am deeply indebted to my advisor and committee chair, Dr. Michael Zhdanov, who made this work possible and shared his vast knowledge of EM and inversion, for giving me a chance to work under his guidance and who ultimately led me down an academic path. Dr. Le Wan not only sacrificed a lot of time to answer the problems of the EM theoretical part for me, but also had many invaluable insights into the application of my research in the real world, and forced me to look beyond my work. Dr. Alexander V. Gribenko, who is an EM expert in my mind, provided helpful guidance on this work, and answered numerous questions about programming and inversion techniques.

I would also like to thank my committee member, Dr. Michael Thorne, who has improved my knowledge about seismology and helped me to understand the stories behind qualification and how to prepare them. Dr. Erich Petersen helped me connect geophysics with geology, especially for minerals and rocks. Finally, I am grateful for my committee member, Dr. Martin Cuma, who forced me to learn much about the principles and skills of parallel computation, which I used to improve my code.

I am also thankful to Dr. Masashi Endo and Dr. Xiaojun Liu for sharing the techniques to calculate the sensitivities, discussing technical problems related to this thesis research and addressing questions related to practical geophysical situations and providing invaluable program codes to refer to this research. I would also like to thank Mrs. Kim Atwater. Without her help, I could not have gotten the salary certifications to apply for Medicaid for my baby.

Finally, my families provided empathy and encouragement along the way. I feel especially grateful to my mother, without her upbringing, I could not have achieved today's success. My father, as a senior geophysicist, gave me a lot of suggestions to help me prepare for qualification. I also thank my parents-in-law. Without them taking care of my baby, I could not have focused on my work completely. Most of all, I would like to thank my wife, Yun, who supported my Ph.D work, which was a long journey from the beginning to the end.

CHAPTER 1

INTRODUCTION

Geophysical exploration is the most significant technique in the discovery of ground water, archelology, geothermal, mineral, and petroleum exploration. Geophysics is applicable to a wide variety of geologic problems. For example, some physical parameters that can be measured are conductivity (electromagnetic), velocity (seismic), magnetic susceptibility (magnetic), and density (gravity).

This dissertation focuses on using land-based controlled source inductive electromagnetic techniques for detecting anomalies in the subsurface. This method uses some form of transmitters to generate the electromagnetic field, which propagates outward from the transmitter and is modified by the electrical properties of the surrounding media.

The electromagnetic data observed in a geophysical survey generally reflect two phenomena: (1) electromagnetic induction (EMI) in the earth, and (2) induced polarization (IP) effects related to the relaxation of polarized charges in rock formations. The EMI effect can be simulated by the solution of electromagnetic (EM) field equations in the geoelectical model characterized by frequency independent conductivity.

Polarization is usually based on models with frequency dependent conductivity distribution. Two of the most popular methods are the Cole-Cole relaxation model (Cole

and Cole, 1941) (Cole and Cole, 1941) and GEMTIP model (Zhdanov, 2008). These two models have been used in a number of publications for the interpretation of IP data. The parameters of the conductivity relaxation model can be used for discrimination of the different types of rock formations, which is an important goal in mineral and petroleum exploration.

The quantitative interpretation of IP data in a complex 3D environment is a very challenging problem because it is complicated by coupling with the EMI effects. Many algorithms presented by the authors are based upon a linear forward modeling for the IP response. However, linear forward modeling ignores the nonlinear effects. Cole-Cole parameters can be recovered relatively accurately by using a linear inversion based on nonlinear forward modeling. In this dissertation, I develop a technique for 3D nonlinear inversion of IP data based on the Cole-Cole relaxation model, especially for multi-transmitter configuration.

Another goal of this dissertation is to develop a parallel computation code for speeding up the nonlinear inversion of IP data, which can be applied to multitransmitter data set. The main difficulty with multitransmitter data inversion is that, in principle, this observation system requires significantly more time for modeling and inversion of the observed data than fixed transmitter system.

The dissertation is organized as follows. Chapter 2 gives the fundamental mechanism that causes the IP phenomena within rock formation. Chapter 3 provides the technique for forward simulation of EM field based on the Cole-Cole relaxation model. In Chapter 4, a new rigorous inversion method is developed to realize inverse distribution of the four parameters of the Cole-Cole model, DC conductivity (σ_0), chargeability (η),

time parameter (τ), and relaxation parameter (C). How to calculate the Fréchet matrix is one of the key points that will be introduced in the Chapter 4 in this dissertation. Synthetic models that are tested to see whether the inversion algorithm can recover the value and position of four Cole-Cole parameters accurately, stably or not and analysis of sensitivity are addressed in Chapter 5. Finally, in the Chapter 6, I move to process the practical (real) 3D IP survey data.

CHAPTER 2

FOUNDATIONS OF THE INDUCED POLARIZATION METHOD

2.1 IP Effect in Rocks and Minerals

Induced polarization is a current-stimulated electrical phenomenon observed as delayed voltage response in earth materials. It has practical importance as a method of prospecting buried mineral deposits and to an minor extent in groundwater search in the subsurface.

The principal phenomenon of induced polarization happens in any material that exhibits conduction by current-induced electron (charge) transfer reaction between electrolyte and metallic-luster minerals or rocks (Bleil, 1953). In general, pure water is an insulating dielectric material with higher dielectric permittivity and conductivity. When water enters the pore system of a rock, the higher dielectric permittivity and higher electrical conductivity of the water dominate the composite electrical properties of the water-rock system (Olhoeft, 1985). During the time of the original current flow, presumably some energy storage took place in the material. There are two ways to describe this chemical energy storage. The first effect is known as membrane or electrolytic polarization, which is the result of variations in the mobility of ions in electrolyte throughout the rock structure within which there is no metallic minerals are

present. The second effect is known as electrode polarization or overvoltage, which is the result of variation between ions and electronic conductivity where metallic mineral are present.

2.1.1 Membrane Polarization

Membrane polarization is the predominating factor in most rocks, occurring when pore space is too narrow to be passed through by ionic current flow. In other words, membrane polarization can be present, even though no current flows, when unsatisfied charges in clays or on cleavage faces or edges of layered and fibrous minerals attract a diffuse cloud of positive ions (Sumner, 1976). Most of the electric current that passes through unmineralized rock is carried by the electrolyte in fractures and pore spaces since adjacent rock forming minerals are very poor conductors of electricity. Most rock minerals have a net negative charge at the interface between the rock surface and electrolytic fluid within the pores, because of crystal structure of minerals. Consequently positive ions are attracted toward, negative repelled from, this interface. Then the viscosity of the bound layer of water is significantly higher than the viscosity of free water. As an ion moves through a narrow spot in a pore structure (Fig 2.1 top panel), the contained water is more viscous, slowing the ions. Secondly, the positive ion concentration may extend into the fluid zone to a depth of about 10^{-6} cm. If this is on the order of the width of the pore itself, negative ions will accumulate at one end of the zone and leave the other when a DC potential is applied across it (Telford et al., 1990). There is a variation in ion mobility causing an ion "pile up" on both sides of the pore where ion mobility varies. At the same time, positive ions are attracted toward the surface and

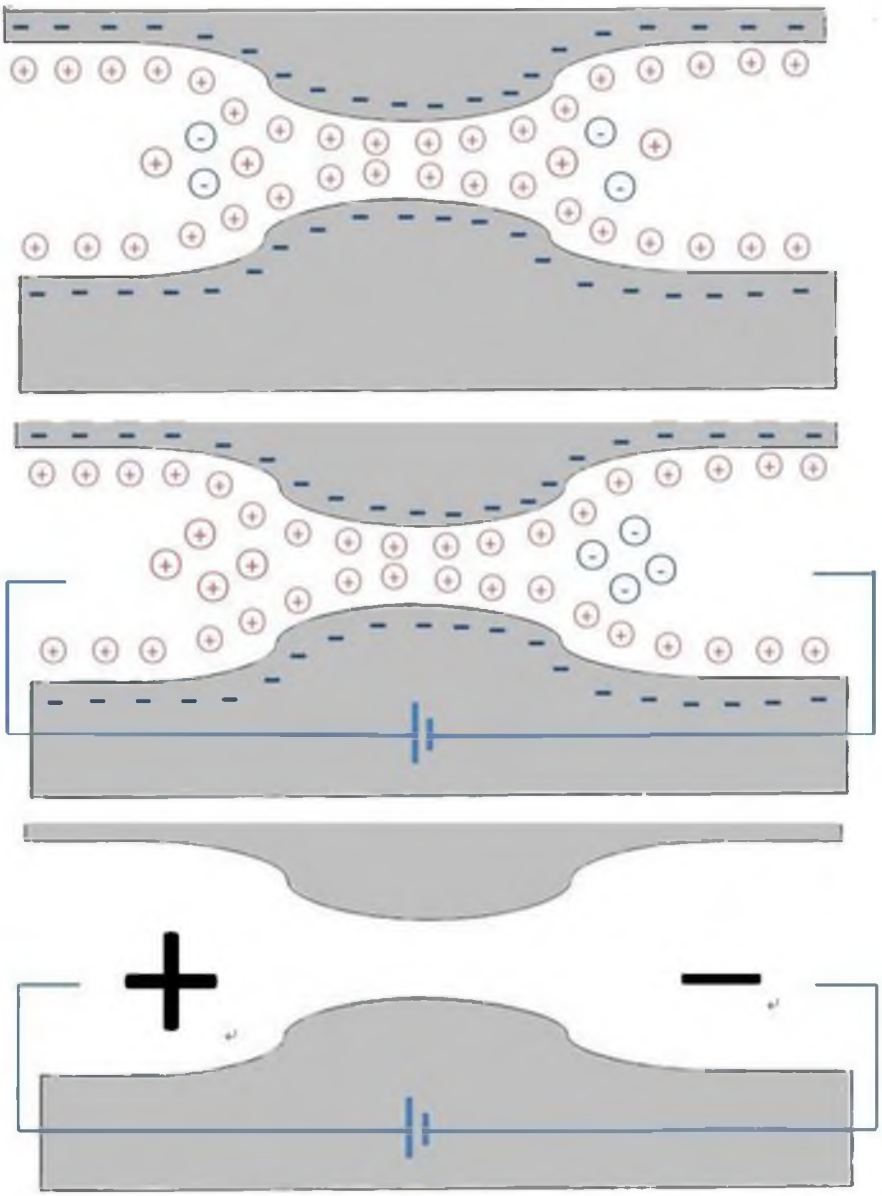

Figure 2.1 Top panel: Illustration of the action of a bound layer of water in sieving the irons as they move through an electrolyte in the pores of a rocks. Middle panel: Ion accumulation forms cation concentrations on the left and anion concentrations on the right. Bottom panel: Finally it forms a net charge dipole (adapted from Sumner, 1976).

negative ions are repelled away from the surface. As time passes, this induced charge increases the polarization at the surface and the current flow continues to decrease. As a result, cation concentrations are formed on one side of the constriction and anion concentrations on the other (Fig 2.1 middle and bottom panel). The ion concentration gradients thus developed oppose current flow and cause a polarized effect. If the current flow is terminated, these induced polarization charges will return to their normal positions under the influence of their own electromotive forces. This transient flow of charged ions will be measured as a voltage that exists after the applied voltage and current are terminated, but decays to zero rapidly.

The membrane polarization is often found in the clay minerals that have very small passageways between sheet structures. The magnitude of polarization does not increase steadily with the clay mineral concentration, but reaches a maximum and then decreases again. The membrane effect also increases with the salinity of the pore fluid. As a result of these factors, membrane polarization is generally at a maximum in a rock containing clay materials in which the electrolyte has some salinity (Telford et al., 1990). Dirty sands and a few rock types containing fibrous and layered minerals also give rise to membrane polarization effects. These minerals have an abundance of small pore passages and a large exposed surface area.

2.1.2 Electrode Polarization

Being similar in principle to membrane polarization, electrode polarization exists when metallic materials are blocked in the pore and the ionic current flow is converted to electronic current flow at the surface of metallic minerals that are in contact with electrolytic solution. Consequently, very pronounced induced polarization occurs in rocks

that contain an aqueous electrolyte in pore spaces in contact with electronically conducting minerals (Sumner, 1976).

Before current is injected into the ground, there exists the natural double potential difference, which happens on the interface of the electronic conductor and solution (Fig 2.2 top panel). At the boundary between the electrolyte and the metallic mineral, as current flows, charge is transferred across the interface either by reduction if an electron is released from the solid phase to the electrolytic solution, or by oxidation, if an electron is released from the electrolytic solution to the solid phase (Fig 2.2 middle panel). When a force perturbs the charge to create a nonuniform distribution, charge will accumulate at material discontinuities such as grain boundaries or particle edges assuming the charge accumulates at interfaces in very thin layers compared to the scale of inhomogeneity (Olhoeft, 1985). When current is caused to flow through such an interface, the oxidation process at one face and the reduction process at another face usually does not require the same energy, which means the speed of the two processes are different. The potential gradient will happen at the face where the process is relatively slow since the current must be conserved. In physical chemistry, this effect is known as overvoltage. The overvoltage is the extra potential energy required to initiate an electro-chemical process, particularly an electron-transfer reaction. It is mainly a potential due to the oxidation-reduction reaction (Siegel and King, 1970), and to a lesser extent a solution concentration gradient at the interface. Overvoltage is the greatest at the interfaces where the chemical activity is largest, where the mode of conduction also changes from ionic in the electrolyte to electronic in the solid. At low currents, the overvoltage is observed to be proportional to the electric current density. The overvoltage at an interface may differ,

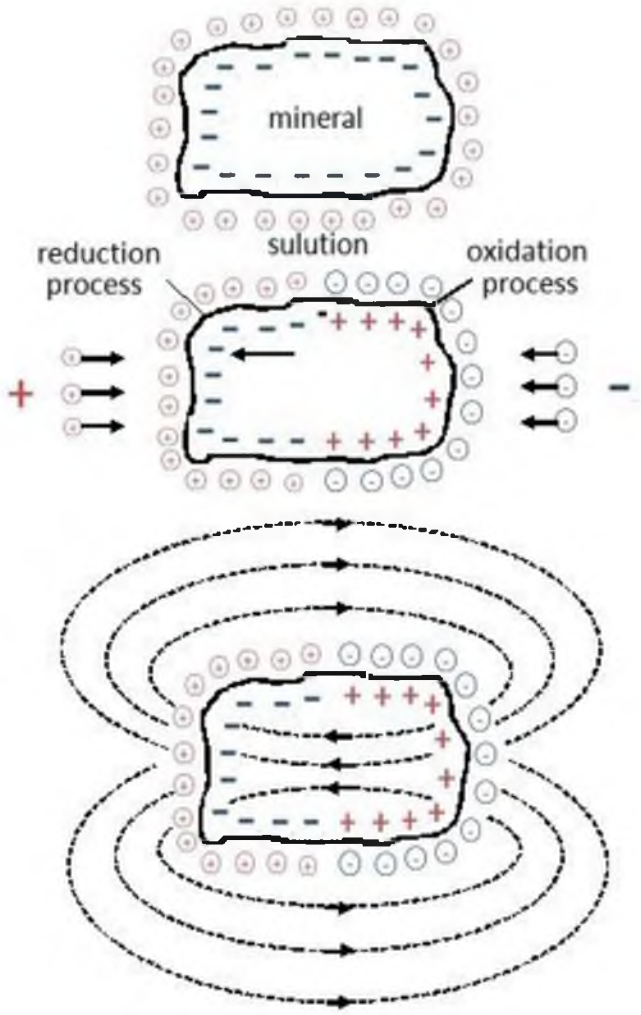

Figure 2.2 Top panel: there exists the natural double potential difference which happens on the interface of the electronic conductor and solution before injecting the current. Middle panel: as current flows, charge is transferred across the interface either by reduction if an electron is released from the solid phase to the electrolytic solution, or by oxidation, if an electron is released from the electrolytic solution to the solid phase. Bottom panel: finally, a net charge dipole is formed (adapted from Wightman et al., 2004).

depending on whether the current is going into or coming out of the metallic electrode. This is because there are different reactions involving oxidation at one interface and reduction at the other that take place at different rates (Sumner, 1976). With the continuation of current flow, the overvoltage gradually increases when increased accumulation of opposite charges occurs across the interface. The overvoltage will not increase any more until the speed of oxidation-reduction is the same as the one of added current. This phenomenon is called as the process of charging.

After cutting of the current, the opposite charges accumulated around the mineral will discharge through the interface itself, the electronic conductor internal and surrounding electrolytic solution will move back to their normal position. Meanwhile, the overvoltage decreases with time until it disappears in the process of discharging (Fig 2.2 bottom panel).

In the absence of chemical reactions between the water and the rock mineral, there is still a physical interaction. The electrical conductivity of the composite material will be determined by the electrical conductivity of the water filling the pore system in the rock and the pore size, shape, and connectivity (Olhoeft, 1985).

Electronic minerals generally have the behavior of electrode polarization. These include almost all of the sulfides, and some oxides such as magnetite, ilmenite, pyrolusite, and cassiterite. The magnitude of electrode polarization depends on the external current sources and also on a number of characteristics of the medium. There are numeuous factors that can establish some relationship between physical properties of rocks and IP effects:

1. The greater the fraction of pores that are blocked by conducting grains, the greater the IP effect will generate.

2. For a given content of conducting minerals, as the grain size of the minerals decreases, the amount of grain surface in contact with the electrolyte increases, which increases the surface resistance of mineral grains as well. If the grain size is too small, lesser fraction of total current will flow through pores blocked by such mineral grains, generating little IP effect. However, if the grain size is too big, the small amount of surface exposed will yield only a small IP effect. It is thus expected that intermediate size of grain can generate maximal IP effect.

3. For the same conducting mineral content, rock with low total porosity will polarize to a greater extent than rocks with high porosity. In the rock with lower porosity, a greater fraction of the total current is forced to flow through the conducting mineral grains than in high porosity rock.

4. The size of IP will depend on the fraction of pore space filled with electrolyte.

5. IP response decreases with increasing source frequency. This is true for membrane as well as electrode polarization.

2.2 Principles of IP Geophysical Methods

The theoretical and experimental foundation of IP methods in geophysical exploration was developed by several generations of geophysicists. The development of the IP method can be traced back to the 1950s, when both mining and petroleum companies were actively looking into the application of this method for mineral exploration. The physical-mathematical principles of the IP effect were originally

formulated in pioneering works by Wait (1959) and Sheinman (1969). However, this method did not find wide application in US industry until after the work of Zonge and his associates at the Zonge Engineering and Research Organization (Zonge and Wynn, 1975) and Pelton and Ward at the University of Utah (1978). Significant contribution to the development of the IP method was made, also, by Wait (1959, 1982), and by the research team at Kennecott in 1965-1977 (Nelson, 1997).

Measurements of IP may be made either in the time or the frequency domain. In the first method the geophysicist looks for portions of the earth where current flow is maintained for a short time after the applied current is terminated. In the second method the geophysicist tries to locate portions of the earth where the resistivity of the rocks decreases as the frequency of the applied current is increased. In both cases, the voltage is measured as a function of either time or frequency.

2.2.1 Time Domain

In the time domain, the simplest way to measure IP effect is to compare the residual voltage existing at a time after the current is cut off with the steady voltage during the current-flow interval (Telford et al., 1990). When the current is injected into the ground, the potential rises up immediately, but it takes some time to reach the maximum. The same behavior of the potential is observed when the current is terminated. The potential does not fall down to zero immediately, but takes some time to decay to zero. The time domain chargeability is defined as the ratio of the potential at some time after turn-off, $V(t)$, to the maximum value of the potential, V_c:

$$M(t) = V(t)/V_c \tag{2.1}$$

or as the ratio of the integral of the potential decay curve after turn-off to the maximum potential (Zhdanov, 2009). If this integration time is very short so we can sample the decay curve at several points, the values of the integral are effectively a measure of the potential existing at different times, that is, $V(t_1), V(t_2), \cdots, V(t_n)$. So the chargeability is defined as:

$$M = \frac{1}{V_c}\int_{t_1}^{t_2} V(t)dt \tag{2.2}$$

and is the most commonly used quantity in time domain IP measurement. When $V(t)$and $V_c$have the same units, the chargeability M is in milliseconds (Telford et al., 1990).

2.2.2 Frequency Domain

In frequency-domain IP, one measures the apparent resistivity at two or more frequencies. The percent frequency effect (PEF) is usually defined as the relative difference between the apparent resistivity with a very high frequency, ρ_{ac}, from that with a lower frequency (DC), ρ_{dc}, normalized by the apparent resistivity with the high frequency (Zhdanov, 2009), in percent:

$$PFE = 100 \times (\rho_{dc} - \rho_{ac})/\rho_{ac} \tag{2.3}$$

Another representation of the IP effect in the frequency domain is that the IP effect also leads to a phase shift between the current flowing through the rock and the voltage across a region containing metallic mineralization.

Note that the conventional IP method in the frequency domain is very similar to the DC resistivity survey and IP data acquisition systems and interpretation techniques are very similar to those of the DC resistivity methods (VES).

In the presence of the IP effect the measured potential in the frequency domain is complex; therefore, the apparent resistivity is characterized by a complex number, as well:

$$\rho_a(\omega) = \mathrm{Re}\rho_a(\omega) + i\mathrm{Im}\rho_a(\omega) \tag{2.4}$$

The magnitude of the complex apparent resistivity is the same as the DC apparent resistivity:

$$\rho_a^{DC}(\omega) = |\rho_a(\omega)| = \sqrt{\left(\mathrm{Re}\rho_a(\omega)\right)^2 + \left(\mathrm{Im}\rho_a(\omega)\right)^2} \tag{2.5}$$

and the phase is described as:

$$\emptyset_a(\omega) = \tan^{-1}\frac{\mathrm{Im}\rho_a(\omega)}{\mathrm{Re}\rho_a(\omega)} \tag{2.6}$$

Surface resistivity surveying is based on the principle that the distribution of electrical potential in the ground around a current-carrying electrode depends on the electrical resistivity and distribution of the surrounding soils and rocks. The usual practice in the field is to apply an electrical direct current (DC) between two electrodes implanted in the ground and to measure the difference of potential between two additional electrodes that do not carry current. Usually, the potential electrodes are in line between the current electrodes, but in principle, they can be located anywhere (Wightman et al., 2004).

In analysis of measurements made with such an array, we will assume that a current, I, is injected into the ground at point A, and, independently, a current, I, is injected into the ground at point B. We measure the voltage, ΔU_{MN}, at points M and N on the surface of the earth. This voltage, according to Ohm's law, will be proportional to the strength of the current, I, and also, be dependent on the electrical properties of the earth.

The potential at the point M will be the sum of contributions from the currents based on various frequencies flowing through point contacts A and B as follows:

$$\Delta U_{MN}(\omega) = U_M - U_N = \frac{I_{AB}(\omega)\rho_a(\omega)}{2\pi}\left(\frac{1}{r_{AM}} - \frac{1}{r_{BM}} + \frac{1}{r_{BN}} - \frac{1}{r_{AN}}\right) \quad (2.7)$$

In this model, ΔU_{MN} is proportional to the resistivity, ρ. One can define the apparent resistivity according to the standard DC resistivity formula:

$$\rho_a(\omega) = K\frac{\Delta U_{MN}(\omega)}{I_{AB}(\omega)} \quad (2.8)$$

where

$$K = \frac{2\pi}{\frac{1}{r_{AM}} - \frac{1}{r_{BM}} + \frac{1}{r_{BN}} - \frac{1}{r_{AN}}} \quad (2.9)$$

and K is the geometric factor for the array of electrodes being used to measure resistivity. The ratio $\Delta U_{MN}(\omega)/I_{AB}(\omega)$ is called the mutual resistance (Zhdanov, 2009).

2.2.3 Field Measurements

In reality, the only characteristic of the field we can measure is a voltage drop between two electrode contacts. The potential and the electric field are idealized mathematical concepts. However, if the distance r_{MN} is made small enough, the ratio $\Delta U_{MN}(\omega)/r_{MN}$ comes close to the value of E_{MN}, the component of the electric field along the line connecting the electrodes M and N. We often use this ratio to measure the electric field component at the halfway point between M and N (Zhdanov, 2009).

The most commonly used standard electrode array for IP is the Schlumberger array with four collinear electrodes symmetrically located about the midpoint of the array, and with the inner two electrodes, M and N, being closely spaced so that in effect, the component of the electric field along the array axis is measured (Fig 2.3 (a)). The

outer electrodes, A and B, are used to inject current into the earth. For this array, $r_{AN} = r_{BM}$ and $r_{AM} = r_{BN}$, and corresponding geometric factor is:

$$K = \pi a \left[\left(\frac{S}{\alpha} \right)^2 - \frac{1}{4} \right] \tag{2.10}$$

The second typical electrode configuration is the Wenner array. The Wenner array, like the Schlumberger array, makes use of four collinear electrodes, with the outer ones being designated as current electrodes and the inner pair as measurement electrodes. The single difference between the Wenner array and the Schlumberger array is that the electrodes are equally spaces in the Wenner system (Fig 2.3 (b)). For this array, $r_{AM} = r_{MN} = r_{NM} = \alpha$, and geometric factor is:

$$K = 2\alpha\pi \tag{2.11}$$

The dipole-dipole array belongs to the family of arrays using dipoles (closely spaced electrode pairs) to measure the curvature of the potential field. If the separation $\boldsymbol{\alpha}$ between both pairs of electrodes is the same, and the separation between the centers of the dipole is restricted to $\boldsymbol{\alpha(n+1)}$, the apparent resistivity is given by follows:

$$K = \pi\alpha n(n+1)(n+2) \tag{2.12}$$

The three above configurations are the most commonly used to measure induced polarization. Whatever is the geophysicist's preference, it is necessary to create a large enough voltage at the potential electrodes to make a satisfactory measurement in the presence of whatever natural electrical noise is present. This is determined by the sensitivity and noise-rejection capabilities of the voltmeter and power and current capabilities of the transmitter.

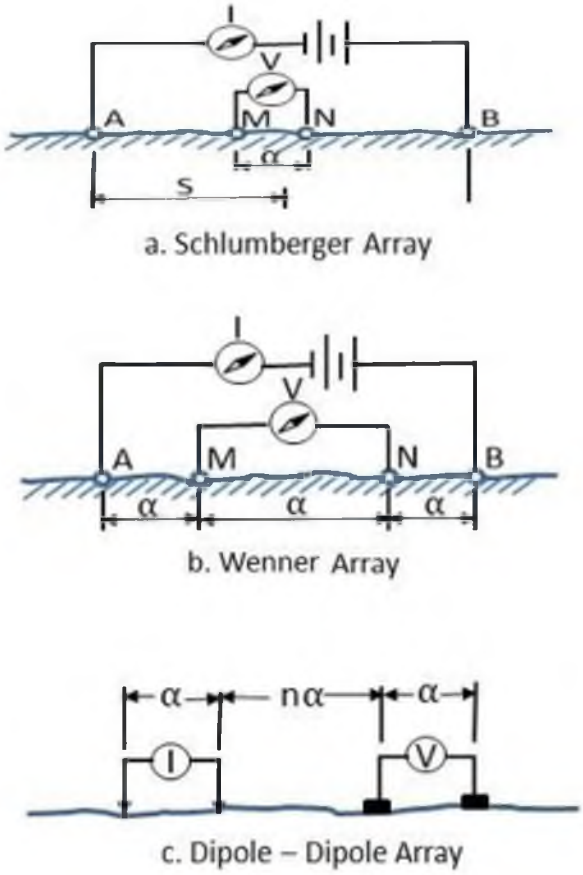

Figure 2.3 a) Schlumberger array with four collinear electrodes symmetrically located about the midpoint of the array, and with the inner two electrodes, M and N, being closely spaced so that in effect, the component of the electric field along the array axis is measured. **b)** Wenner electrode configuration with using of four collinear electrodes, with the outer ones being designated as current electrodes and the inner pair as measurement electrodes. **c)** Dipole-Dipole electrode configuration with using dipoles (closely spaced electrode pairs) to measure the curvature of the potential field (adapted from Wightman et al., 2004).

For the dipole-dipole configuration (Fig 2.3 (c)), the effect of the depth to the top of the source can be seen in that the apparent effects measured increase with the larger value of the offset (n). For more than two values of (n), we wish to show the resistivity at the same time. A two-dimensional (pseudo-section) (Fig 2.4) format has been developed to present dipole-dipole data with several values of (***n***). The 45-degree angle used to plot the data is entirely arbitrary. The pseudo-section plots are contoured, and the resulting anomalous patterns can be recognized as being caused by a particular geometry of source, and/or correlated from line to line (Van Blaricom, 1992).

However, the contoured data plots are most emphatically not meant to represent sections of the electrical parameters of the subsurface. The relationship between the plotted, contoured pseudo-section and the actual section of the electrical parameter is a

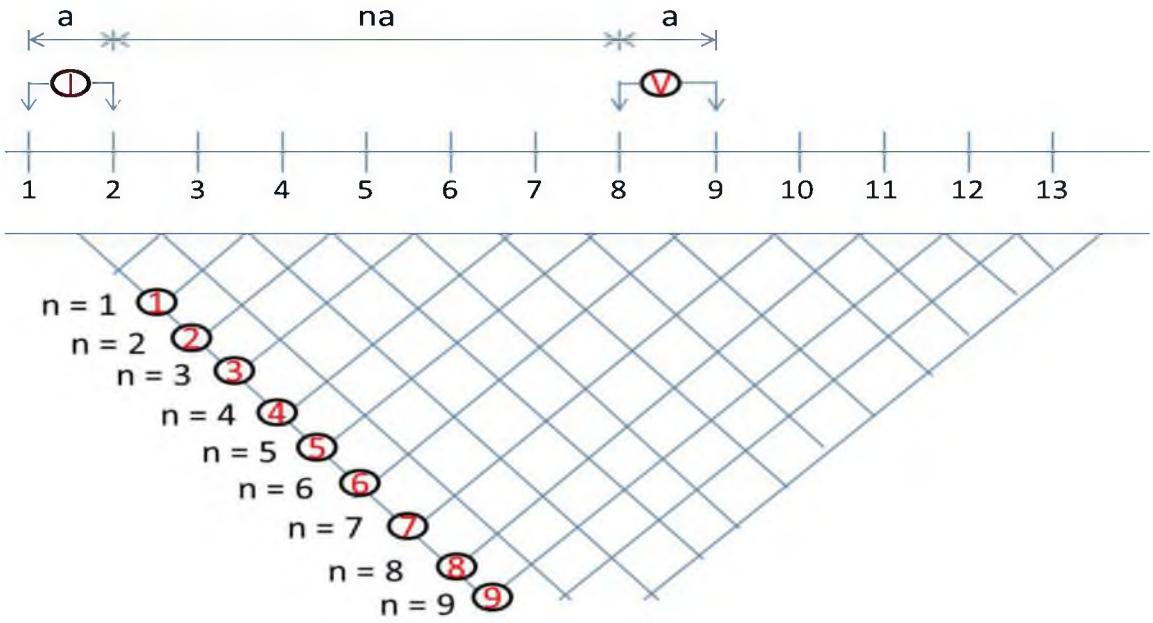

Figure 2.4 Pseudosection representation. The data are plotted at the midpoint of a transmitter and receiver pair versus a separation index, ***n*** (adapted from Zhdanov, 2009).

very complex mapping function. The pseudo-section data plots are merely a convenient method for showing all of the apparent results along a given line. The dipole-dipole measurement, which is lateral second derivative measurement, is the most sensitive to relatively small, lateral variation in the parameters of the earth and can be easily employed in the field because the lengths of wire are relatively short (Van Blaricom, 1992).

The disadvantage of the dipole-dipole configuration is the relatively small resistive coupling. With modern electronics, the design of IP equipment with higher power capabilities is practical. This is particularly true for variable frequency equipment or time domain equipment that uses coherent filters since noise rejection is better and current requirements are less (Van Blaricom, 1992).

There are important implications for exploration where a DC resistivity anomaly may mask an ore body making the phase response important to the interpretation, indicating the importance of understanding the IP effect of the ore body and surrounding geology. We should note that the pseudosections of the apparent resistivity and phase can be used for the qualitative interpretation of the IP data only. It is essential for the success of IP data interpretation to have a reliable method of quantitative analysis of the IP data. This analysis can be made on the basis of the appropriate conductivity model, quantitatively describing the relationships between the intrinsic characteristics of the heterogeneous rock and their effective conductivity, which can be determined by the IP surveys.

In making field measurements during an exploration program, the geophysicist rarely has the opportunity to measure the true value. The source being located is

relatively small and at some depth. Only an apparent effect at the surface can be measured. The apparent effect measured will be influenced by the size, depth and altitude of the source as well as the length of the electrode interval being used and the exact position of the electrodes themselves. Further, it is obvious that the electrical parameters of the surrounding rocks will also affect the apparent values measured from the source with a given true effect. Sometimes field experiences show that even for a shallow source, the apparent effects measured are much less than the true effects in the source(Van Blaricom, 1992). These phenomena also confirm that the apparent effects measured increase if the true effects are increased. For a large zone of disseminated sulfide mineralization the IP effect can be treated as a property of the rock volume. The effects are averaged and smooth, because of the smooth nature of solutions to the equations that govern electrical potentials and current flow. This smooth nature of potentials and the resulting averaged, smooth anomalies that are measured can make it difficult to interpret the source of a given IP anomaly.

Electromagnetic coupling presents a serious problem for induced polarization surveys, particularly when large electrode separations are used in areas of low resistivity. The electromagnetic eddy currents induced in the ground by current in the transmitting circuit vary with frequency, and their effects are similar to those of sulfide mineralization (Telford et al., 1990; Zonge and Wynn, 1975).

The first step in combating EM coupling is to use an appropriate electrode array. Arrays such as the Schlumberger and Wenner, where measurements are made between widely spaced current electrodes, generate large EM coupling and cannot be used except where resistivities are high. If a long current line is necessary to increase the signal in low

resistivity terrain, measurements must be made perpendicular to the current wire near one of the electrodes, as in the three-array or the perpendicular array. If the earth is homogeneous, there is no EM coupling with a perpendicular array. But lateral or vertical resistivity changes can produce large and sometimes negative EM coupling. The in-line dipole-dipole array offers both high earth resolution and lower EM coupling, at the expense of low receiver voltage levels. EM coupling is greater than the half-space coupling when the transmitter and receiver straddle the body at large separations. However, there are areas in the pseudosection where EM coupling over the prime is less than half-space coupling. In fact, negative EM coupling is often seen in field data taken over very conductive bodies (Telford et al., 1990). Hence, the goal is to eliminate EM coupling. The phase is the sum of two components: 1) caused by IP, which is constant with frequency and persists to very low frequencies; and 2) owing to EM coupling, which varies with frequency and is negligible at very low frequencies. The EM effects would decrease at low frequencies, but because of increasing natural electrical fields, reliable measurements often cannot be made below 0.1 Hz (Skinner, 1981). Time domain practitioners reduce the problem by using high currents and large, perpendicular arrays, and by allowing a large time interval between current shutoff and voltage measurement. This technique usually is successful because the EM coupling decays more rapidly than the IP response. Dipole-dipole and pole-dipole spreads are employed to reduce the EM coupling due to long wires and the frequency are usually kept below 10 Hz (Telford et al., 1990).

2.3 Review of the State-of-the-art in Interpretation of IP

The use of resistivity and spontaneous potential by the Schlumberger brothers is documented as early as 1900. Under Arthur Brant's direction, his Newmont group, pursued the theory and application of the technique in the field and laboratory. From that time activity flourished for over 30 years in both theory and practice. Sumi may have been one of the first to investigate mineral discrimination via the time domain waveform in the early sixties. Millett of Phelps Dodge published the first readily usable EM coupling calculations. Later, Van Voorhis et al., at Kennecott, developed the first EM de-coupling algorithms and Zonge introduced the concept of complex resistivity. Pelton presented arguments for using the Cole-Cole model as a basis for IP inversion (Pelton, 1977).

However, with the crash of copper prices in 1983, people dramatically declined the interest in disseminated sulfide (porphyry copper) deposits with a concurrent drop in research concerning the induced polarization (IP) response. The precipitous decline in oil prices in 1985 further reduced interest in IP, which was being used as one of the non-seismic alternatives in hydrocarbon exploration. Only in the last few years has the interest been renewed.

The most significant advancements in IP and complex resistivity (or spectral IP) in the recent past have not been in theory or practice, but rather in development of sophisticated instrumentation, for both receivers and transmitters, and robust data processing, modeling, and inversion code.

IP surveys are carried out worldwide, and will continue to be used effectively whenever disseminated sulfides are the target. IP is now utilized in environmental applications. Research is in progress to discern the effects of hydrocarbons and other contaminants on the cation exchange capacity of clays, and the resultant changes in IP response (Hohmann and Newman, 1990; Zonge, 2003).

Historically, the main reason for running an IP or CR survey has been to detect the response of disseminated sulfides and to map structural variations with resistivity. The same reasoning holds true today. The most popular arrays remain dipole-dipole (D-D) for profiling.

The main reason for Zonge developing multifrequency IP (complex resistivity or spectral IP) was two-fold; to remove EM coupling effects from IP data, and to identify the source of the IP respons (Telford et al., 1990). EM coupling removal has been successfully achieved and work continues in analyzing the IP response for mineral discrimination. Electrochemical models have been developed that utilize parameters associated with the generation of IP responses, such as Warburg impedance, double layer capacitance, charge transfer resistance, etc. (Carlson et al., 1994). The Cole-Cole representation has gained popularity as the model to determine time constants for the separation of responses due to clays, graphite and metallic-luster (sulfide) minerals. New models will be developed as more work is completed to determine the electrochemical sources for the IP response (Burtman et al., 2011; Zonge, 2003).

2.3.1 IP Modeling and Inversion

Improvements in modeling and inversion will make interpretation more accurate and easier for geophysicists trying to explain the data to a project geologist. One of the

fastest developing areas, with the advent of the improvements in the computer speed, has been 2D and 3D forward and inverse modeling. Finally, computers have enough speed and memory capacity to make complex 2D and 3D modeling both time and cost efficient.

The quantitative interpretation of IP data in a complex 3D environment is still a challenging problem of applied geophysics. Difficulties arise even in forward modeling because of the huge size of the numerical problem to be solved for adequate representation of the complex 3D distribution of IP multiple parameters in the media. As result, computer simulation time and memory requirements could be excessive especially for realistic models. Additional difficulties are related to the IP inverse problem solution. These problems are nonlinear and ill posed, because, in general cases, the solutions can be unstable and/or nonunique. In order to figure it out, there are four aspects needed to be considered at least as followings.

First is the calculation of the electromagnetic response. There are a couple of approaches to simulate EM data, such as finite volume (Dey and Morrison, 1979), finite element (FE), and finite difference (FD). However, the electromagnetic (EM) data observed in geophysical experiments reflect two phenomena: 1) electromagnetic induction (EMI), which is characterized by frequency independent conductivity, and 2) induced polarization (IP) with frequency dependent conductivity (Zhdanov, 2009). In the early days, it was thought that the IP effect must be confined to a finite body. The method cannot work in layered earth or in 2D earth for the TE mode (E parallel to strike) (Morrison and Gasperikova, 1996). So the inversion of 3D IP data is an extremely difficult problem because observed data are complicated by coupling with electromagnetic induction effects. This problem was considered in the paper (Li and

Oldenburg, 2000; Yoshioka, 2000), where authors demonstrated the possibility of electromagnetic coupling removal from the frequency domain IP data in a 3D environment using the integral equation (IE) method for forward modeling method which also could provide an effective tool for 3D inversion of IP data.

Secondly, selecting the forward operator appropriately plays an important role insimulating the electromagnetic field. The most common approach to the solution of nonlinear electromagnetic inverse problem is based on linearization of the nonlinear problem since the total electrical field $\vec{E}$ is a function of $\Delta\sigma$. This approach has found wide practical application because of the ease of its implementation, the accessibility of software for linear inversion, and the speed of numerical calculations. The simplest approach to linearization is based on the Born approximation. If we want to use the Born inversion, the total electrical field $\vec{E}$ can be approximated as background field $\vec{E}^b$. Within the framework of this method the Green's tensor $\overrightarrow{G_E}$ and $\overrightarrow{G_H}$, and the background field $\vec{E}^b$ stay unchanged. However, this approach is difficult to implement in practice, because it requires calculation of the Green's tensor for inhomogeneous media, which is an extremely time consuming problem in itself. On the other hand, the Born approximation is available to be used when there is not too much conductivity contrast between the background field and anomalies. In summary, linear inversion ignores the nonlinear effects.

Within the nonlinearization, one approach, which can be used in 3D inversion, is based on principle of quasi-linear (QL) approximation (Zhdanov et al., 2000; Zhdanov and Fang, 1996). According to QL approximation, the anomalous field $\overrightarrow{E^a}$ inside the inhomogeneous domain D is linearly proportional to the background field $\vec{E}^b$ through

some electrical reflectivity tensor $\hat{\boldsymbol{\lambda}}$. This inversion scheme reduces the original nonlinear inverse problem to three linear inverse problems: the first one for the material property tensor $\hat{\boldsymbol{m}}$ based on quasi-Born approximation, the second one for the tensor $\hat{\boldsymbol{\lambda}}$ and the third one for the conductivity $\Delta\tilde{\sigma}$ which is based on the Cole-Cole relaxation model. This approach was considered and realized 3D inversion of IP data in the paper (Yoshioka and Zhdanov, 2002).

The quasi-linear (QL) cannot be used for interpretation of multitransmitter data, because both the reflectivity tensor $\hat{\boldsymbol{\lambda}}$ and the material property tensor $\hat{\boldsymbol{m}}$ depend on the illuminating background electromagnetic field. However, in Dipole-Dipole arrays, airborne EM and well-logging, for example, the data are acquired with moving transmitter. In this case, Zhdanov and Tartaras put forward an effective inversion scheme based on the localized quasi-linear approximation (LQL) (Zhdanov and Tartaras, 2002). The main difference between QL and LQL is the reflectivity tensor $\hat{\boldsymbol{\lambda}}_L$ does not depend on the background field and the material property function $m_L(\mathbf{r})$ does not depend on the illuminating source. This method was successfully applied to the 3D inversion of IP data (Yoshioka and Zhdanov, 2003).

However, no matter what kind of methods introduced above people use, they actually indirectly recover the Cole-Cole parameters "step by step." In case any "step" is not accurate, the final inversion results of the Cole-Cole parameters will not be correct.

Thirdly, the algorithm of inversion is also important factor in the framework of inversion. Since in the inverse problem, while we may be almost certain that there is a unique physical inverse solution, widely differing numerical geoelectric models may be found, which may cause almost exactly the same electromagnetic field behavior

(Zhdanov, 2009). Moreover, the accuracy with which we know the electromagnetic field behavior is contaminated to some extent by telluric noise (Rowston et al., 2003) and measurement error.

Some researchers use Gauss-Newton and Markov-chain Monte Carlo-based method for Cole-Cole parameters estimation using 2D inversion algorithm in time domain (Oldenburg, 1997) and in frequency domain (Chen et al., 2008). Laterally constrained inversion (LCI) algorithm in which the model is composed of a set of laterally constrained 1D models aligned along a profile was put forward in time domain (Fiandaca et al., 2012). The preconditioned gradient technique was used to invert two of the IP parameters issued by 3D inversion of IP data was realized in wavelet domain instead of frequency or time domain (Zhu and Li, 2004). Michael Commer used the nonlinear conjugate gradient (NLCG) to minimize the error function to realize 3D inversion of IP data (Commer et al., 2011). The inverse problem of constructing 3D chargeability model was solved by the Tikhonov regularization method (Tikhonov and Arsenin, 1977) with additional bound constraints (Li and Oldenburg, 2000).

Finally, the conductivity $\Delta\tilde{\sigma}$ is based on the Cole-Cole relaxation model, which has four parameters that are not linearly independent. Especially the time constant τ and relaxation parameters C could cause additional instability in version. So most of researchers fixed those parameters (τ and C), which are supposed to be used to discriminate the texture of the rocks in the inversion.

The further development of a 3D and 4D (including time) joint inversion code will be a major factor over the next several years, and this may be more important than improvements for instrumentation. But 3D modeling and inversion mean using

instrumentation that can acquire large volumes of data and this acquisition must be economical enough for general use. The rapid development in computing technology is a good indicator that the high computing costs for voluminous data sets can be expected to decrease reasonably in the future.

Topography has probably played a larger role in the distortion of dipole-dipole and pole-dipole resistivity and IP data than previously realized. A note of caution, even when topography is available: we must be diligent in determining whether results make good geologic sense, even we get beautiful, mathematically correct, color sections that do not accurately reflect geology or mineralization.

CHAPTER 3

3D FORWARD MODELING OF IP DATA

3.1 Integral Equation Method for 3D EM Modeling

The integral equation method considers a 3D geoelectrical model with a horizontally layered background conductivity σ_b and a local inhomogeneous region, D, with an arbitrarily varying complex conductivity $\sigma = \sigma_b + \Delta\sigma$. Within this chapter we will assume $\mu = \mu_0 = 4\pi \times 10^{-7}$ H/m, H/m, where μ_0 is the free-space magnetic permeability. The model is excited by an electromagnetic field generated by an arbitrary source with an extraneous current distribution $\mathbf{j}^e$concentrated within some local domain Q. In this dissertation, I use electromagnetic modeling based on the Contraction integral Equation (CIE) method, which uses the contraction Green's operator (Hursán and Zhdanov, 2002).

The electromagnetic field in the model described above can be presented as a sum of the background and anomalous fields:

$$\mathbf{E} = \mathbf{E}^b + \mathbf{E}^a \tag{3.1}$$

$$\mathbf{H} = \mathbf{H}^b + \mathbf{H}^a \tag{3.2}$$

where the background field is generated by the given sources in the model with the background distribution of conductivity σ_b, and the anomalous field is produced by the anomalous conductivity distribution $\Delta\sigma$.

The total electromagnetic field in this model satisfies Maxwell's equations:

$$\nabla \times \mathbf{H} = \sigma\mathbf{E} + \mathbf{j}^{a} + \mathbf{j}^{e} \tag{3.3}$$

$$\nabla \times \mathbf{E} = i\omega\mu_0\mathbf{H} \tag{3.4}$$

which can be written separately for the background field $\mathbf{E^b}$ and $\mathbf{H^b}$,

$$\nabla \times \mathbf{H^b} = \sigma\mathbf{E^b} + \mathbf{j}^{e} \tag{3.5}$$

$$\nabla \times \mathbf{E^b} = \mathrm{i}\omega\mu_0\mathbf{H^b} \tag{3.6}$$

and for the anomalous field $\mathbf{E^a}$ and $\mathbf{H^a}$,

$$\nabla \times \mathbf{H^a} = \sigma\mathbf{E^a} + \mathbf{j}^{a} \tag{3.7}$$

$$\nabla \times \mathbf{E^a} = \mathrm{i}\omega\mu_0\mathbf{H^a} \tag{3.8}$$

where $\mathbf{j}^{a}$ is the density of extraneous electric currents, and

$$\mathbf{j}^{a}(\mathbf{r}) = \Delta\sigma(\mathbf{r})\mathbf{E}(\mathbf{r}) = \Delta\sigma(\mathbf{r})\left[\mathbf{E^b}(\mathbf{r}) + \mathbf{E^a}(\mathbf{r})\right] \tag{3.9}$$

is excess electric currents within the inhomogeneity D.

It is possible to determine the electromagnetic field of an arbitrary current distribution $\mathbf{j} = \mathbf{j}^{a} + \mathbf{j}^{e}$ within a medium with background conductivity $\boldsymbol{\sigma_b}$

$$\mathbf{E}(\mathbf{r}_j) = \iiint_D \widehat{\mathbf{G_E}}(\mathbf{r}_j|\mathbf{r}) \cdot \mathbf{j}(\mathbf{r})\mathrm{dv} = \mathbf{G_E}(\mathbf{j}) = \mathbf{G_E}(\mathbf{j}^{a}) + \mathbf{G_E}(\mathbf{j}^{e}) \tag{3.10}$$

$$\mathbf{H}(\mathbf{r}_j) = \iiint_D \widehat{\mathbf{G_H}}(\mathbf{r}_j|\mathbf{r}) \cdot \mathbf{j}(\mathbf{r})\mathrm{dv} = \mathbf{G_H}(\mathbf{j}) = \mathbf{G_H}(\mathbf{j}^{a}) + \mathbf{G_H}(\mathbf{j}^{e}) \tag{3.11}$$

where $\mathbf{G_E}$ and $\mathbf{G_H}$ are the electric and magnetic Green's operators. The proof of these formulae is based on an application of Green's theorem to the electric or magnetic field

and corresponding Green's tensor (Zhdanov, 2009). The anomalous fields generated by the excess current are as follows:

$$\mathbf{E}^a(\mathbf{r}_j) = \iiint_D \widehat{\mathbf{G}_E}(\mathbf{r}_j|\mathbf{r}) \cdot \mathbf{j}^a(\mathbf{r}) dv = \iiint_D \widehat{\mathbf{G}_E}(\mathbf{r}_j|\mathbf{r}) \cdot \Delta\sigma(\mathbf{r})\mathbf{E}(\mathbf{r})\, dv = \mathbf{G}_E(\mathbf{j}^a) \quad (3.12)$$

$$\mathbf{H}^a(\mathbf{r}_j) = \iiint_D \widehat{\mathbf{G}_H}(\mathbf{r}_j|\mathbf{r}) \cdot \mathbf{j}^a(\mathbf{r}) dv = \iiint_D \widehat{\mathbf{G}_H}(\mathbf{r}_j|\mathbf{r}) \cdot \Delta\sigma(\mathbf{r})\mathbf{E}(\mathbf{r})\, dv = \mathbf{G}_H(\mathbf{j}^a) \quad (3.13)$$

Using integral formula, one can calculate the electromagnetic field at any point $\mathbf{r}_j$, if the electric field is known within the inhomogeneity (Hohmann, 1975).

3.2 Cole-Cole and GEMTIP Models of Complex Resistivity

3.2.1 Cole-Cole Relaxation Model

It was demonstrated in the pioneer work of Pelton (Pelton, 1977), that the Cole-Cole relaxation model (Cole and Cole, 1941) can represent well the typical complex conductivity of polarized rock formation. In the framework of this model, the complex resistivity, $\rho_a(\omega)$, is described by the following expression (Pelton, 1977):

$$\rho_a(\omega) = \rho_0\left(1 - \eta\left(1 - \frac{1}{1+(i\omega\tau)^C}\right)\right) \quad (3.14)$$

where ρ_0 is the DC resistivity [Ohm-m]; ω is the angular frequency [rad/sec]; τ is the time parameter; η is the intrinsic chargeability (Seigel, 1959a); and C is the relaxation parameter. The dimensionless intrinsic chargeability, η, characterizes the intensity of the IP effect. These four parameters can reflect properties of rocks that allow distinguishing different kinds of rocks.

Fig 3.1 presents examples of typical complex resistivity curves with the Cole-Cole model parameters defined according to Table 3.1.

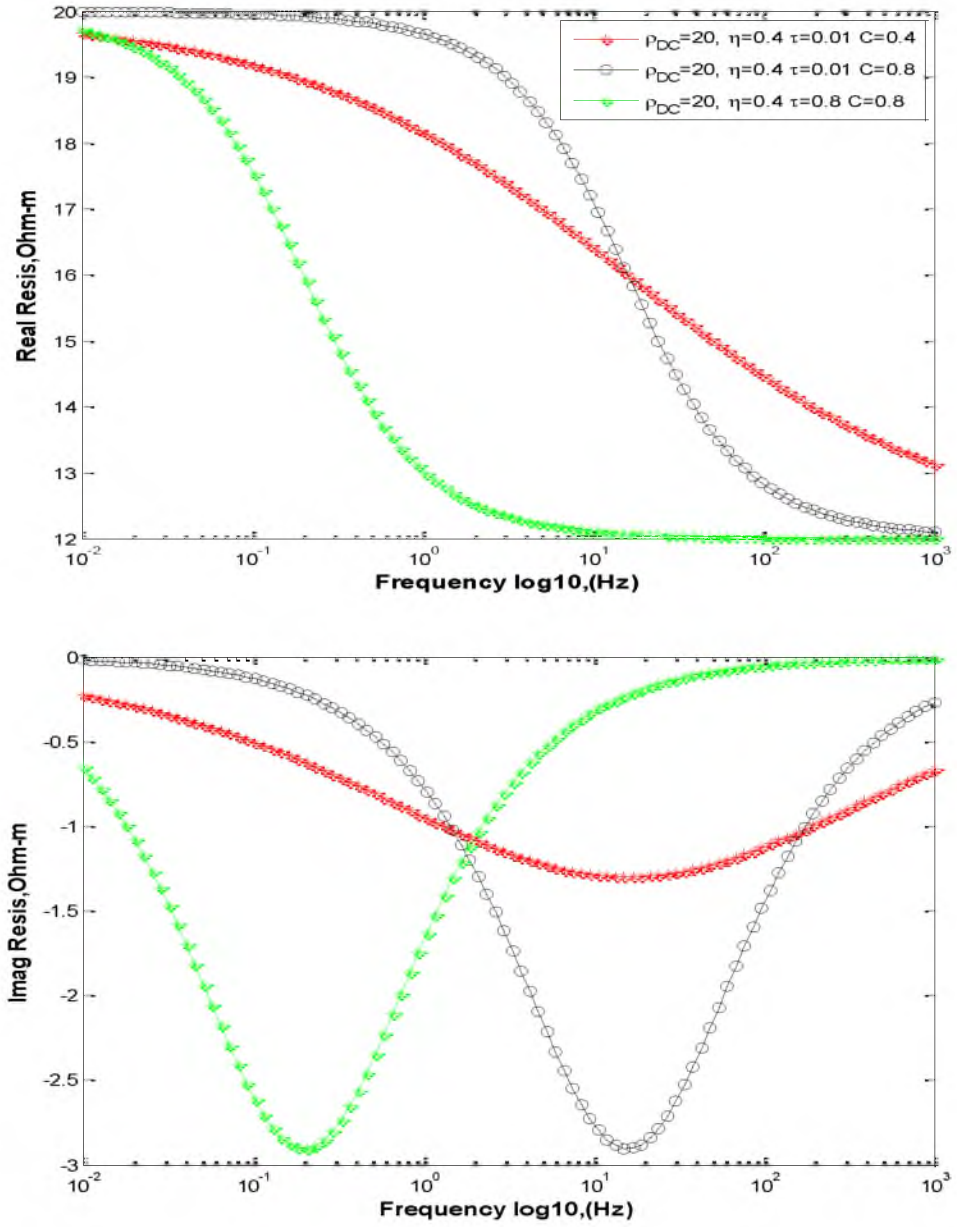

Figure 3.1 Top panel is variation of real part of resistivity based on black curve ($\rho_{DC} = 20\ ohm-m, \eta = 0.4, \tau = 0.01, C = 0.8$), red curve ($\rho_{DC} = 20\ ohm-m, \eta = 0.4, \tau = 0.01, C = 0.4$) and green curve ($\rho_{DC} = 20\ ohm-m, \eta = 0.4, \tau = 0.8, C = 0.8$); Bottom panel is variation of imaginary part of resistivity based on black curve ($\rho_{DC} = 20\ ohm-m, \eta = 0.4, \tau = 0.01, C = 0.8$), red curve ($\rho_{DC} = 20\ ohm-m, \eta = 0.4, \tau = 0.01, C = 0.4$) and green curve ($\rho_{DC} = 20\ ohm-m, \eta = 0.4, \tau = 0.8, C = 0.8$)

Table 3.1 Cole-Cole parameter for three different cases

	Blue	Black	Red
ρ_0	20 ohm-m	20 ohm-m	20 ohm-m
η	0.4	0.4	0.4
τ	0.8	0.01	0.01
C	0.8	0.8	0.4

One can see a significant difference between the red, black and green curves in Fig 3.1, which correspond to different Cole-Cole models with different parameters.

Note also that the Cole-Cole curve gives us just one possible example of the relaxation model. There are several other models discussed in the geophysical literature. One of the important practical questions is the relationship between the Cole-Cole model parameters and the petro-physical characteristics of mineralized rock.

The frequency, F_c, the "critical frequency," can often be used to describe a spectral response. It is the special frequency at which the maximum phase shift is measured. For the Cole-Cole Response Equation, the critical frequency, F_c, can be described in terms of the other parameters. Thus, the critical frequency is inversely proportional to the time constant, τ. If F_c occurs at high frequencies, the time constant, τ, is small. If F_c occurs at low frequencies, the time constant is large (Fig 3.1).

The value of C determines the slope of the imaginary resistivity-versus-frequency, log-log plot, for both high and low frequencies. For small values of C, the imaginary resistivity-versus-frequency curves are quite flat. For large values of C, the slopes become more pronounced and the imaginary resistivity-versus-frequency curves become more peaked. For larger C, the value of F_c is easily determined; for very small C, the value of F_c may not be so obvious (Fig 3.1).

For any given polarizable rock, the values of ρ and η will depend upon the porosity of the rock itself and the surface area of metallic minerals exposed to electrolyte in conductive pore spaces. Increasing the metallic mineral will decrease ρ_0 and increase η. Research efforts and field experience (Van Blaricom, 1992) show that τ and C are much more dependent upon the texture of the metallic mineralization present than upon the type of metallic minerals present. Two factors describe this texture. The first is the grain size for each population of polarization particles; the second is the number of populations of metallic particles present as well as the specific distribution of grain sizes within each population of polarization particles.

Field work and research indicates that the time constant, τ, of the measured IP effect is directly dependent upon the grain size of the metallic particles that are the source of the IP effect (Van Blaricom, 1992). For fine-grained mineralization, F_c is at high frequencies and τ is small. For coarse-grained mineralization, F_c is at low frequencies and τ is large. The first use of spectral IP data in defining the texture of metallic mineralization in the subsurface relates the time constant, τ, of the IP effect measured to the grain size of the mineralization. A change in the time constant, τ, obtained by this procedure reflects a change in the grain size of the polarizable particles.

Field measurements have produced spectral curves of all shapes. Computer inversion has given curves from as flat as (C=0.10) to as peaked as (C=0.50). Theoretical work shows that (C=0.50) would be the maximum theoretical value to be expected (Van Blaricom, 1992). The position of the critical frequency, F_c, is determined by the grain size, the shape of the imaginary resistivity-versus-frequency spectral plot is determined by the distribution of grain size. If a single, unique grain size is present, imaginary

resistivity-versus-frequency curve is very peaked with a value (C=0.5). The value of C based on the mean grain size of the normal distribution is smaller than the unique grain size. The broader distribution of the grain size population, however, results in a smaller value for C. The imaginary resistivity-versus-frequency curve is less peaked. This result agrees with field experience, so if a broad, nonunique distribution of grain size is present, the C value obtained by the inversion of the spectral curve is in the range 0.25 to 0.35 (Van Blaricom, 1992). For most spectral IP surveys, the value of C falls into this range. For some zones of metallic mineralization, there may be two populations of metallic particles present, resulting in discontinuous distribution of grain sizes. If the grain sizes for these two populations are different, the spectral curve would be expected to have a double peak. In more common situations, however, there are two overlapping distributions of grain sizes or continuous distribution over a wide range of grain sizes. The value for C is small, in the range from 0.1 to 0.2. The imaginary resistivity-versus-frequency curve is very flat. The magnitude of the imaginary resistivity-versus-frequency curve is low.

3.2.2 GEMTIP Model

Effective-medium theory (EMT) for composite media can be developed as a rigorous mathematical model to describe multiphase heterogeneous conductive media excited by an EM field. The EMT and its different extensions were applied successfully to the study of macroscopically isotropic and anisotropic models of rock formations in electrical geophysics. However, the existing form of EMT and its modifications only allow the inclusion of the EMI instead of the IP effect, which is manifested by additional

surface polarization of the grains caused by complex electrochemical reactions that accompany current flow within the formation in the general model of heterogeneous rocks.

Zhdanov (2008) developed the generalized effective-medium theory of induced polarization (GEMTIP) model based on the EMT that generates a conductivity model with parameters directly related by analytic expressions to the heterogeneous, multiphase rock formations with inclusions of arbitrary shape and conductivity by using the principles of Born-type quasi-linear (QL) approximation (Zhdanov, 2008). This new composite geoelectric model provides more realistic representation of complex rock formations than conventional unimodal-conductivity models. It takes into account the electromagnetic induction (EMI) and induced polarization (IP) effect related to the relaxation of polarized charges in rock formations and allows us to model the relationships between the geometric factors and physical characteristics of different types of rocks (e.g., grain size, shape, conductivity, polarizability, fraction volume and so forth).

Fig 3.2 shows that GEMTIP theory represents a complex heterogeneous rock formation as a composite model formed by a homogeneous host medium of a volume V with a complex conductivity tensor $\widehat{\sigma}_0(r)$ filled with grains of arbitrary shape and conductivity. In the present problem, the rock is composed of a set of N different types of grains, the l th grain type have a volume fraction f_l in the medium and a particular shape and orientation. The rigorous mathematical effective conductivity of the heterogeneous polarizable model was developed by Zhdanov (2008) as follows:

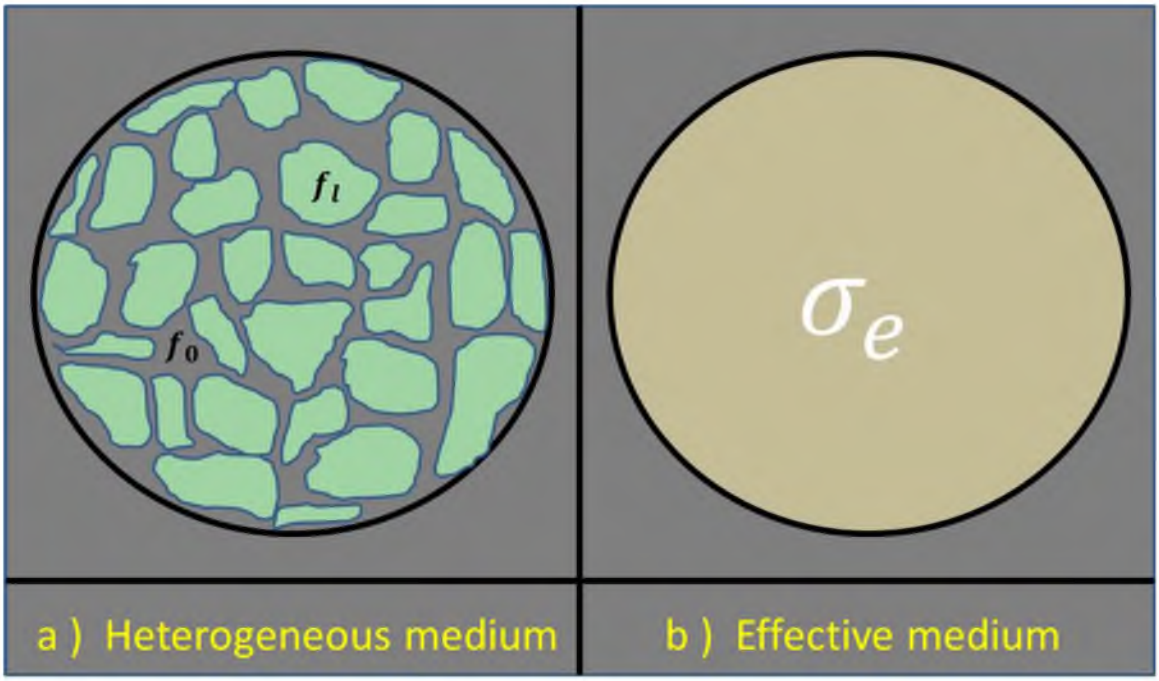

Figure 3.2 a) A schematic multiphase heterogeneous model of a reservoir rock sample. b) A corresponding effective-medium model (adapted from Zhdanov, 2008).

$$\hat{\sigma}_e = \hat{\sigma}_b + \left[\hat{\mathbf{I}} + \hat{\mathbf{p}}_0\right]^{-1}\hat{\mathbf{q}}_0 f_0 + \sum_{l=1}^{N}\left[\hat{\mathbf{I}} + \hat{\mathbf{p}}_l\right]^{-1}\hat{\mathbf{q}}_l f_l \tag{3.15}$$

where the related parameters are shown in Table 3.2.

Let us consider a composite model that is formed by a homogeneous host medium of a volume V with conductivity σ_0 filled with grains of spherical shape (Fig 3.2). We also assume that there are a set of N type of grains, with the l th grain type, having radius a_l, conductivity σ_l, and surface-polarizability k_l. So the Eq. 3.15 can be rewritten as:

$$\rho_e = \rho_0\left\{1 + \sum_{l=1}^{N}\left[f_l M_l\left[1 - \frac{1}{1+(i\omega\tau_l)^{C_l}}\right]\right]\right\}^{-1} \tag{3.16}$$

where the related parameters are shown in Table 3.2.

In the case of a two-phase composite model, there is a homogeneous host medium of a volume V with a complex resistivity ρ_0 and spherical inclusions with resistivity ρ_1.

Table 3.2 List of variables (adapted from Zhdanov 2008)

Heterogeneous rock formation with grains of *arbitrary* shape and conductivity	
$\hat{\sigma}$	Total conductivity
$\hat{\mathbf{p}}_0$	Surface-polarization tensor of the background
$\hat{\mathbf{q}}_0$	Volume-polarization tensor of the background
f_0	Volume fraction of a grain of background
f_l	Volume fraction of a grain of the lth type
$\hat{\sigma}_0$	Conductivity tensor of a host medium
$\hat{\sigma}_b$	Conductivity tensor of a homogeneous background
$\Delta\hat{\sigma}$	Anomalous-conductivity tensor
$\hat{\mathbf{m}}$	Material-property tensor
$\hat{\mathbf{G}}_\mathbf{b}$	Green's tensor for homogeneous background full space
$\hat{\mathbf{\Gamma}} = \iiint_V \hat{\mathbf{G}}_\mathbf{b} dv$	Volume-depolarization tensor
$\hat{\mathbf{\Lambda}} = \iint_S \hat{\mathbf{G}}_\mathbf{b} \cdot n n ds$	Surface-depolarization tensor
$\hat{\xi}(r') = k\sigma_b\hat{\sigma}(r') \cdot \left(\Delta\hat{\sigma}(r')\right)^{-1}, r' \in V_l$	Relative-conductivity tensor
$\hat{\mathbf{p}}_l = \hat{\Gamma}_l^{-1} \cdot \hat{\Lambda}_l \cdot \hat{\xi}(r'), r' \in V_l$	Surface-polarization tensor of the lth type
$\hat{\mathbf{q}}_l = \left[\hat{I} + \hat{p}_l\right] \cdot \hat{m}_l, r' \in V_l$	Volume-polarization tensor of the lth type
Heterogeneous rock formation with grains of spherical shape and conductivity	
ρ_0	Resistivity of host medium
ρ_l	Resistivity tensor of the lth grain type
C_l	Relaxation parameter of the lth grain type
$M_l = \frac{3(\rho_0 - \rho_l)}{2\rho_l + \rho_0}$	
$\tau_l = \left[\frac{a_l}{2\alpha_l}(2\rho_l + \rho_0)\right]^{1/C_l}$	Time constant of the lth grain type
Heterogeneous rock formation with grains of *two-phase spherical* shape and conductivity	
$\eta = \frac{3f_1(\rho_0 - \rho_1)}{2\rho_1 + \rho_0 + 3f_1(\rho_0 - \rho_1)}$	Relaxation parameter of the target grain type
$\tau = \left[\frac{a_1}{2\alpha_1}\left(2\rho_1 + \rho_0 + 3f_1(\rho_0 - \rho_1)\right)\right]^{1/C}$	Time constant of the target grain type

The Eq. 3.16 is simplified:

$$\rho_e = \rho_0 \left\{1 + f_1 M_1 \left[1 - \frac{1}{1+(i\omega\tau_1)^{c_1}}\right]\right\}^{-1} \tag{3.17}$$

After some algebra, we arrive at the conventional Cole-Cole formula for the effective resistivity

$$\rho_e = \rho_0 \left\{1 - \eta \left[1 - \frac{1}{1+(i\omega\tau)^{c}}\right]\right\} \tag{3.18}$$

where the related parameters are shown in Table 3.2.

Note that in Eq. 3.18, we use the same notations as in the original Cole-Cole formula Eq. 3.14.

Thus, both the conventional Cole-Cole model and the classical Wait's model appear as special cases of the general GEMTIP model of the complex resistivity of an isotropic, multiphase heterogeneous medium filled with spherical inclusion.

3.3 Forward Modeling of IP Data

A typical IP survey consists of multiple electric dipole transmitters and receivers. The integral equation can be used for 3D modeling of both electromagnetic induction and induced polarization effects in inhomogeneous structures. In this case Eq. 3.12 and Eq. 3.13 should be modified to take into account the IP effect. The main modification will include the expression for the anomalous conductivity, $\Delta\sigma$, which should be substituted now by another, complex value, $\Delta\sigma$ (Zhdanov, 2009). In order to take into account the IP effect, one should assume that the conductivity within the anomalous domain, $\sigma_b + \Delta\tilde{\sigma}$, becomes complex and frequency dependent and σ_b is a real number:

$$\sigma_b + \Delta\tilde{\sigma} = \sigma(\omega) = 1/\rho(\omega) \tag{3.19}$$

In the case of the IP effect study, I consider that the complex resistivity, $\rho(\omega)$, is described by the relaxation Cole-Cole model, Eq. 3.14. I assume that the Cole-Cole and GEMTIP model produce a complex resistivity curve at the frequency interval from a low frequency to a high frequency. So the anomalous conductivity, $\Delta\tilde{\sigma}$, is expressed as:

$$\Delta\tilde{\sigma} = \sigma(\omega) - \sigma_b \tag{3.20}$$

where for Cole-Cole model

$$\sigma(\omega) = \sigma_0\left(1 - \eta\left(1 - \frac{1}{1+(i\omega\tau)^C}\right)\right)^{-1} \tag{3.21}$$

where for GEMTIP model

$$\sigma(\omega) = \sigma_0\left\{1 + \sum_{l=1}^{N}\left[f_l M_l\left[1 - \frac{1}{1+(i\omega\tau_l)^{C_l}}\right]\right]\right\}^{-1} \tag{3.22}$$

and $\sigma_0 = 1/\rho_0$.

Thus,

$$\Delta\tilde{\sigma} = \sigma f(\eta, \tau, C) - \sigma_b \tag{3.23}$$

where function $f(\eta, \tau, C)$ for Cole-Cole and GEMTIP models are represented respectively (Zhdanov, 2009):

$$f(\eta, \tau, C) = \left(1 - \eta\left(1 - \frac{1}{1+(i\omega\tau)^C}\right)\right)^{-1} \tag{3.24}$$

$$f(\eta, \tau, C) = \left\{1 + \sum_{l=1}^{N}\left[f_l M_l\left[1 - \frac{1}{1+(i\omega\tau_l)^{C_l}}\right]\right]\right\}^{-1} \tag{3.25}$$

The anomalous electromagnetic field is related to the electric current induced in the inhomogeneity, $\boldsymbol{j}^a = \Delta\tilde{\sigma}\boldsymbol{E}$, according to the following integral formula (Zhdanov, 2009).

$$\boldsymbol{E}^a(r_j) = \iiint_D \widehat{\boldsymbol{G}_E}(r_j|r) \cdot \boldsymbol{j}^a(r)dv = \widehat{\boldsymbol{G}_E}(r_j|r) \cdot \Delta\tilde{\sigma}\boldsymbol{E}dv = A_E(r) \tag{3.26}$$

$$\boldsymbol{H}^a(r_j) = \iiint_D \widehat{\boldsymbol{G_H}}(r_j|r) \cdot \boldsymbol{j}^a(r)dv = \widehat{\boldsymbol{G_H}}(r_j|r) \cdot \Delta\tilde{\sigma}\boldsymbol{E}dv = A_H(r) \tag{3.27}$$

where $\widehat{\boldsymbol{G_E}}(r_j|r)$ and $\widehat{\boldsymbol{G_H}}(r_j|r)$ are the electric and magnetic Green's operators defined for an unbounded conductive medium with the background (horizontally layered) conductivity σ_b. A_E and A_H are corresponding integral operators, and domain D represents a volume with the anomalous conductivity distribution $\sigma(r) = \sigma_b(r) + \Delta\tilde{\sigma}(r)$, $r \ni D$. We can describe the forward problem by an operator equation:

$$d = A(\Delta\tilde{\sigma}) \tag{3.28}$$

CHAPTER 4

PRINCIPLES OF REGULARIZED INVERSION OF IP DATA

4.1 Regularized Conjugate Gradient Method for 3D Inversion of IP Data

Our goal is to solve operator equation. This equation can be written as:

$$\hat{d} = \hat{A}(\hat{m}) \tag{4.1}$$

where $\hat{m}$ is a vector of four model parameters σ, η, τ and C based on Cole-Cole model.

The inverse problem is ill posed, i.e., the solution can be nonunique and unstable. The traditional way to obtain the regularized solution of this equation is based on introducing the Tikhonov parametric functional (Zhdanov, 2002):

$$P^{\alpha}(\hat{m}) = \varphi(\hat{m}) + \alpha s(\hat{m}) \tag{4.2}$$

where $\varphi(\hat{m})$ is the misfit functional between the predicted data $\hat{A}(\hat{m})$ and the observed data, $\hat{d}$.

$$\varphi(\hat{m}) = \left(\hat{A}(\hat{m}) - \hat{d}\right)^{T}\left(\hat{A}(\hat{m}) - \hat{d}\right) \tag{4.3}$$

and $s(\hat{m})$ is an stabilizing functional that is usually introduced as the least-square difference between the regularized solution and some a priori model.

$$s(\hat{m}) = \left(\hat{m} - \hat{m}_{apr}\right)^{T}\left(\hat{m} - \hat{m}_{apr}\right) \tag{4.4}$$

In reality, the observed data can include different components of geophysical field or even different kinds of geophysical data with different units and scales. It is advisable to have the prediction errors of the more accurate observations a greater weight than the inaccurate observation to smooth the data. In this situation, the equation has to rewritten to include data weights in calculation of the misfit functional:

$$\varphi_w(\hat{m}) = \left(\hat{W}_d\hat{A}(\hat{m}) - \hat{W}_d\hat{d}\right)^T\left(\hat{W}_d\hat{A}(\hat{m}) - \hat{W}_d\hat{d}\right) \tag{4.5}$$

where $\hat{W}_d$ is the data weighting matrix, which assigns a greater weight to more accurate observations than inaccurate observations and levels the scales of the different data sets.

In principle, a similar approach can be used in evaluating the stabilizing functional. So the equation can also be rewritten to include some weights in calculation of the stabilizer functional:

$$s_w(\hat{m}) = \left(\hat{W}_m\,\hat{m} - \hat{W}_m\hat{m}_{apr}\right)^T\left(\hat{W}_m\,\hat{m} - \hat{W}_m\,\hat{m}_{apr}\right) \tag{4.6}$$

where $\hat{W}_m$ is the model weighting matrix.

Consider the forward geophysical problem described by equation. For the regularized solution of this inverse problem, we rewrite Eq. 4.2 as:

$$P^\alpha(\hat{m},\hat{d}) = \left(\hat{A}(\hat{m}) - \hat{d}\right)^T\hat{W}_d^2\left(\hat{A}(\hat{m}) - \hat{d}\right) + \alpha\left(\hat{m} - \hat{m}_{apr}\right)^T\hat{W}_m^2\left(\hat{m} - \hat{m}_{apr}\right) \tag{4.7}$$

where $\hat{W}_m$ is model weighting matrixes which are defined respectively (Zhdanov, 2002).

I developed $\hat{W}_d$ based on my research since E^b depends on frequencies. This choice of model weighting matrix ensures a uniform sensitivity to the different model parameters (Zhdanov, 2002).

$$\hat{W}_d = \frac{1}{\|E^b\|} \tag{4.8}$$

$$\hat{W}_m = \sqrt[4]{\hat{F}_m^T \cdot \hat{F}_m} \tag{4.9}$$

where $\hat{F}_m$ is the new Fréchet derivative of forward operator $\hat{A}$. In this paper, the linear Fréchet derivative operator can be represented by a matrix that consists of the partial derivation of data with respect to the four model parameters σ, η, τ and C.

According to the basic principles of the regularization method, we have to find the model $\hat{m}_\alpha$, a quasi-solution of the inverse problem that minimizes the parametric functional:

$$P^\alpha(\hat{m}, \hat{d}) = \min \tag{4.10}$$

Note that the solution of this problem is equivalent to the minimization of the stabilizing functional:

$$s_w(\hat{m}) = (\hat{W}_m\,\hat{m} - \hat{W}_m\,\hat{m}_{apr})^T(\hat{W}_m\,\hat{m} - \hat{W}_m\hat{m}_{apr}) = \min \tag{4.11}$$

under the condition that misfit is equal to the given level of the noise:

$$\varphi_w(\hat{m}) = (\hat{W}_d\hat{A}(\hat{m}) - \hat{W}_d\hat{d})^T(\hat{W}_d\hat{A}(\hat{m}) - \hat{W}_d\hat{d}) = \delta \tag{4.12}$$

We apply the gradient type method to the solution of the minimum parametric functional problem, which is based on computing the gradient direction for the parametric functional and decreasing this functional by moving iteratively "down the hill" (Tarantola, 1987) in the space of model parameters.

Following the conventional ideas of the descent method, we calculate the first variation of the parametric functional in order to find the gradient direction, assuming that the operator is differentiable, so that

$$\delta\hat{A}(\hat{m}) = \hat{F}_m\delta\hat{m} \tag{4.13}$$

where $\hat{F}_m$ is the Fréchet derivative matrix of $\hat{A}$ (Zhdanov, 2002).

Thus, we obtain:

$$\delta P^\alpha(\hat{m}, \hat{d}) = 2(\delta\hat{m})^T\hat{F}_m^*\hat{W}_d^2(\hat{A}(\hat{m}) - \hat{d}) + 2\alpha(\delta\hat{m})^T\hat{W}_m^2(\hat{m} - \hat{m}_{apr}) \tag{4.14}$$

where we assume that the matrices $\widehat{W}_d$ and $\widehat{W}_m$ are diagonal.

Following the regularized conjugate gradient method, we can select:

$$\delta\hat{m} = -\widetilde{k_n^{\alpha}}\widehat{l}^{\alpha}(\hat{m}_n) \tag{4.15}$$

where the "direction" of ascent $\widehat{l}^{\alpha}(\hat{m}_n)$ can be calculated as following:

$$\widehat{l}^{\alpha}(\hat{m}_{n+1}) = \widehat{l}^{\alpha}(\hat{m}_{n+1}) + \beta_{n+1}^{\alpha}\widehat{l}^{\alpha}(\hat{m}_n) \tag{4.16}$$

However, the $\widehat{l}^{\alpha}(\hat{m}_n)$ is now determined according to the formulae for the least-squares method:

$$\widehat{l}^{\alpha}(\hat{m}_n) = \hat{F}_m^{*}\widehat{W}_d^2\left(\widehat{A}(\hat{m}_n) - \hat{d}\right) + \alpha\widehat{W}_m^2\left(\hat{m}_n - \hat{m}_{apr}\right) \tag{4.17}$$

An iterative process of the method is constructed according to the formulae:

$$\hat{m}_{n+1} = \hat{m}_n + \delta\hat{m} = \hat{m}_n - \widetilde{k_n^{\alpha}}\widehat{l}^{\alpha}(\hat{m}_n) \tag{4.18}$$

where the coefficient $\widetilde{k_n^{\alpha}}$ is defined by a line search according to the condition:

$$P^{\alpha}(\hat{m}_{n+1}) = P^{\alpha}\left(\hat{m}_n - \widetilde{k_n^{\alpha}}\widehat{l}^{\alpha}(\hat{m}_n)\right) = \Phi^{\alpha}\left(\widetilde{k_n^{\alpha}}\right) = \min \tag{4.19}$$

We discuss now the problem of the determination of $\widetilde{k_n^{\alpha}}$. To solve this problem we can consider more carefully the functional $\Phi^{\alpha}\left(\widetilde{k_n^{\alpha}}\right)$ (Zhdanov, 2002):

$$\Phi^{\alpha}\left(\widetilde{k_n^{\alpha}}\right) = P^{\alpha}\left(\hat{m}_n - \widetilde{k_n^{\alpha}}\widehat{l}^{\alpha}(\hat{m}_n)\right)$$

$$= \left(\widehat{A}\left(\hat{m}_n - \widetilde{k_n^{\alpha}}\widehat{l}^{\alpha}(\hat{m}_n)\right) - \hat{d}\right)^{T}\widehat{W}_d^2\left(\widehat{A}\left(\hat{m}_n - \widetilde{k_n^{\alpha}}\widehat{l}^{\alpha}(\hat{m}_n)\right) - \hat{d}\right) +$$

$$\alpha\left(\hat{m}_n - \widetilde{k_n^{\alpha}}\widehat{l}^{\alpha}(\hat{m}_n) - \hat{m}_{apr}\right)^{T}\widehat{W}_m^2\left(\hat{m}_n - \widetilde{k_n^{\alpha}}\widehat{l}^{\alpha}(\hat{m}_n) - \hat{m}_{apr}\right) \tag{4.20}$$

In the last equation we can assume that $\widetilde{k_n^{\alpha}}\widehat{l}^{\alpha}(\hat{m}_n)$ is small enough, so we can use linearize representation for operator $\widehat{A}\left(\hat{m}_n - \widetilde{k_n^{\alpha}}\widehat{l}^{\alpha}(\hat{m}_n)\right)$:

$$\widehat{A}\left(\hat{m}_n - \widetilde{k_n^{\alpha}}\widehat{l}^{\alpha}(\hat{m}_n)\right) \approx \widehat{A}(\hat{m}_n) - \widetilde{k_n^{\alpha}}\hat{F}_{m_n}\widehat{l}^{\alpha}(\hat{m}_n) \tag{4.21}$$

Meanwhile, let us assume some conditions:

$$\hat{\mathrm{F}}^{*}_{\mathrm{m_w}} = \hat{\mathrm{W}}_d \hat{\mathrm{F}}^{*}_{\mathrm{m_n}} \mathrm{i}\hat{\mathrm{W}}_m \tag{4.22}$$

$$\hat{\mathrm{m}}_{\mathrm{n_w}} = \hat{\mathrm{W}}_m \hat{\mathrm{m}}_{\mathrm{n}} \tag{4.23}$$

$$\hat{\mathrm{m}}_{\mathrm{w\_apr}} = \hat{\mathrm{W}}_m \hat{\mathrm{m}}_{\mathrm{apr}} \tag{4.24}$$

$$\hat{\mathrm{l}}^{\alpha}(\hat{\mathrm{m}}_{\mathrm{n}})_{\mathrm{w}} = \mathrm{i}\hat{\mathrm{W}}_m \hat{\mathrm{l}}^{\alpha}(\hat{\mathrm{m}}_{\mathrm{n}}) \tag{4.25}$$

$$\hat{\tilde{\mathrm{l}}}^{\alpha}(\hat{\mathrm{m}}_{\mathrm{n}})_{\mathrm{w}} = \mathrm{i}\hat{\mathrm{W}}_m \hat{\tilde{\mathrm{l}}}^{\alpha}(\hat{\mathrm{m}}_{\mathrm{n}}) \tag{4.26}$$

$$\hat{\mathrm{R}}_{\mathrm{n_w}} = \hat{\mathrm{W}}_d\left(\hat{\mathrm{A}}(\hat{\mathrm{m}}_{\mathrm{n}}) - \hat{\mathrm{d}}\right) \tag{4.27}$$

where $\mathrm{i}\hat{\mathrm{W}}_m$ is the inverse of $\hat{\mathrm{W}}_m$.

Under this situation, the Eq. 4.17 can be rewritten as follows:

$$\hat{\mathrm{l}}^{\alpha}(\hat{\mathrm{m}}_{\mathrm{n}}) = \hat{\mathrm{F}}^{*}_{\mathrm{m_w}} \hat{\mathrm{R}}_{\mathrm{n_w}} + \alpha\left(\hat{\mathrm{m}}_{\mathrm{n_w}} - \hat{\mathrm{m}}_{\mathrm{w\_apr}}\right) \tag{4.28}$$

Then $\widetilde{\mathrm{k}^{\alpha}_{\mathrm{n}}}$ can be expressed as follows:

$$\widetilde{\mathrm{k}^{\alpha}_{\mathrm{n}}} = \frac{\left(\hat{\tilde{\mathrm{l}}}^{\alpha}(\hat{\mathrm{m}}_{\mathrm{n}})\right)^{\mathrm{T}}\left(\hat{\mathrm{l}}^{\alpha}(\hat{\mathrm{m}}_{\mathrm{n}})\right)}{\left(\hat{\tilde{\mathrm{l}}}^{\alpha}(\hat{\mathrm{m}}_{\mathrm{n}})\right)^{\mathrm{T}}\left((\hat{\mathrm{F}}_{\mathrm{m_n}})^{\mathrm{T}}(\hat{\mathrm{F}}_{\mathrm{m_n}}) + \alpha\mathrm{I}\right)\left(\hat{\tilde{\mathrm{l}}}^{\alpha}(\hat{\mathrm{m}}_{\mathrm{n}})\right)} \tag{4.29}$$

The algorithm of the re-weighted regularized conjugate gradient method to solve the minimization of Eq. 4.19 is given as follows:

$$\mathrm{r}^{\mathrm{w}}_{\mathrm{n}} = \hat{\mathrm{W}}_d\left(\hat{\mathrm{A}}(\hat{\mathrm{m}}_{\mathrm{n}}) - \hat{\mathrm{d}}\right)$$

$$\widehat{\mathrm{l}^{\alpha_{\mathrm{n}}}_{\mathrm{n}}}(\hat{\mathrm{m}}_{\mathrm{n}}) = \left(\hat{\mathrm{F}}_{\mathrm{m_n}}\right)^{\mathrm{T}}\mathrm{r}^{\mathrm{w}}_{\mathrm{n}} + \alpha_{\mathrm{n}}\left(\hat{\mathrm{m}}_{\mathrm{n_w}} - \hat{\mathrm{m}}_{\mathrm{w\_apr}}\right)$$

$$\beta^{\alpha_{\mathrm{n}}}_{\mathrm{n}} = \left\|\widehat{\mathrm{l}^{\alpha_{\mathrm{n}}}_{\mathrm{n}}}\right\|^2 / \left\|\widehat{\mathrm{l}^{\alpha_{\mathrm{n-1}}}_{\mathrm{n-1}}}\right\|^2, \widehat{\mathrm{l}^{\alpha_{\mathrm{n}}}_{\mathrm{n}}} = \widehat{\mathrm{l}^{\alpha_{\mathrm{n}}}_{\mathrm{n}}} + \beta^{\alpha_{\mathrm{n}}}_{\mathrm{n}}\widehat{\mathrm{l}^{\alpha_{\mathrm{n-1}}}_{\mathrm{n-1}}}, \widehat{\mathrm{l}^{\alpha_{\mathrm{o}}}_{0}} = \widehat{\mathrm{l}^{\alpha_{\mathrm{o}}}_{0}} \tag{4.30}$$

$$\widetilde{\mathrm{k}^{\alpha_{\mathrm{n}}}_{\mathrm{n}}} = \frac{\left(\widehat{\tilde{\mathrm{l}}^{\alpha_{\mathrm{n}}}_{\mathrm{n}}}\right)^{\mathrm{T}}\left(\widehat{\mathrm{l}^{\alpha_{\mathrm{n}}}_{\mathrm{n}}}\right)}{\left(\widehat{\tilde{\mathrm{l}}^{\alpha_{\mathrm{n}}}_{\mathrm{n}}}\right)^{\mathrm{T}}\left((\hat{\mathrm{F}}_{\mathrm{m_w}})^{\mathrm{T}}(\hat{\mathrm{F}}_{\mathrm{m_w}}) + \alpha\mathrm{I}\right)\left(\widehat{\tilde{\mathrm{l}}^{\alpha_{\mathrm{n}}}_{\mathrm{n}}}\right)}$$

$$\hat{\mathrm{m}}_{n+1_w} = \hat{\mathrm{m}}_{\mathrm{n_w}} - \widetilde{\mathrm{k}^{\alpha_{\mathrm{n}}}_{\mathrm{n}}}\widehat{\mathrm{l}^{\alpha_{\mathrm{n}}}_{\mathrm{n}}}(\hat{\mathrm{m}}_{\mathrm{n}})$$

I apply the adaptive regularization method. The regularization parameter α is updated in the process of the iterative inversion as follows:

$$\alpha_n = \alpha_1 q^{n-1}; n = 1, 2, 3 \ldots\ldots; 0 < q < 1 \tag{4.31}$$

The above iterative process is terminated when the misfit reach the given level ϵ_0:

$$\phi(\hat{m}_n) = \|r_n^w\|^2 < \epsilon_0 \tag{4.32}$$

4.2 Fréchet Derivative Calculation for Cole-Cole Model

The IP forward modeling operator is described by formulae, which I reproduce here for convenience:

$$d = A_E(\Delta\tilde{\sigma}) = A(m) \tag{4.33}$$

where d is a vector of the observed EM data, m is a vector formed by a distribution of the four Cole-Cole model DC conductivity (σ_0), chargeability (η), time parameter (τ), and relaxation parameters (C) in the subsurface formations, and A is a nonlinear operator transforming the Cole-Cole parameters into the electric field.

Applying the variational operator δ to operator A, and using the chain rule of differentiation, I obtain the following:

$$\delta A = F_E\delta_\sigma\Delta\tilde{\sigma} + F_E\delta_\eta\Delta\tilde{\sigma} + F_E\delta_\tau\Delta\tilde{\sigma} + F_E\delta_C\Delta\tilde{\sigma}$$

$$= F_E f(\eta,\tau,C)\delta_\sigma + F_E\sigma\frac{\partial f(\eta,\tau,C)}{\partial\eta}\delta_\eta + F_E\sigma\frac{\partial f(\eta,\tau,C)}{\partial\tau}\delta_\tau + F_E\sigma\frac{\partial f(\eta,\tau,C)}{\partial C}\delta_C$$

$$= \left[F_E f(\eta,\tau,C),\ F_E\sigma\frac{\partial f(\eta,\tau,C)}{\partial\eta},\ F_E\sigma\frac{\partial f(\eta,\tau,C)}{\partial\tau},\ F_E\sigma\frac{\partial f(\eta,\tau,C)}{\partial C}\right]\begin{bmatrix}\delta_\sigma\\ \delta_\eta\\ \delta_\tau\\ \delta_C\end{bmatrix} \tag{4.34}$$

where F_E is the Fréchet derivative matrix of the original forward modeling operator, A_E, represented by integral equation. This Fréchet derivative can be found using the corresponding perturbation of the anomalous field $\mathbf{E}^{a}(\mathbf{r}_j)$ (Zhdanov, 2009).

From expression, I conclude that the Fréchet derivative matrix, $\hat{F}_m$, of nonlinear IP forward modeling operator A is given by the following expression:

$$\hat{F}_m = \left[F_E f(\eta,\tau,C),\ F_E\sigma\frac{\partial f(\eta,\tau,C)}{\partial\eta},\ F_E\sigma\frac{\partial f(\eta,\tau,C)}{\partial\tau},\ F_E\sigma\frac{\partial f(\eta,\tau,C)}{\partial C}\right] \tag{4.35}$$

where

$$\frac{\partial f(\eta,\tau,C)}{\partial\eta} = \frac{\partial}{\partial\eta}\left(1-\eta\left(1-\frac{1}{1+(i\omega\tau)^C}\right)\right)^{-1}$$

$$= \left(1-\eta\left(1-\frac{1}{1+(i\omega\tau)^C}\right)\right)^{-2}\left(1-\frac{1}{1+(i\omega\tau)^C}\right); \tag{4.36}$$

$$\frac{\partial f(\eta,\tau,C)}{\partial\tau} = \frac{\partial}{\partial\tau}\left(1-\eta\left(1-\frac{1}{1+(i\omega\tau)^C}\right)\right)^{-1}$$

$$= -\eta(i\omega)^C\cdot\tau^{C-1}\left(1-\eta\left(1-\frac{1}{1+(i\omega\tau)^C}\right)\right)^{-2}(1+(i\omega\tau)^C)^{-2}; \tag{4.37}$$

$$\frac{\partial f(\eta,\tau,C)}{\partial C} = \frac{\partial}{\partial C}\left(1-\eta\left(1-\frac{1}{1+(i\omega\tau)^C}\right)\right)^{-1}$$

$$= -\eta(i\omega\tau)^C\ln(i\omega\tau)\left(1-\eta\left(1-\frac{1}{1+(i\omega\tau)^C}\right)\right)^{-2}(1+(i\omega\tau)^C)^{-2}; \tag{4.38}$$

$\hat{F}_m$ is the Fréchet derivative matrix of nonlinear IP forward modeling operator A. The matrix of the Fréchet derivative, $\hat{F}_m$, is the Fréchet derivative matrix of nonlinear IP forward modeling operator A and is formed by a product of the matrix of the Fréchet derivative of the original forward modeling operator, F_E, and the partial derivative of the

anomalous conductivity with respect to the four Cole-Cole model parameters σ, η, τ and C.

4.3 Numerical Implementation of IP Inversion Using Parallel Computing

In this dissertation, there are four Cole-Cole parameters involved in the inversion, in other words, within each cell, there are DC conductivity (σ_0), chargeability (η), time parameters (τ), and relaxation parameters (C) instead of conductivity only, especially for Dipole-Dipole configuration, which requires more sources and receivers. One the other hand, calculating Green tensor and Fréchet matrix takes a lot of time and storing them also occupy much more memory. So, if using one thread/process to make the inversion, it will be seriously time-consuming and out of memory may happen.

The inversion code can be implemented as parallel computation application, which can be considered to realize in person PC that have multicores and relatively high performance. I use MATLAB parallel computation to realize it. This approach allows us to use multiple MATLAB processes running on a single machine with multiple processors. However, no coordination between the MATLAB processes is provided. Instead, a parent process passes off data to the child processes. Then all processes work on its local data, and return the result to the parent process. Under this model, the type of functions that can be parallelized is limited. For example, a for-loop with any data dependency across iteration would be impossible to parallelize under this model. However, this model has the advantage of simplicity. In the software we found that

utilize this approach, usually no change in existing code is needed to parallelize the code, if the code is parallelizable using this simple approach.

In Model 4, for example, the observed data contain eight frequencies and 675 receivers per frequency, and the inversion domain is divided into 1960 cells which contain four Cole-Cole parameters that are constant in each cell. Before inverting thousands of data to 3D models with thousands of cells, the Green tensor and background EM field need to be calculated.

I allocate eight frequencies data to eight child threads. Within each thread, I calculate Greens tensor and the background EM field based on its frequency within whole 3D domain independently. After they finish calculating, each thread sends its own results of Green tensor and background EM field to parent thread to "accumulate" these results together that will be used in future inversion. Using parallel computation for Green tensor and background, the EM field can run the calculation about eight times faster than using one thread/process (Fig 4.1).

Calculation of the Fréchet matrix also is also time-consuming. We allocate eight frequencies data to eight child threads again, similarly as above. Each child thread calculates Fréchet matrix for its frequency within entire inversion domain independently. After they accomplish their own job, they send the results back to parent thread to accumulate these local Fréchet matrixes together to form a full Fréchet matrix, which contains all the frequencies information. This process is about 7.5 times faster than using the single thread/process (Fig 4.1).

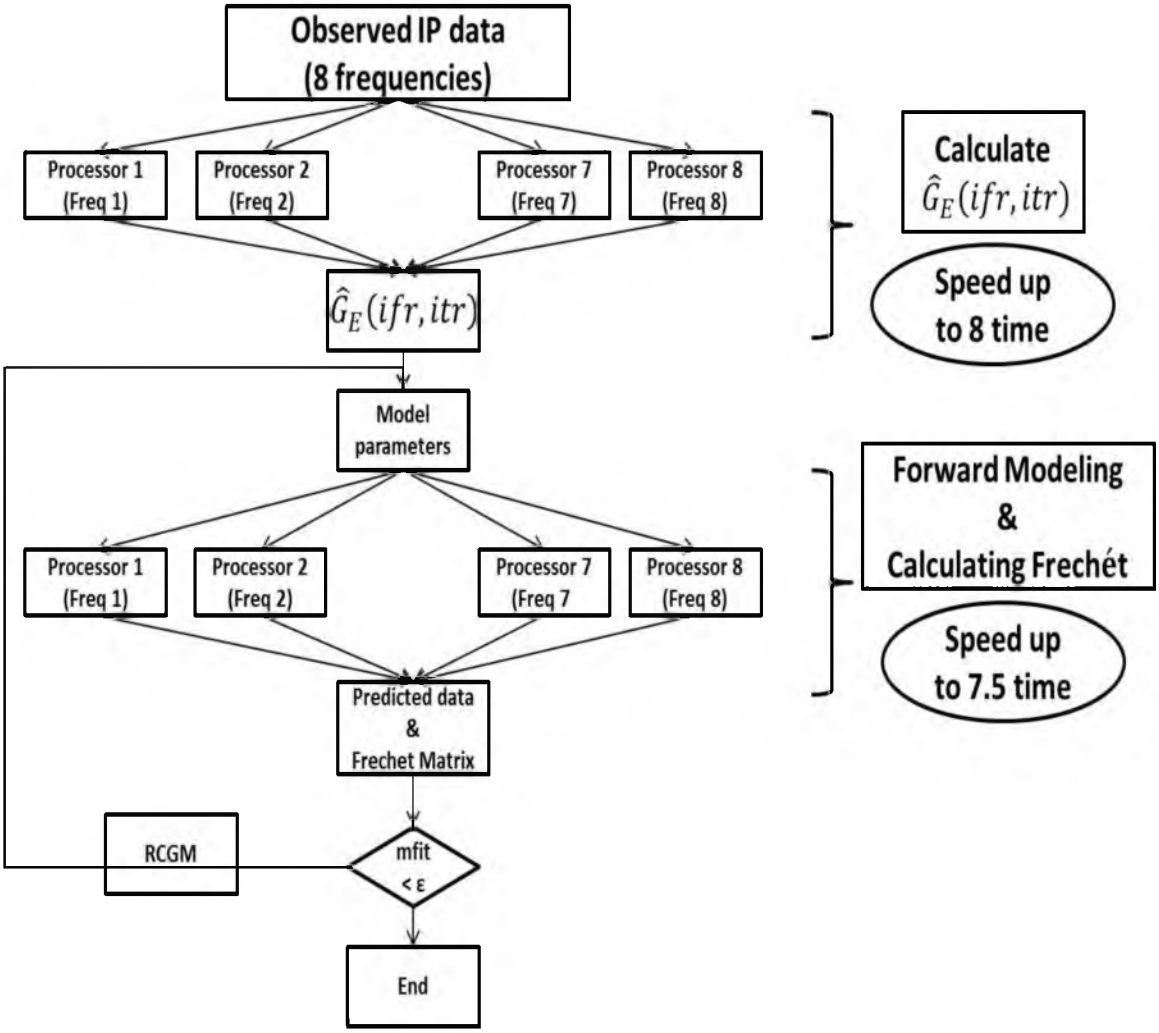

Figure 4.1 Flow-process diagram using MATLAB's parallel computing toolbox based on synthetic Model 4

CHAPTER 5

FEASIBILITY STUDY OF INVERSION

Modeling induced polarization (IP) phenomena is important for developing effective methods for remote sensing of subsurface geology and is widely used in mineral exploration. However, the quantitative interpretation of IP data in a complex 3D environment is still a challenging problem of applied geophysics. So I divided my research into several stages during which I solved this problem step by step.

As we know, 3D inversion processing means that there is no longer a need to place receiver and transmitter electrodes in a co-linear array. Electrode arrays can now be designed to optimise target definition and data collection efficiency (White et al., 2003). In synthetic studies, I choose bipole and dipole-dipole survey configurations to see whether the target with IP effect can be recovered accurately.

5.1 Multiple-parameters Inversion Based on Cole-Cole Model 1

In this stage, I will use the complex resistivity based on Cole-Cole relaxation model as observed data and use Regularized Conjugate Gradient Method (RCGM) to invert for the three parameters chargeability (η), time parameter (τ), and relaxation parameter (C) of Cole-Cole model.

In synthetic model 1, I adopt complex resistivity as observed data, which are simulated by fixed four parameters (shown in Table 5.1) to invert the three parameters (η), time parameter (τ), and relaxation parameters (C). In order to test how well the inversion algorithm deals with the noise, I designed two cases, pure observed data and the data with 2% random noise. In the inversion process, I chose the decay coefficients of the regularized parameter q as 0.8, misfit conditions are set as 0.1% and 2% respectively. For pure data, after 328 iterations, the normalized misfit (shown in Fig 5.1 and Fig 5.2) reached with the 0.1% misfit condition. For the noisy data, iterations stopped at 106 with 2% misfit condition (shown in Fig 5.3 and Fig 5.4). Comparison the observed and predicated data shows that the two cases fit quite evenly under 2% noise level. The comparisons between true models, initial models and final values of the three parameters η, τ and C are shown in Table 5.1.

Next I moved to the real sample D4-3 (Fig 5.5), which is from the Akah Formation (Utah). It is dominated by evaporates that are interbedded with open marine carbonate rocks and shoaling-up carbonate buildups to the west, and terrigenous clastic rocks to the north-northeast. The pyrite inclusions are thought to be deposited as a replacement mineral for some of the organic material and for this reason are disseminated (Phillips, 2010). The real and imaginary part of resistivity of the sample D4-3 measured in lab directly is used as observed data to invert the three parameters chargeability (η), time parameter (τ), and relaxation parameter (C) as well. I chose the same decay coefficients of the regularized parameter q as 0.8, misfit conditions are set as 0.01%. According to compare my result with the result (Phillps, 2010) shown in Table 5.2 find our algorithm can fit the curves better (shown in Fig 5.6 and Fig 5.7).

Table 5.1 Comparison between the true, initial, and final value based on Model 1

Cole-Cole Parameters	True Value	Initial Value	Final Value (no noise) [328 iterations / 0.1% misfit]	Final Value (2% noise) [106 iterations / 2% misfit]
η	0.7	0.1	0.699	0.6826
τ	0.01	0.1	0.0099	0.0099
C	0.4	0.1	0.4014	0.4036

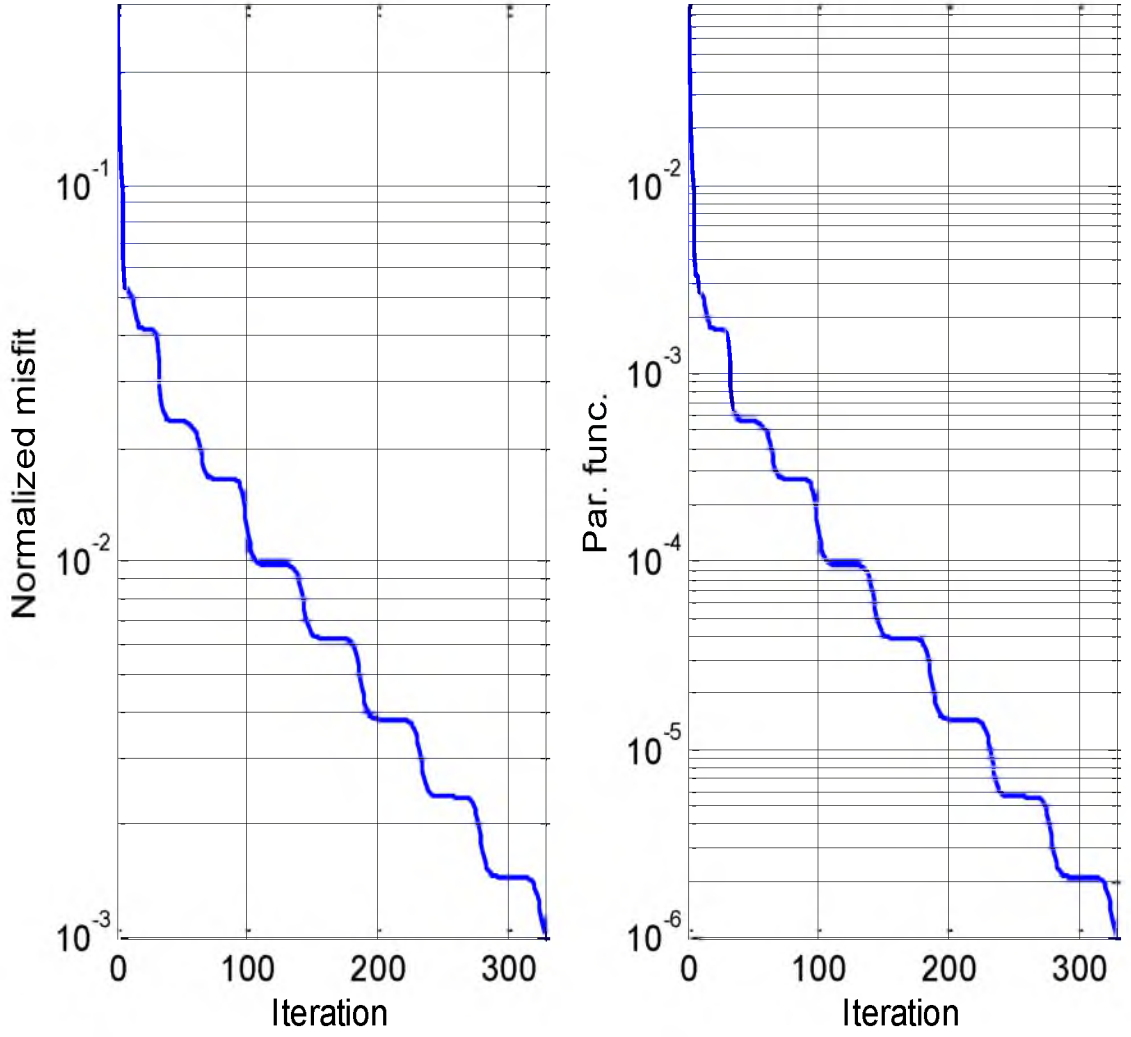

Figure 5.1 Model 1. The figure shows the normalized misfit and parametric functional varies with iteration.

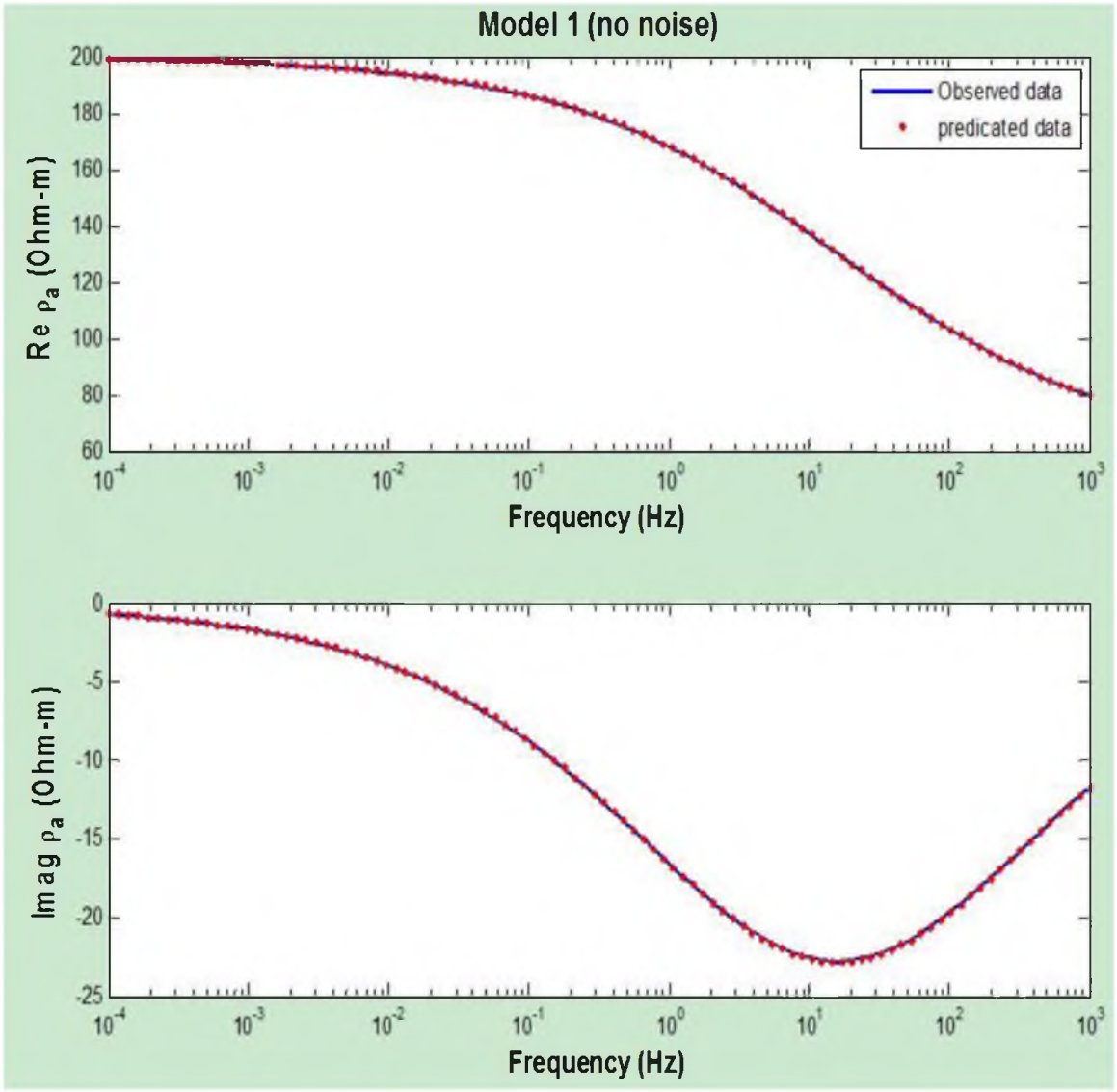

Figure 5.2 Model 1. The comparison between observed and predicated data without noise.

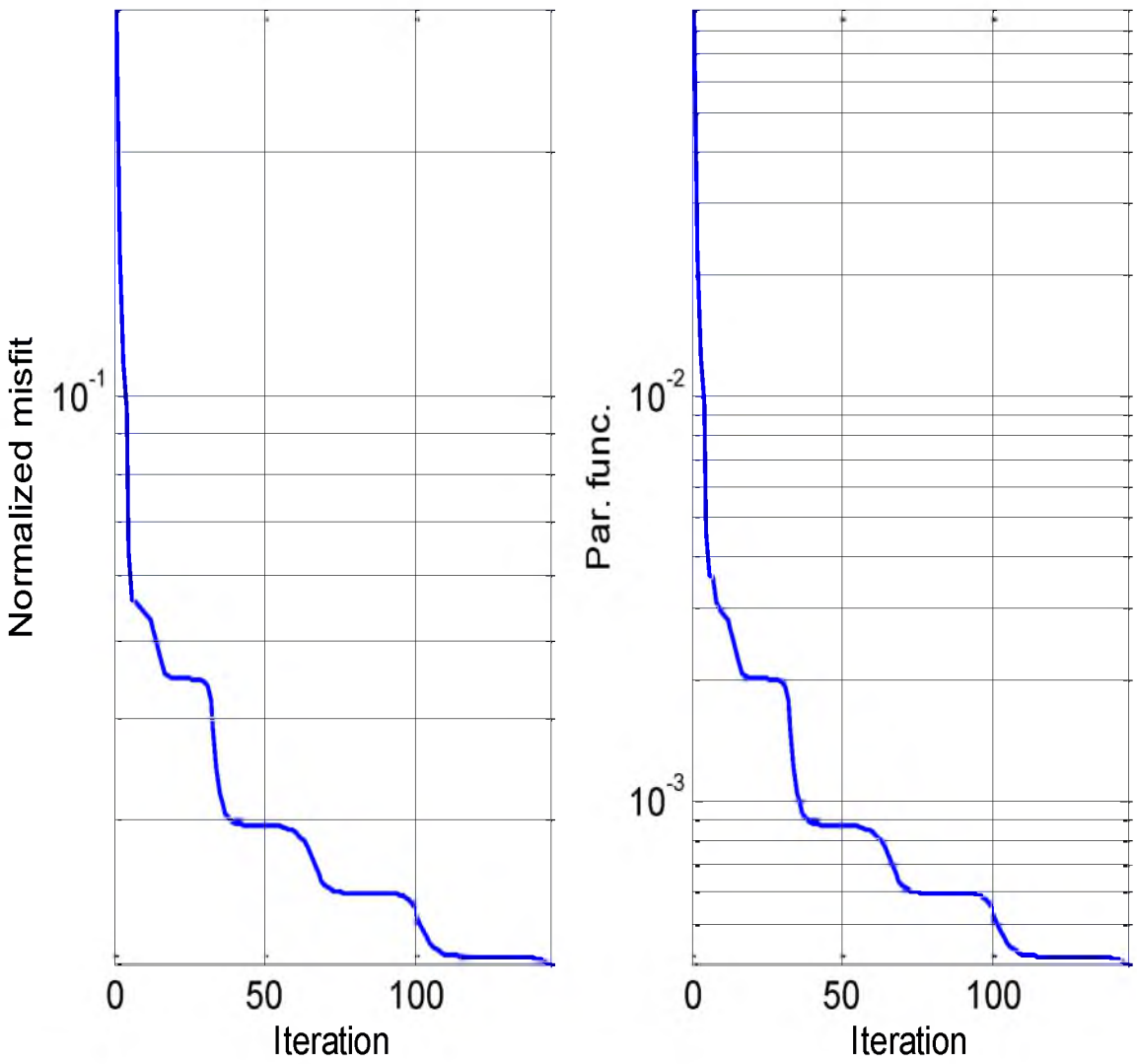

Figure 5.3 Model 1. The normalized misfit and parametric functional varies with iteration.

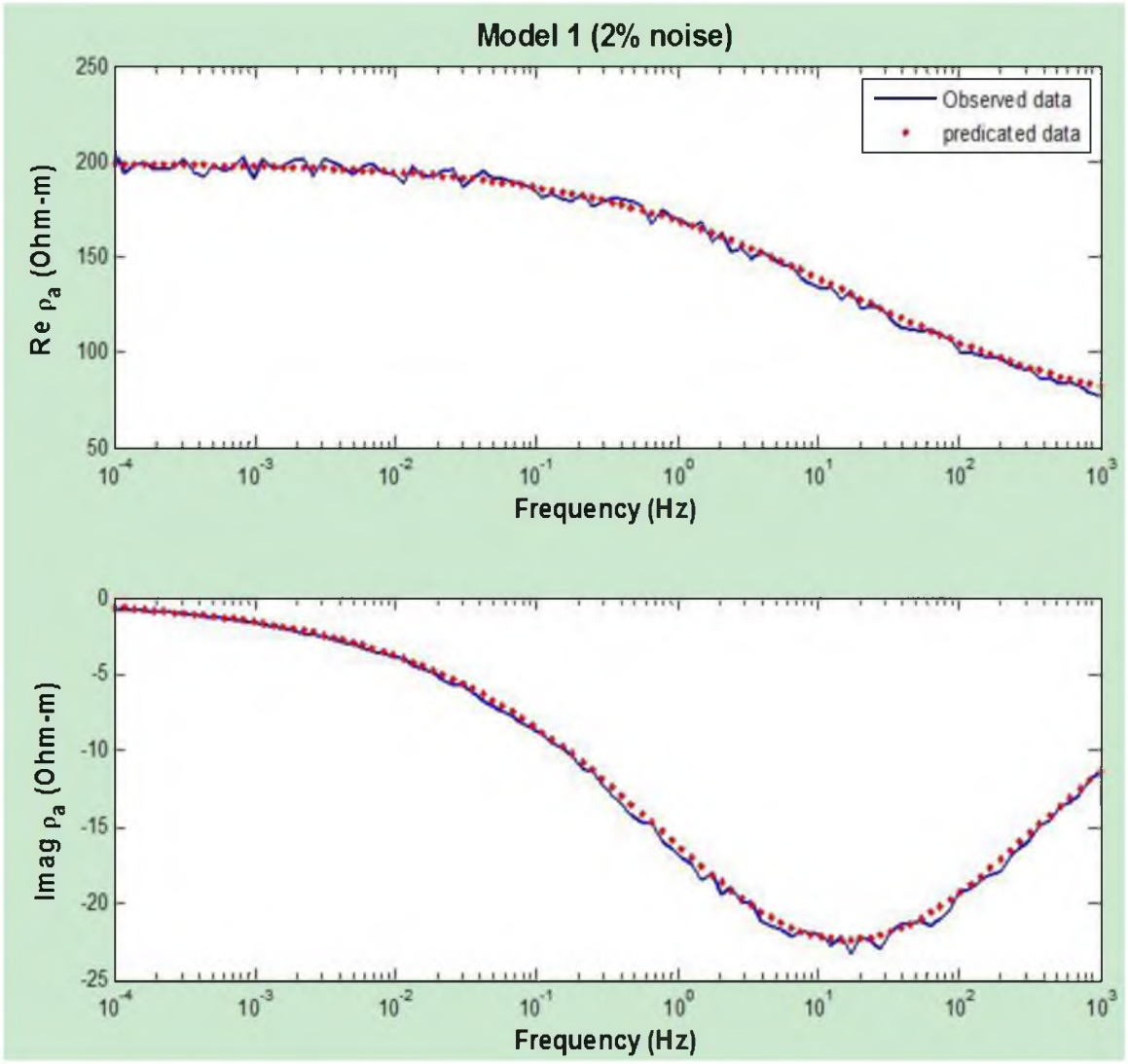

Figure 5.4 Model 1. The comparison between observed and predicated data with 2% noise.

Figure 5.5 Sample D4-3 is come from Akah Formation, Suan Juan County, Utah. It is an organic rich carbonate source rock with visible pyrite lenses under a hand lens. Sampled from a well depth of 6095 feet (Phillips, 2010).

Table 5.2 Comparison between the true, initial, and final value based on sample D4-3

Cole-Cole Parameters	**Phillps**	**Final Model (no noise) [320 iterations / 0.01% misfit]**
η	0.2	0.245
τ	0.005	0.0002
C	0.35	0.316

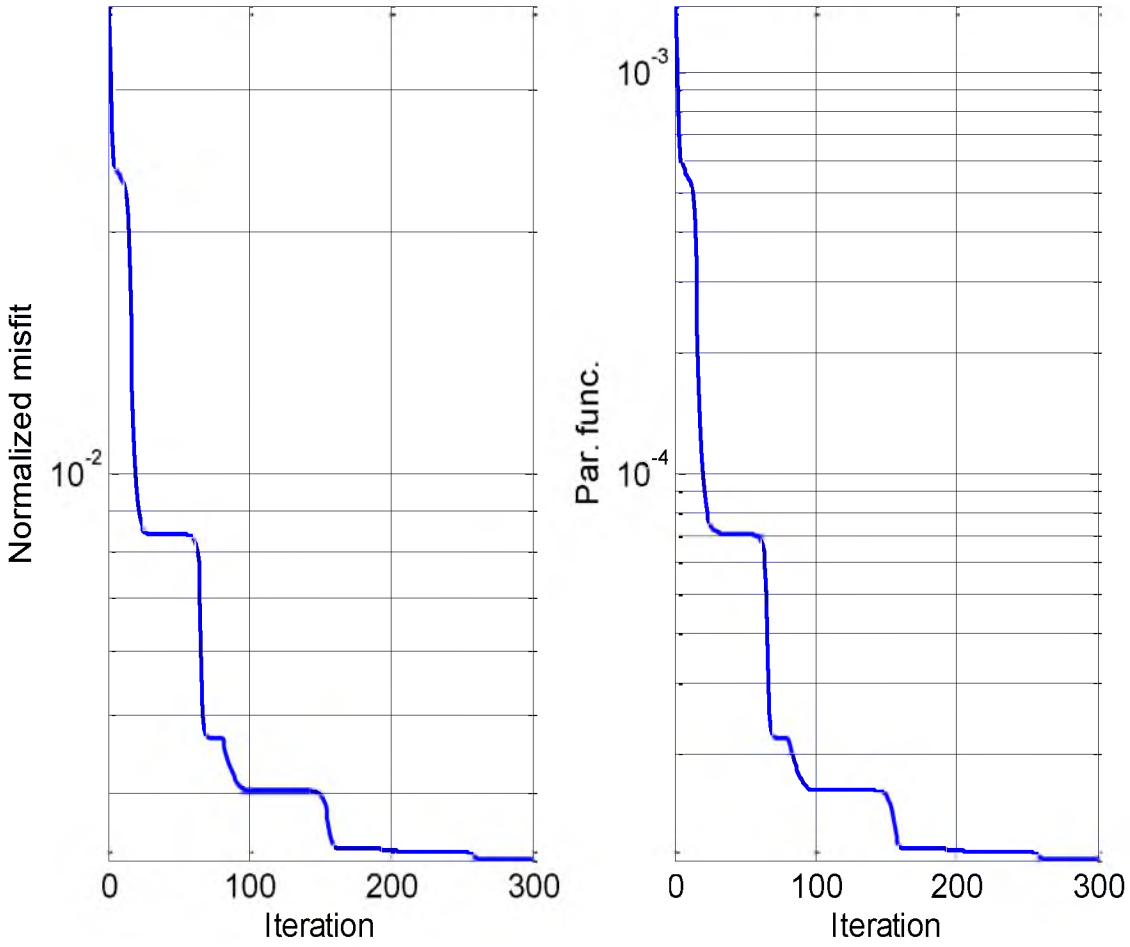

Figure 5.6 Sample D4-3. The figure shows the normalized misfit and parametric functional varies with iteration.

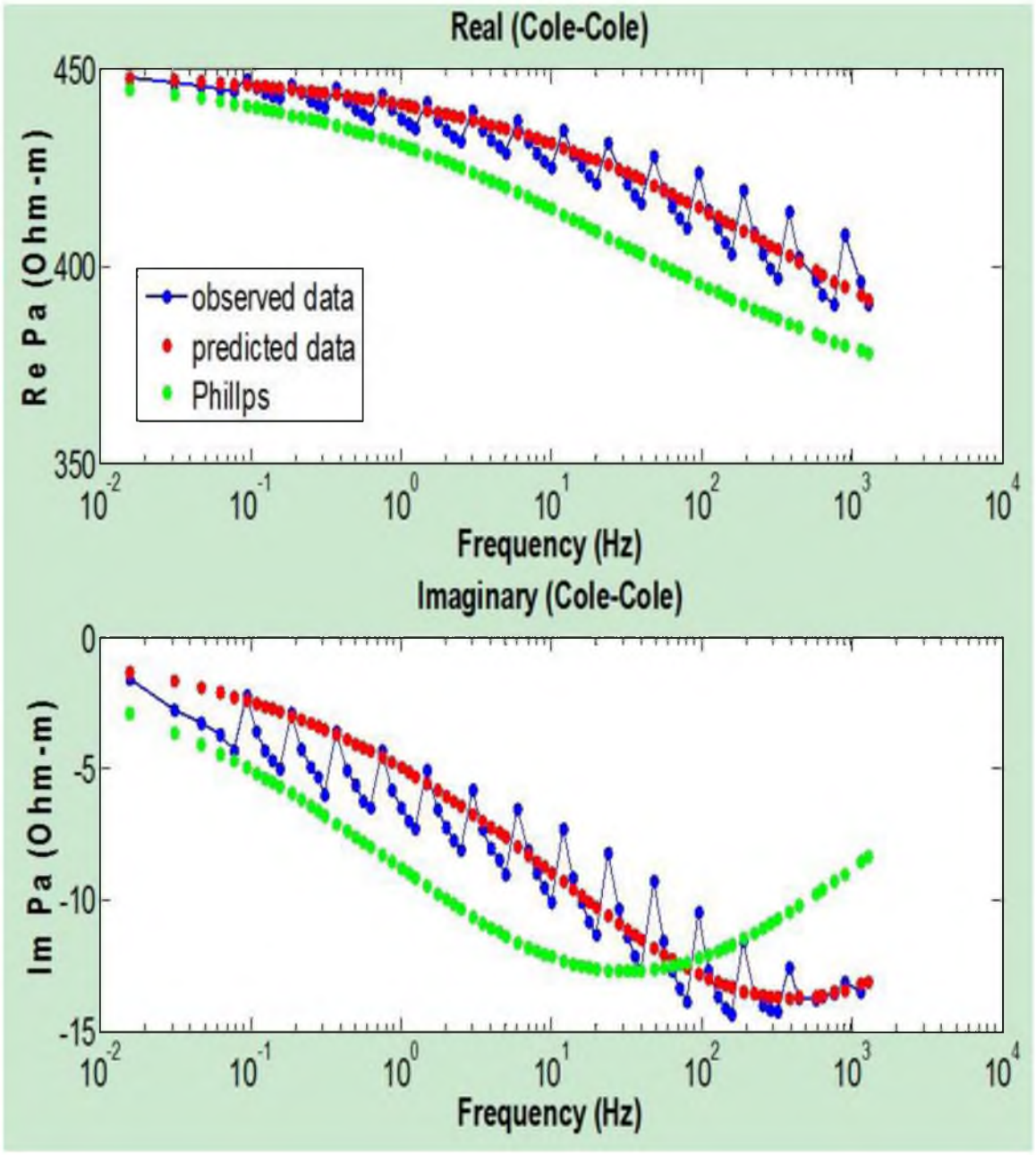

Figure 5.7 Sample D4-3. The figure shows the comparison between observed and predicated data.

5.2 Estimation of Cole-Cole Parameters Based on Fixed 3D Model 2

In synthetic model 2, I generate the synthetic EM data based on the typical geoelectrical models of the resistivity target that contain the IP effect within a homogeneous background.

Model 2 consists of one rectangular resistive body in a 100 Ohm-m homogenous background (Fig 5.8, bottom panel). The IP parameters of the conductivity defined by the Cole-Cole model (Eq. 3.14) are shown as a true model in Table 5.3. The body is located at the center of the y coordinate plane at a depth 100 m. The body sides in the x, y, and z direction have a length of 350 m, 350 m, and 200 m, respectively.

The electromagnetic field in the model is generated by a fixed electrical bipole transmitter (galvanic EM field excitation) and is simulated by the integral equation forward modeling code INTEM3DQIP using 10 frequencies: 0.1, 0.278, 0.77, 2.15, 6, 16, 46, 130, 360, 1000 Hz. The electric bipole in the model with galvanic excitation is parallel to the survey lines and is located at a distance of 5 km along the x-axes (Fig 5.8, top panel). The length of the bipole transmitter is 1 km. The receivers are located along 21 profiles deployed in the x-direction with 50 m separation. The length of the receiver profiles is 1 km. The EM stations are located every 50 m in a line. The total number of stations is 441. The synthetic observed data were not contaminated by noise.

The key point of this stage is that I know the exact position of the conductive target and assume all the three Cole-Cole parameters within each cell are the same during

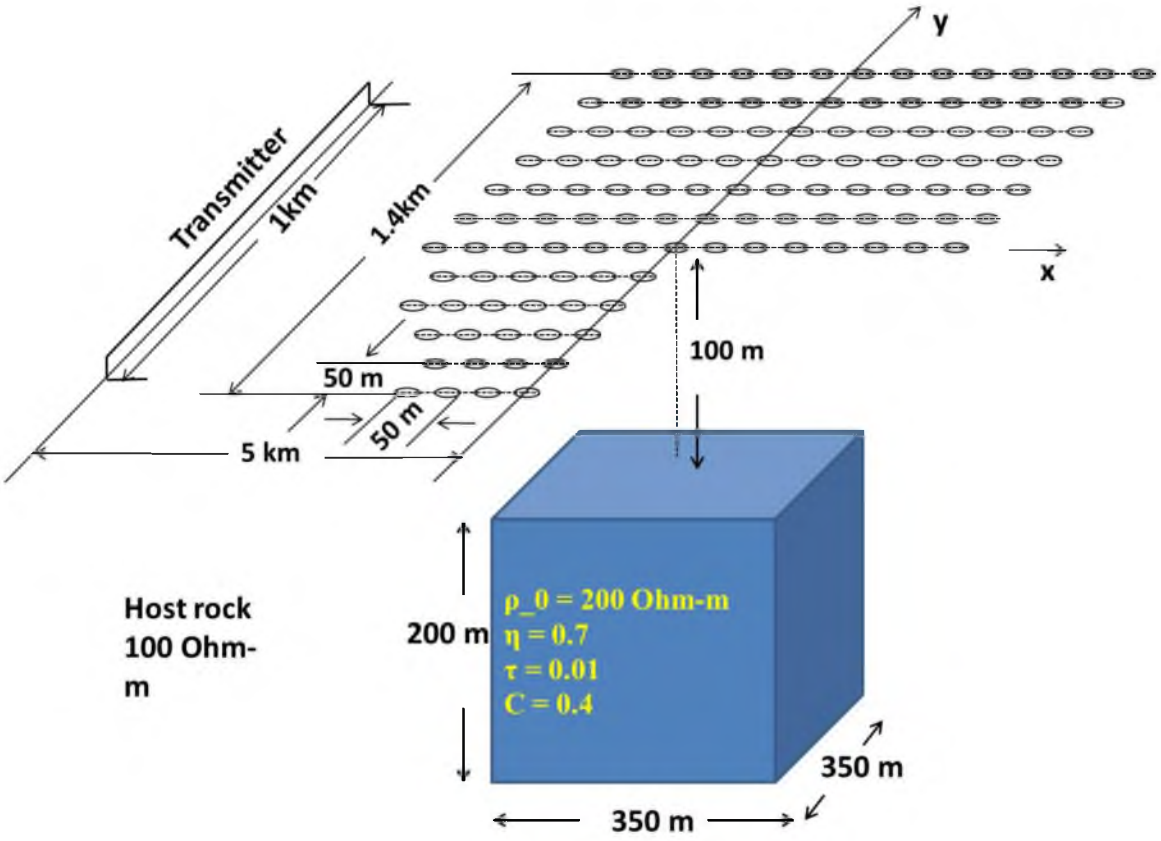

Figure 5.8 Model 2. Top panel shows the survey configuration. Bottom panel: The physical properties of the resistive body and host rock.

Table 5.3 Comparison between the true, initial, and final value based on Model 2

Cole-Cole Parameters	True Value	Initial Value	Final Value (2% noise)
η	0.7	0.1	0.7083
τ	0.01	0.1	0.0093
C	0.4	0.1	0.397

the whole inversion. In other words, the purpose of this test is whether the three Cole-Cole parameters can be estimated or not.

The result shows the predicted data match the observed data quite well (shown in Fig 5.9 and Fig 5.10). The information of parameters is shown in the Table 5.3. In Fig 5.9, the blue line for each parameter presents the true value (shown in Table 5.3). The red, green, and black lines which start from the initial model (shown in Table 5.3)

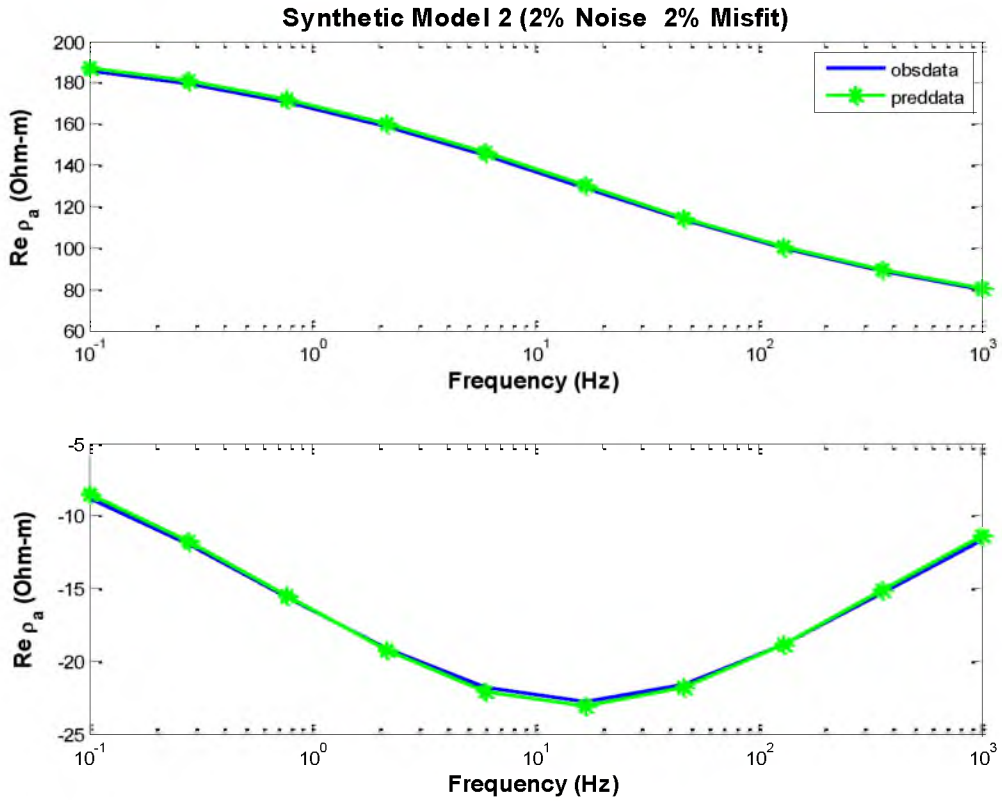

Figure 5.9 Model 2. The figure shows the comparison between observed and predicated data.

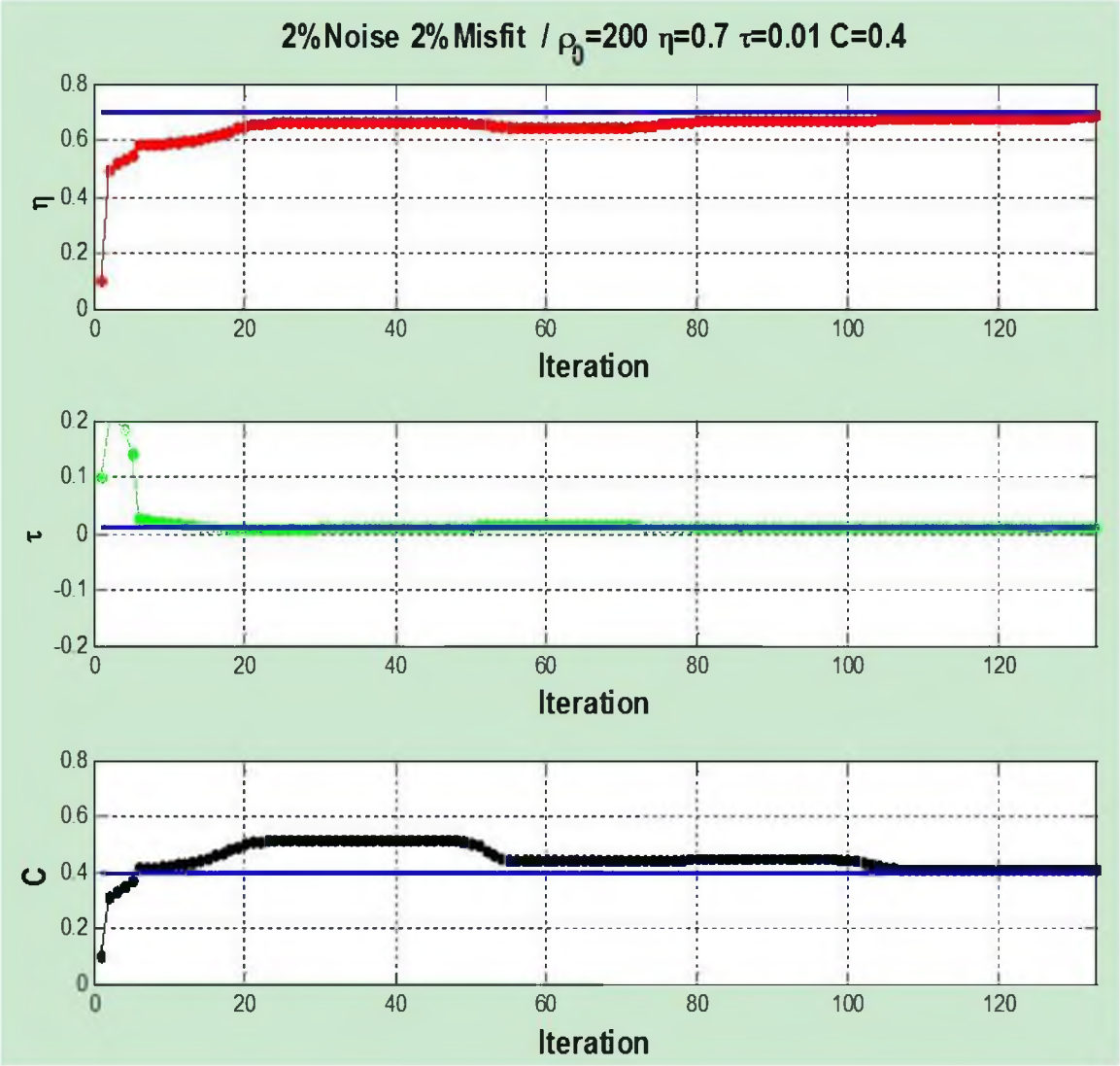

Figure 5.10 Model 2. The figure shows how fast η, τ, and C can touch the corresponding true value.

represent η, τ, and C, respectively. It shows that after about 60 iterations, all of the values of three parameters converge toward to the true value (blue line).

5.3 Inversion for 3D Distribution of Cole-Cole Model Parameters

The inversion of 3D IP data is an extremely difficult problem because it is complicated by coupling with the electromagnetic induction (EMI) effect. Some algorithms are used based upon linear forward modeling. However, the linear inversion ignores the nonlinear effects which are significant in IP phenomena. The goal of this dissertation is to develop a technique for rigorous nonlinear inversion of IP data that can be applied to both fixed electrical bipole transmitter data (Model 3) and multitransmitter data (Model 4) to get 3D distribution of four parameters of Cole-Cole model.

5.3.1 Model 3: Conductive and Resistive Anomaly in a Homogeneous Half Space Using Fixed Electrical Bipole Transmitter

Model 3 consists of two rectangular conductive and resistive bodies in a 100 Ohm-m homogenous background (Fig 5.11, top panel). The IP parameters of the conductivity defined by the Cole-Cole model (Eq. 3.14) are shown in Table 5.4.

The body is located at the center of the y coordinate plane at a depth 150 m. The body sides in the x, y, and z direction have a length of 150 m, 200 m, and, 150 m respectively. The four IP parameters were unknown, and the inversion was run for the

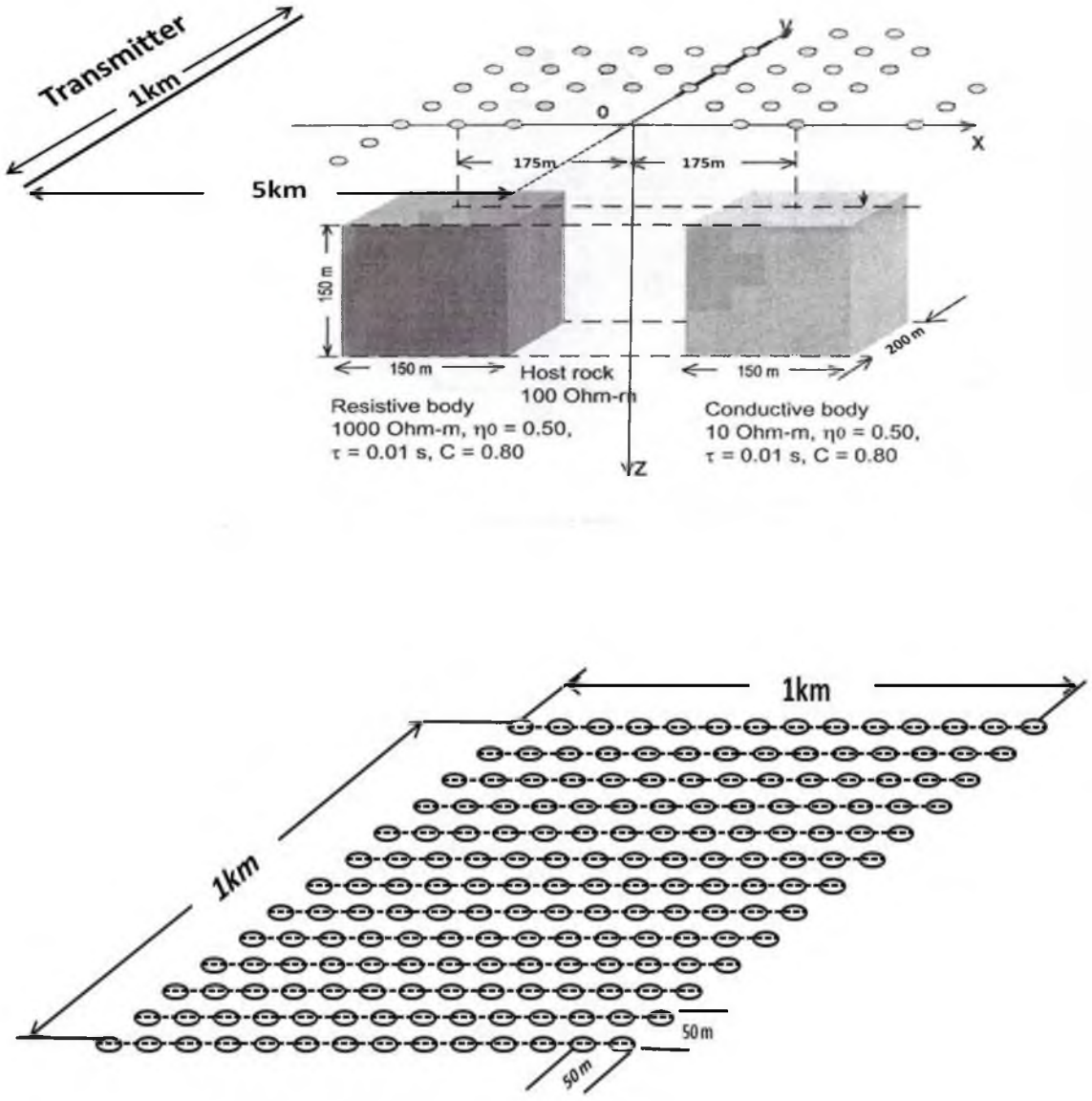

Figure 5.11 Model 3. Top panel: two rectangular conductive and resistive bodies in a 100 Ohm-m homogenous background. Bottom panel: configuration survey using fixed electrical bipole transmitter.

Table 5.4 The Cole-Cole parameters of conductive and resistive body

	Conductive body	Resistive body
ρ_0	10 Ohm-m	1000 Ohm-m
η	0.5	0.5
τ	0.01	0.01
C	0.8	0.8

four parameters DC conductivity (σ_0), chargeability (η), time parameters (τ), and relaxation parameters (C) at the same time. The inversion domain was subdivided into 2800 cells (20×20×70), with the size of each cubic cell being 50 m×50 m×50 m.

The electromagnetic field in the model is generated by a fixed electrical bipole transmitter (galvanic EM field excitation) and is simulated by integral equation forward modeling code INTEM3DQIP using eight frequencies: 0.125, 0.25, 0.5, 1, 2, 4, 8, 32, 64, 128, 256 Hz. The electric bipole in the model with galvanic excitation is parallel to the survey lines and is located at a distance of 5 km along the x-axes (Fig 5.11, bottom panel). The length of the bipole transmitter is 1 km. The receivers are located along 21 profiles deployed in the x-direction with 50 m separation. The length of the receiver profiles is 1 km. The EM stations are located every 50 m in a line. The total number of the stations is 441. The synthetic observed data were not contaminated by noise.

Fig 5.12 to Fig 5.15 show the inversion results which represent x-y section (z = 200 m), x-z section (y=0 m), and y-z section (x = 150 m) and 3D view of the anomaly respectively based on DC conductivity (σ_0), chargeability (η), time parameter (τ), and relaxation parameter (C). For conductivity (σ_0), chargeability (η), and time parameter (τ), the inversion results of these three parameters only recover both position and value of conductive body accurately. For relaxation parameter (C), the position of inversion result

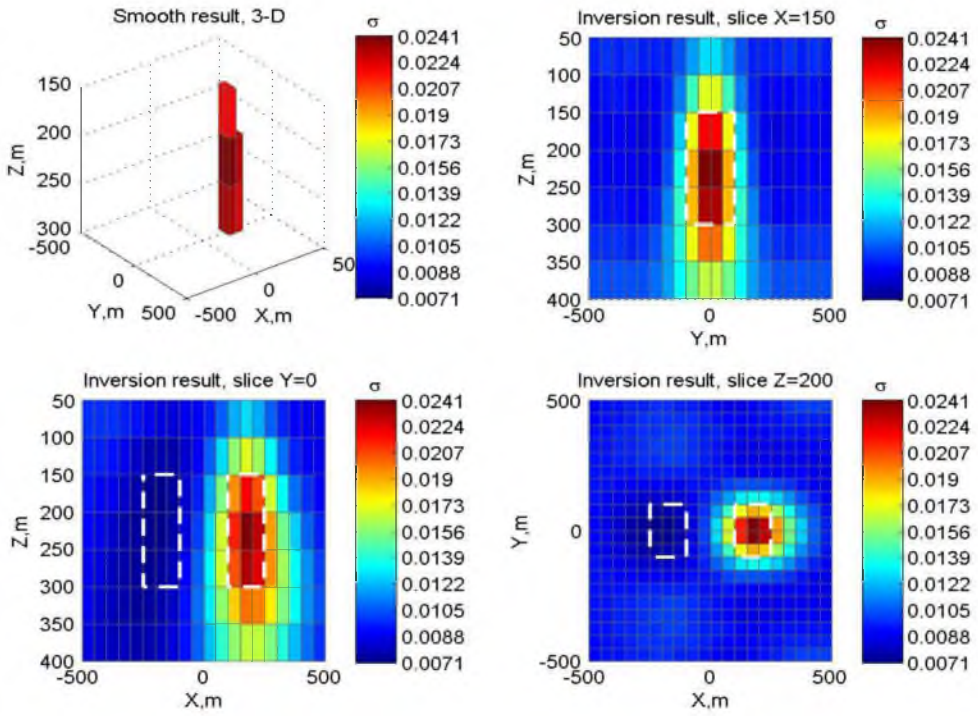

Figure 5.12 Model 3. The DC conductivity distribution obtained by IP data inversion.

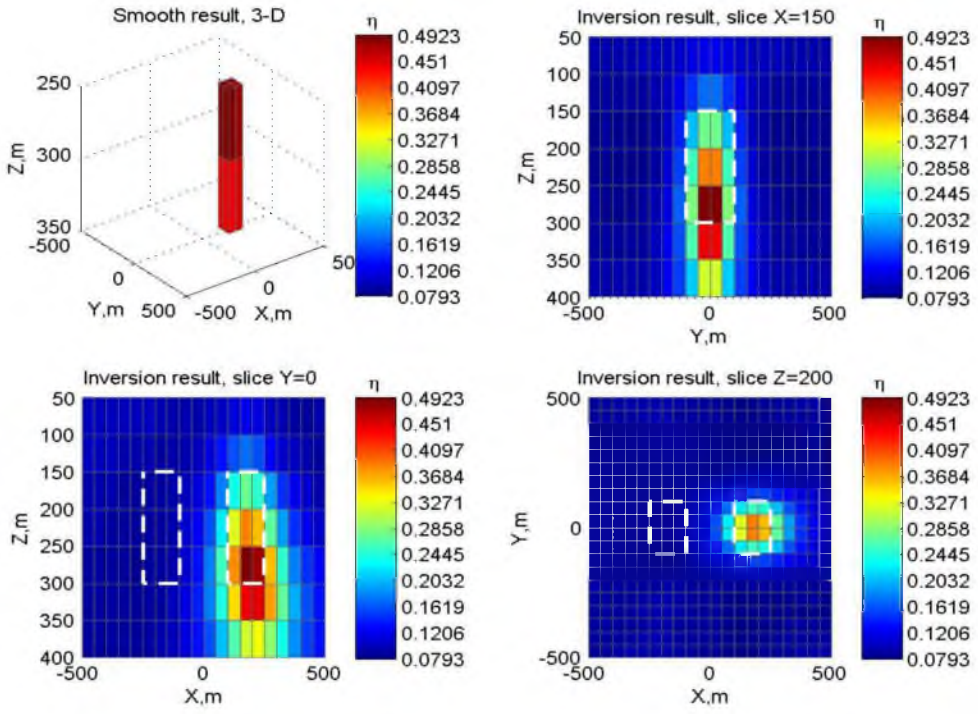

Figure 5.13 Model 3. The chargeability distribution obtained by IP data inversion.

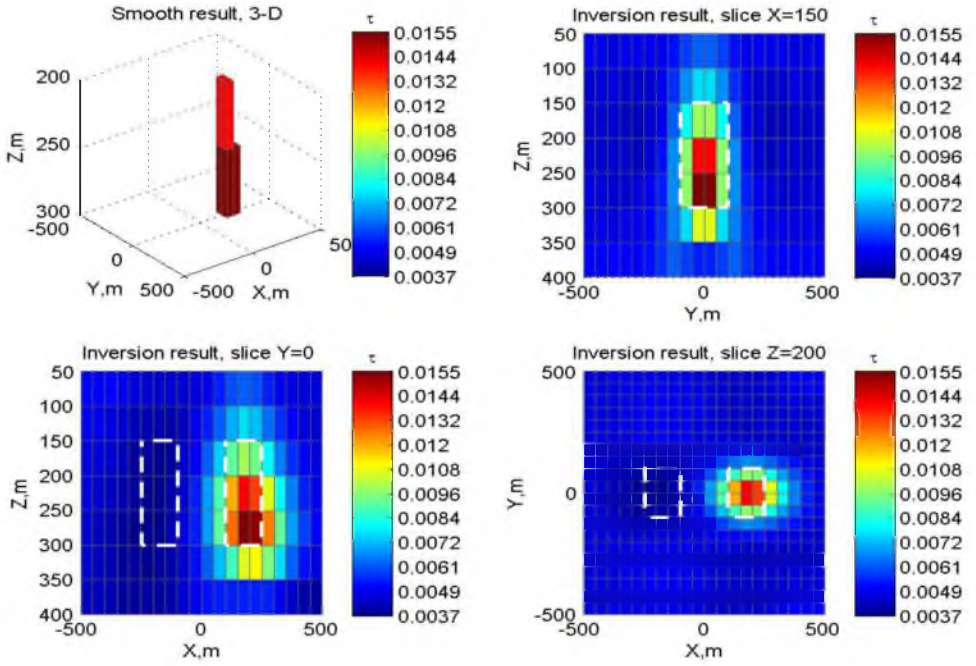

Figure 5.14 Model 3, the time constant obtained by IP data inversion.

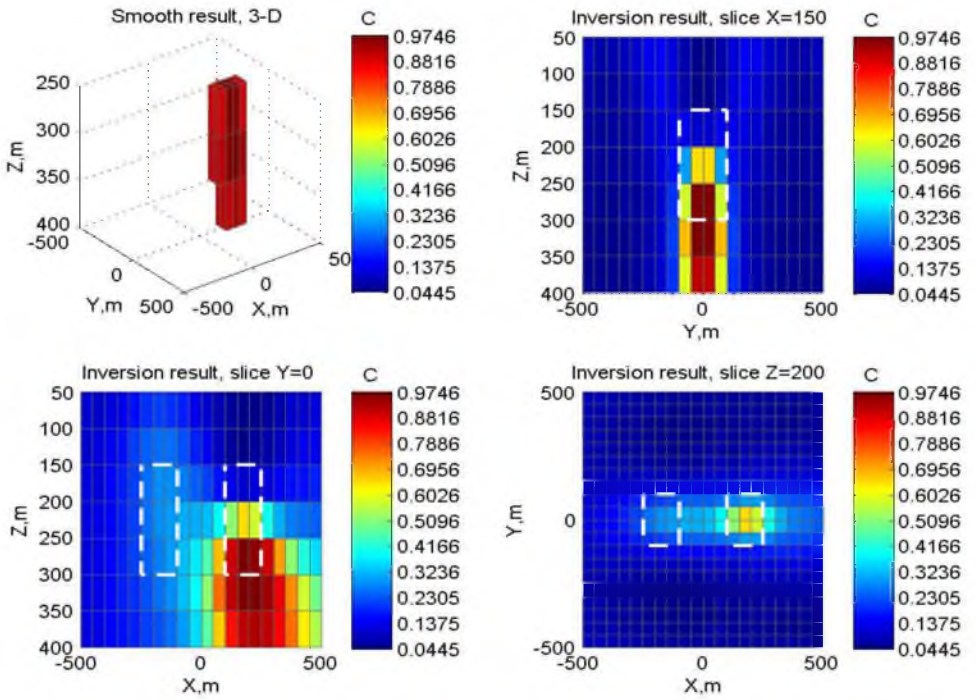

Figure 5.15 Model 3. The relaxation parameters distribution obtained by IP data .

is lower than the true position since among these four parameters, because C has the lowest sensitivity. Fig 5.16 shows the behavior of misfit, parametric function and α varying with iteration. Fig 5.17 and Fig 5.18 indicates the comparison between the real and imaginary E_x part of observed and predicted data of each frequency and they fit quite well.

5.3.2 Model 4: Conductive and Resistive Anomaly in a Homogeneous Half Space Using Multiple Dipole Transmitters

Model 4 has the same shape and position of the anomalous bodies as Model 3 (Fig 5.19, a). The electromagnetic field in Model 4 is generated by electric bipole transmitters with a length of a = 100 m (galvanic EM field excitation) and is measured by electric bipole receivers of the same length. The transmitters and receivers are positioned along a profile. For each transmitter position, there are up to six receivers located at a distance ***na*** from the end of the bipole transmitter, where ***n*** = 1, 2, ..., 6, respectively. So there are 25 transmitters in one profile of 2.6 km length (Fig 5.19, b). For the transmitters located at the right-hand side of the profile, the number of the corresponding receivers is reduced respectively so that, for transmitter number 25, there is just one receiver (Fig 5.20).

The synthetic EM data for this model were generated using the integral equation forward modeling code INTEM3DQLIP as well. I used eight frequencies: 0.25, 0.5, 1, 2, 4, 8, 16, and 32 Hz. The area of the inversion was subdivided into 1960 cells (20×14×7),

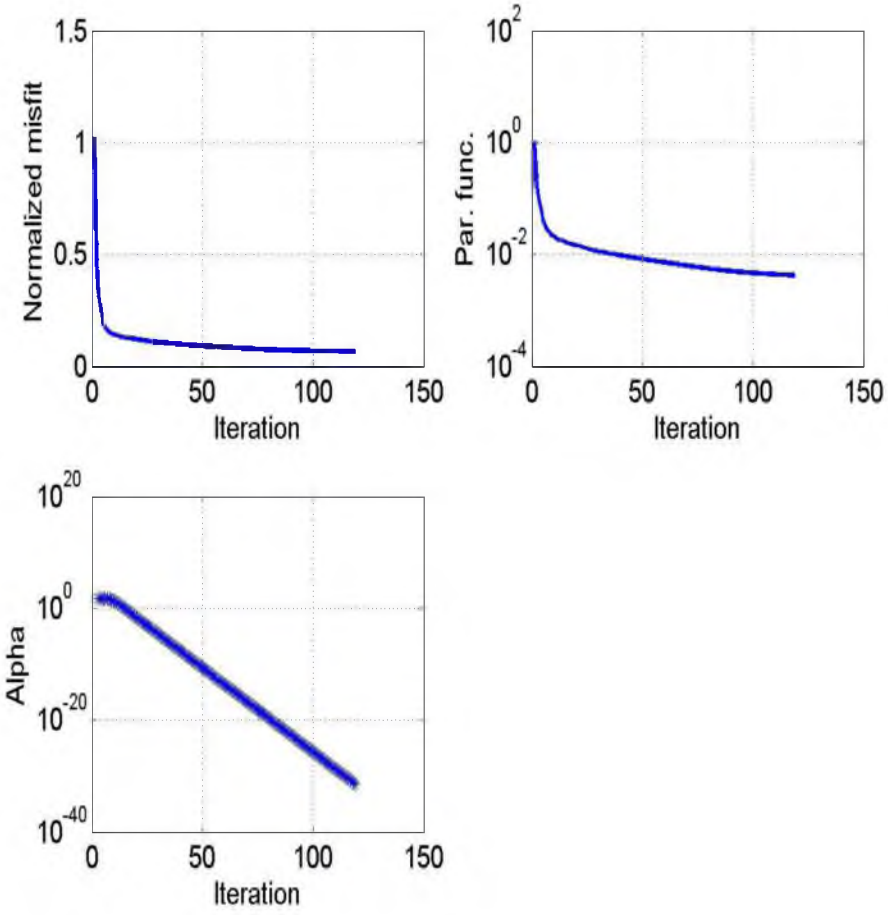

Figure 5.16 Model 3. The behavior of misfit, parametric function and alpa.

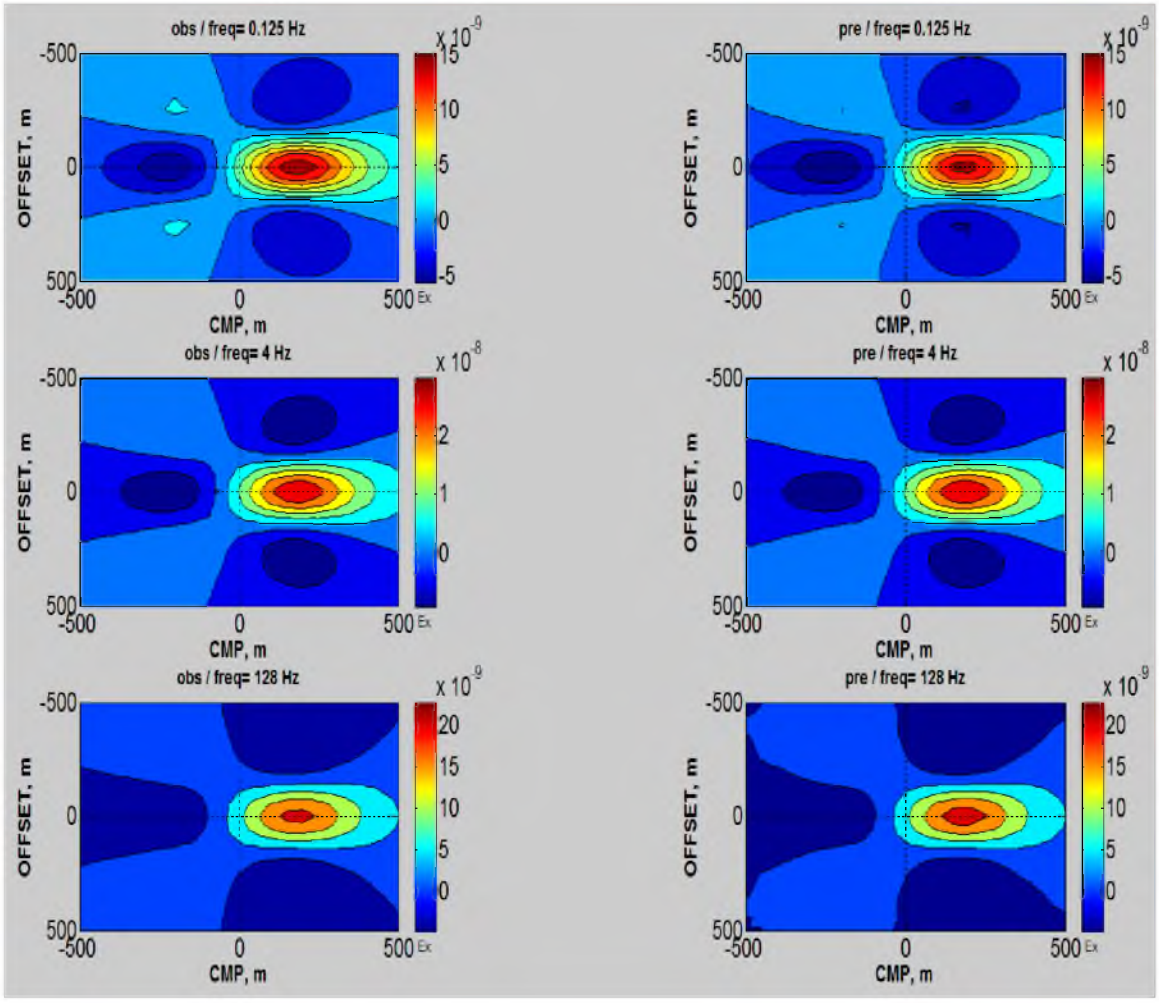

Figure 5.17 Model 3. The comparison of the real E_x part of predicted and observed data for each frequency.

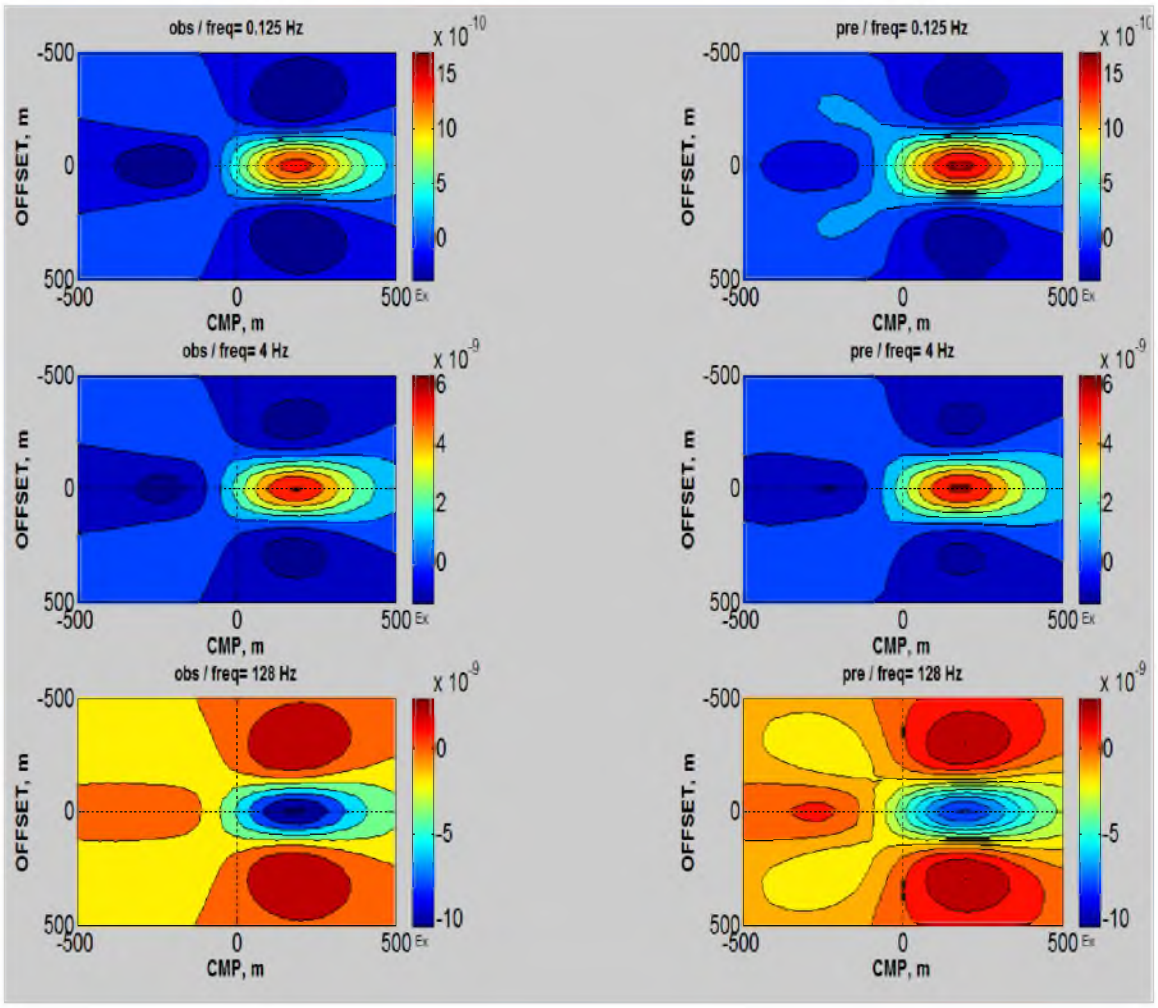

Figure 5.18 Model 3. The comparison of the imaginary E_x part of predicted and observed data for each frequency.

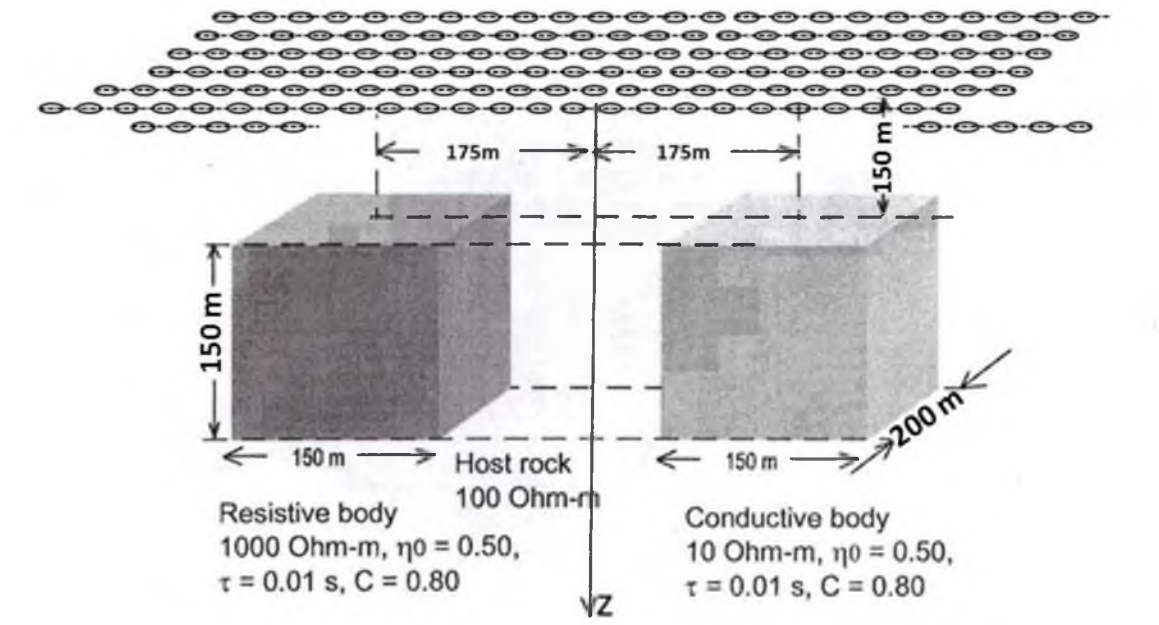

(a)

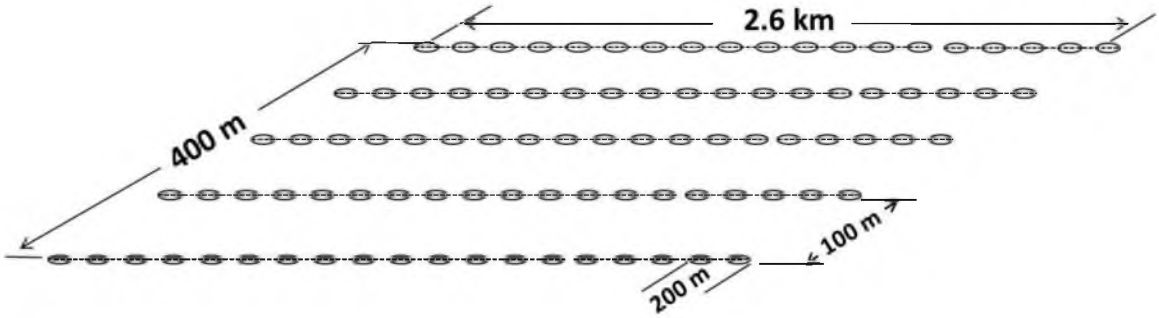

(b)

Figure 5.19 Model 4: a) Two rectangular conductive and resistive bodies in a 100 Ohm-m homogenous background. b) Configuration survey using mutil-transmitters.

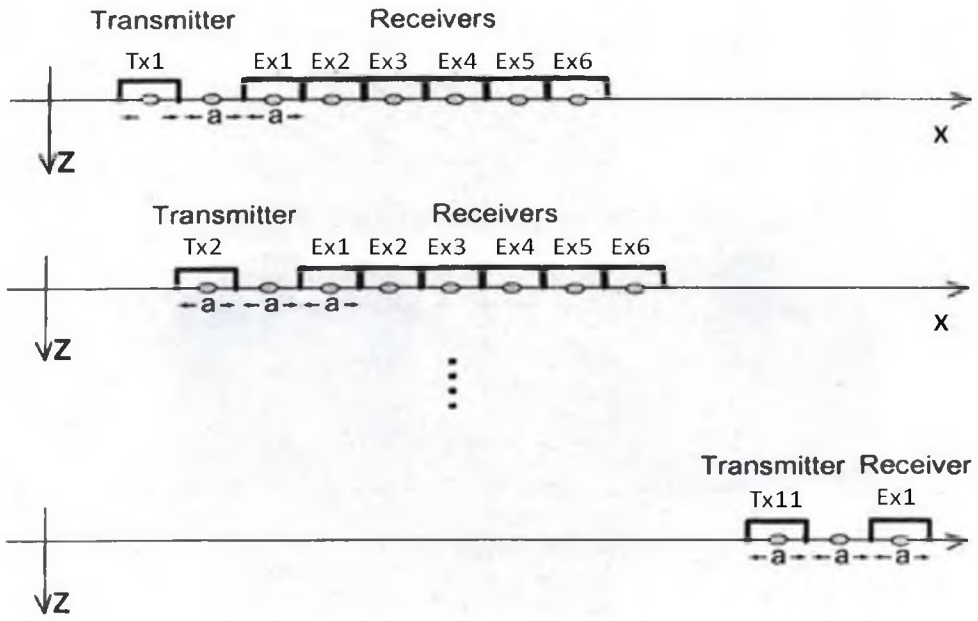

Figure 5.20 Model 4. The configuration of IP receivers and transmitters survey.

with the size of each cubic cell 50 m × 50 m × 50 m. the inversion was run simultaneously for the four parameters (σ_0, η, τ, and C).

Fig 5.21 to Fig 5.24 show the inversion results which represent x-y section (z = 200 m), x-z section (y=0 m), and y-z section (x = 150 m) and 3D view of the anomaly respectively based on DC conductivity (σ_0), chargeability (η), time parameter (τ), and relaxation parameters (C). For conductivity (σ_0), chargeability (η), and time parameter (τ), comparing with inversion results of Model 3, except for conductive body, it shows that the inversion results of these three parameters can recover both value of the resistive body much better, especially for DC conductivity (σ_0) which is primary parameter. The resolution of multiple transmitter configurations is much better than in the fixed electrical bipole case. For relaxation parameters (C), the position of inversion anomaly is still lower than the true position because C has the lowest sensitivity even using multiple transmitter configurations. Fig 5.25 indicates the comparison between the observed and predicted data of each frequency along the middle receiver line and they fit well.

5.4 Sensitivity Analysis of Cole-Cole Parameters Based on 3D Inversion

The EM field generated by the transmitters propagates through the geologic formations according to Maxwell's equations. I can represent a numerical solution of the system of Maxwell's equations in the form of a discrete operator equation:

$$d = A_E(\Delta\tilde{\sigma}) = A(m) \tag{5.1}$$

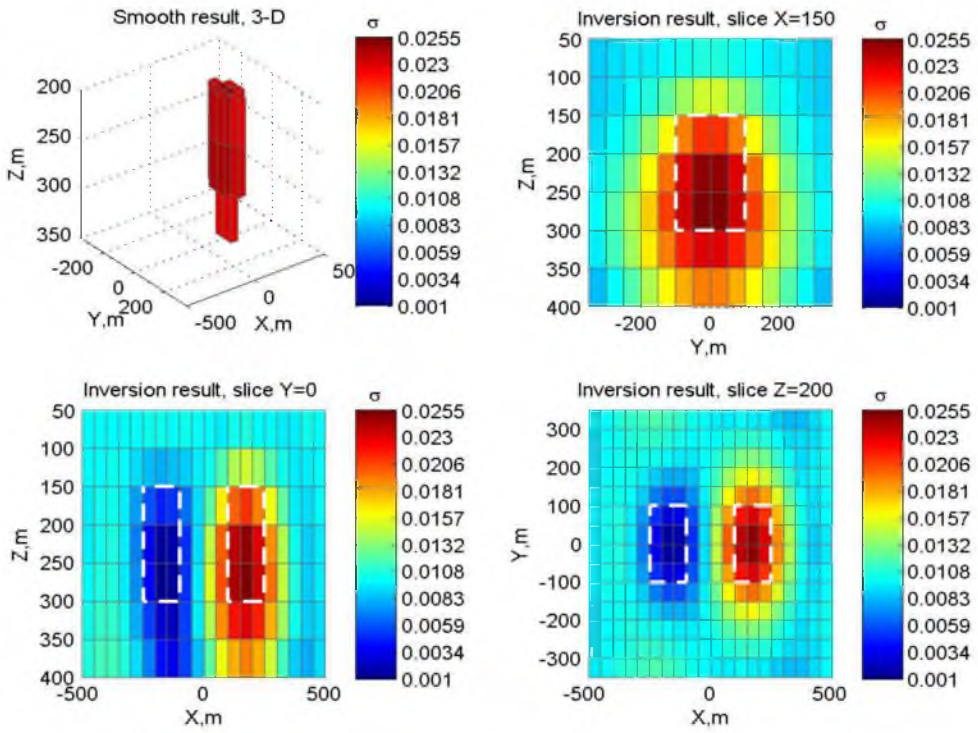

Figure 5.21 Model 4. The DC conductivity distribution obtained by IP data inversion.

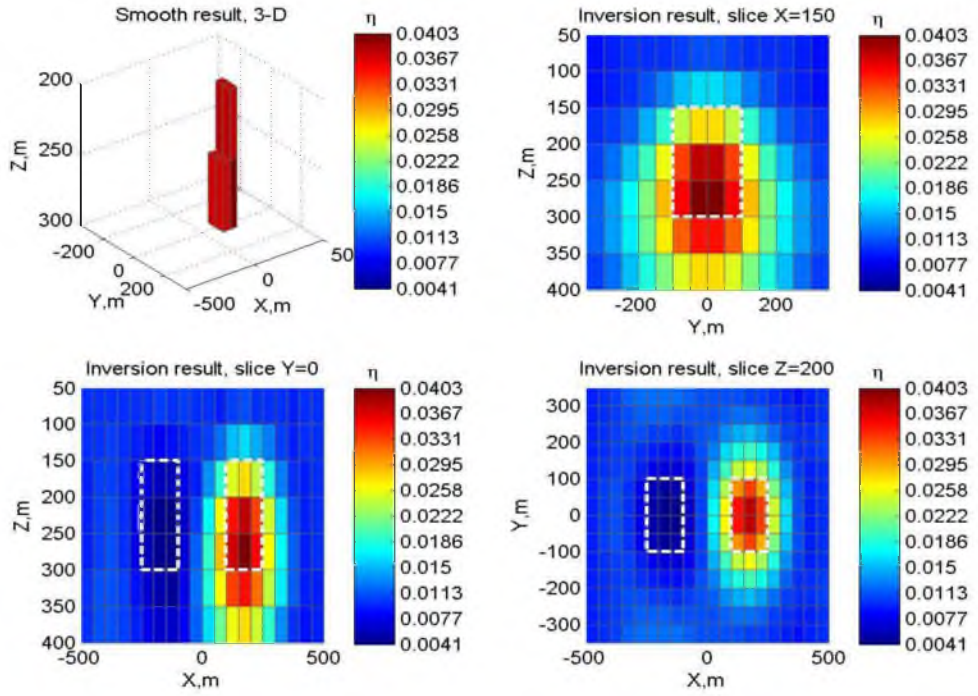

Figure 5.22 Model 4. The chargeability obtained by IP data inversion.

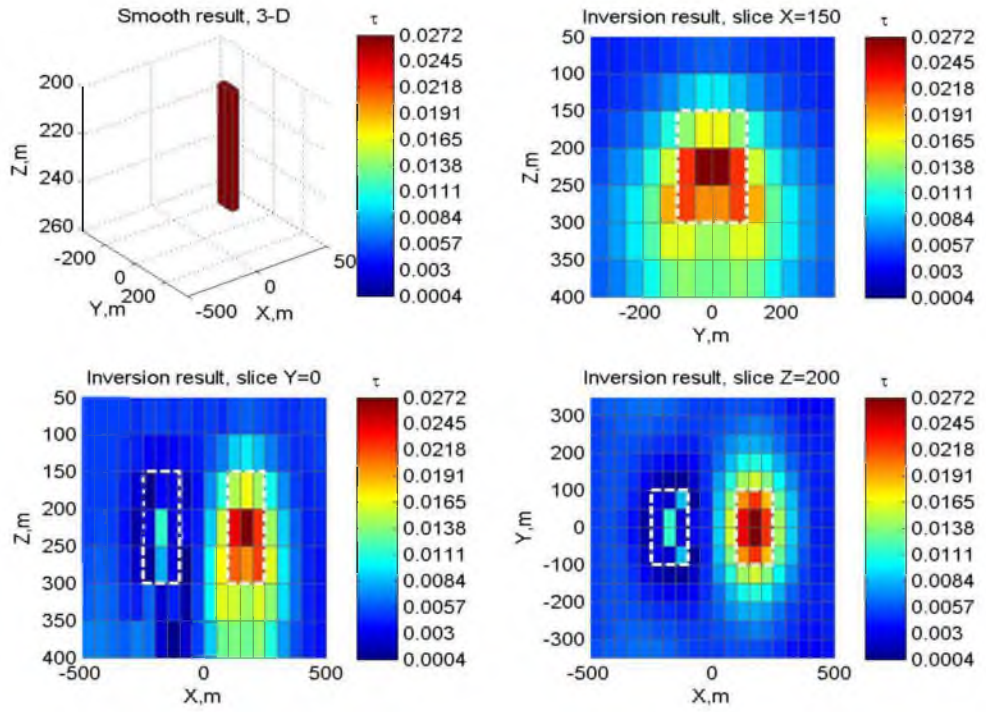

Figure 5.23 Model 4. The time constant distribution obtained by IP data inversion.

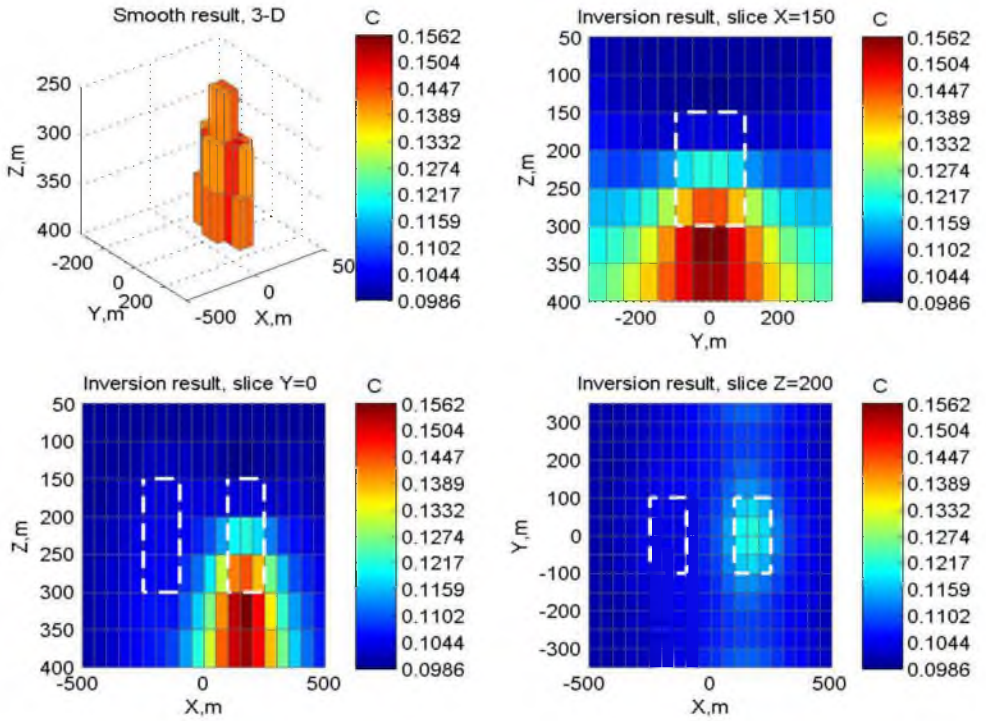

Figure 5.24 Model 4. The relaxation parameter obtained by IP data inversion.

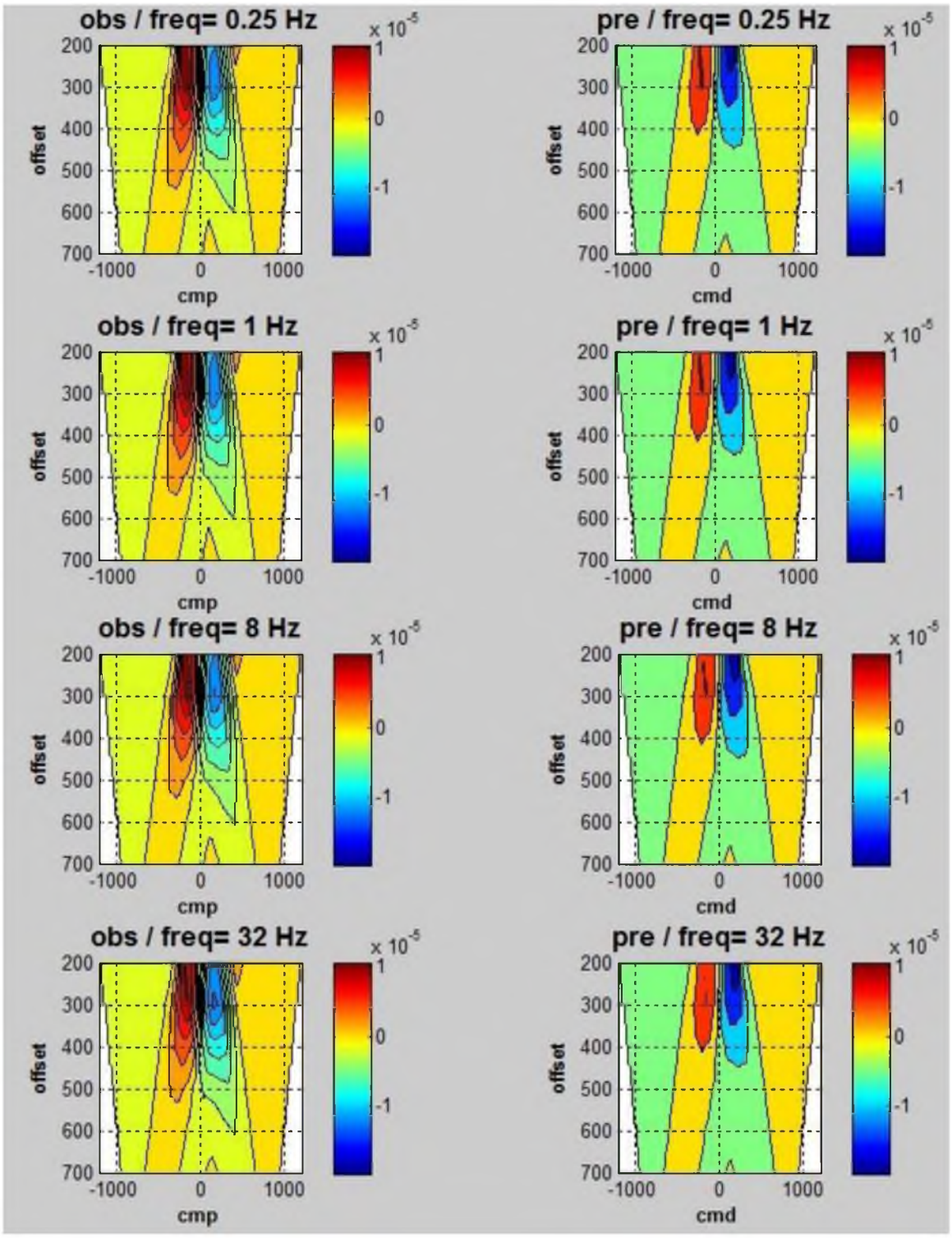

Figure 5.25 Model 4. The comparison of predicted data and observed data for four frequencies on the center profile.

where d is a vector of the observed EM data, A is a nonlinear operator transforming the Cole-Cole parameters into the electric field and m is a vector formed by a distribution of the four Cole-Cole model (σ_0, η, τ and C) in the subsurface describing by formula.

$$\Delta\tilde{\sigma} = \sigma_0\left(1 - \eta\left(1 - \frac{1}{1+(i\omega\tau)^C}\right)\right)^{-1} - \sigma_b \tag{5.2}$$

Applying the variational operation to both sides of formula, I obtain:

$$\delta d = F\delta(\sigma_0, \eta, \tau, C) \tag{5.3}$$

where F is the Fréchet derivative matrix consisting of the partial derivative of data with respect to the four parameters σ_0, η, τ and C.

Let us analyze the sensitivity of the EM data to the perturbation of one of the specific parameters, $\delta\sigma_k$. To solve this problem, the formula in matrix notations can be wrote as follows:

$$\delta d_i = F_{ik}\delta\sigma_k \tag{5.4}$$

In the last formula, F_{ik} are the elements of the Fréchet derivative matrix F of the forward modeling operator, and there is no summation over index k. The norm of the perturbed vector of the data can be calculated as:

$$\|\delta d\| = \sqrt{\sum_i \delta d_i \cdot \delta d_i^*} = \sqrt{\sum_i (F_{ik}F_{ik}^*)}\,\delta\sigma_k \tag{5.5}$$

The integrated sensitivity of the data to parameter $\delta\sigma_k$ is determined as the ratio (Zhdanov, 2002):

$$S_k = \frac{\|\delta d\|}{\delta\sigma_k} = \sum_i (F_{ik}F_{ik}^*) \tag{5.6}$$

One can see that the integrated sensitivity of the data to the different parameters $\delta\sigma_k$ varies because the contributions of the different parameters to the observation are

also variable. The diagonal matrix with diagonal elements equal to $S_k = \frac{\|\delta d\|}{\delta \sigma_k}$ is called an integrated sensitivity matrix

$$\mathbf{S} = \mathrm{diag}(\textstyle\sum_i (F_{ik} F_{ik}^*)) = \mathrm{diag}(\mathbf{F}^* \mathbf{F})^{1/2} \tag{5.7}$$

Matrix S is formed by the norms of the columns of the Fréchet derivative matrix F. Therefore, in order to compute the integrated sensitivity, one should determine the Fréchet derivative matrix F. In this dissertation, the observed data are usually normalized by the amplitude of the background field. In other words, I work with the weighted data. The weighted integrated sensitivity matrix can be expressed as

$$\mathbf{S_w} = \mathrm{diag}(\mathbf{F}^* \mathbf{W_d}^* \mathbf{W_d} \mathbf{F})^{1/2} \tag{4.8}$$

In this section, I use sensitivity to analyze the inversion results of synthetic Model 3 and Model 4.

5.4.1 Sensitivity Analysis of Synthetic Model 3

Fig 5.12 to Fig 5.15 show the result of the inversion for DC conductivity (σ_0), chargeability (η), time parameters (τ), and relaxation parameters (C) for synthetic Model 3 shown above. I found that the inversion based on σ_0, η, τ only can recover both position and value of the conductive target much more clearly and accurately than those of the resistive target. In order to make the interpretation about the phenomena, I pick up the value of Fréchet matrix of the first and last iteration based on the 9 middle column cells of the resistive and conductive targets (Fig 5.26) to use Eq. 5.7 to calculate corresponding nonweighted (Fig 5.27) and weighted integrated sensitivity (Fig 5.28 and Fig 5.29) for 6 frequencies and plot them together.

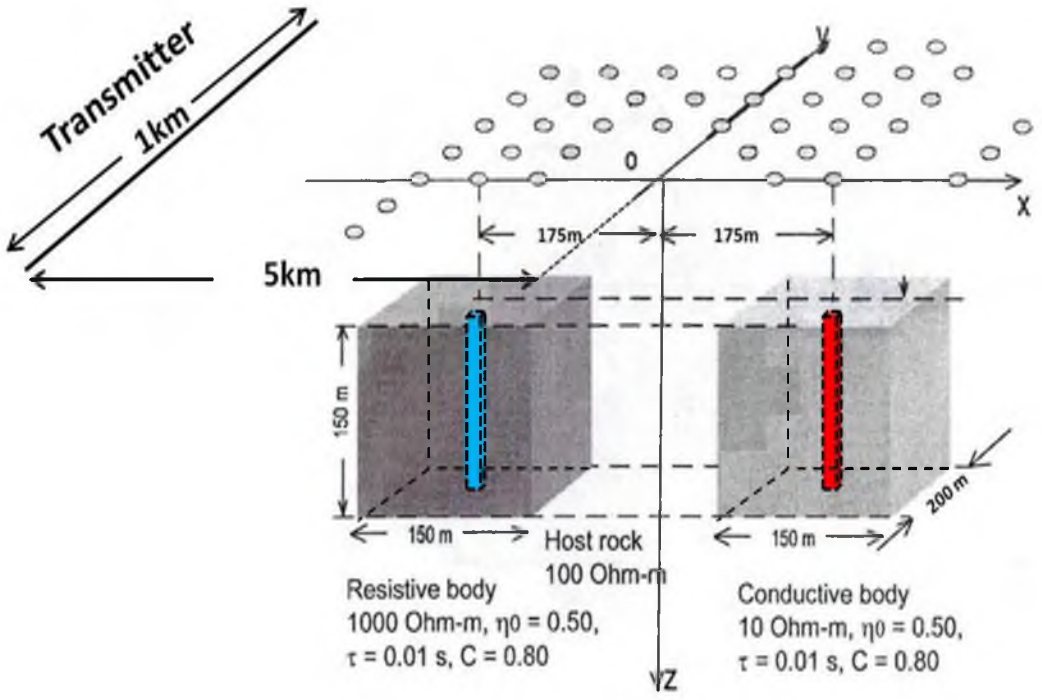

Figure 5.26 Sensitivity analysis based on synthetic Model 3. a) Center column cells (blue) of the resistive body, b) center column cells (red) of the conductive body.

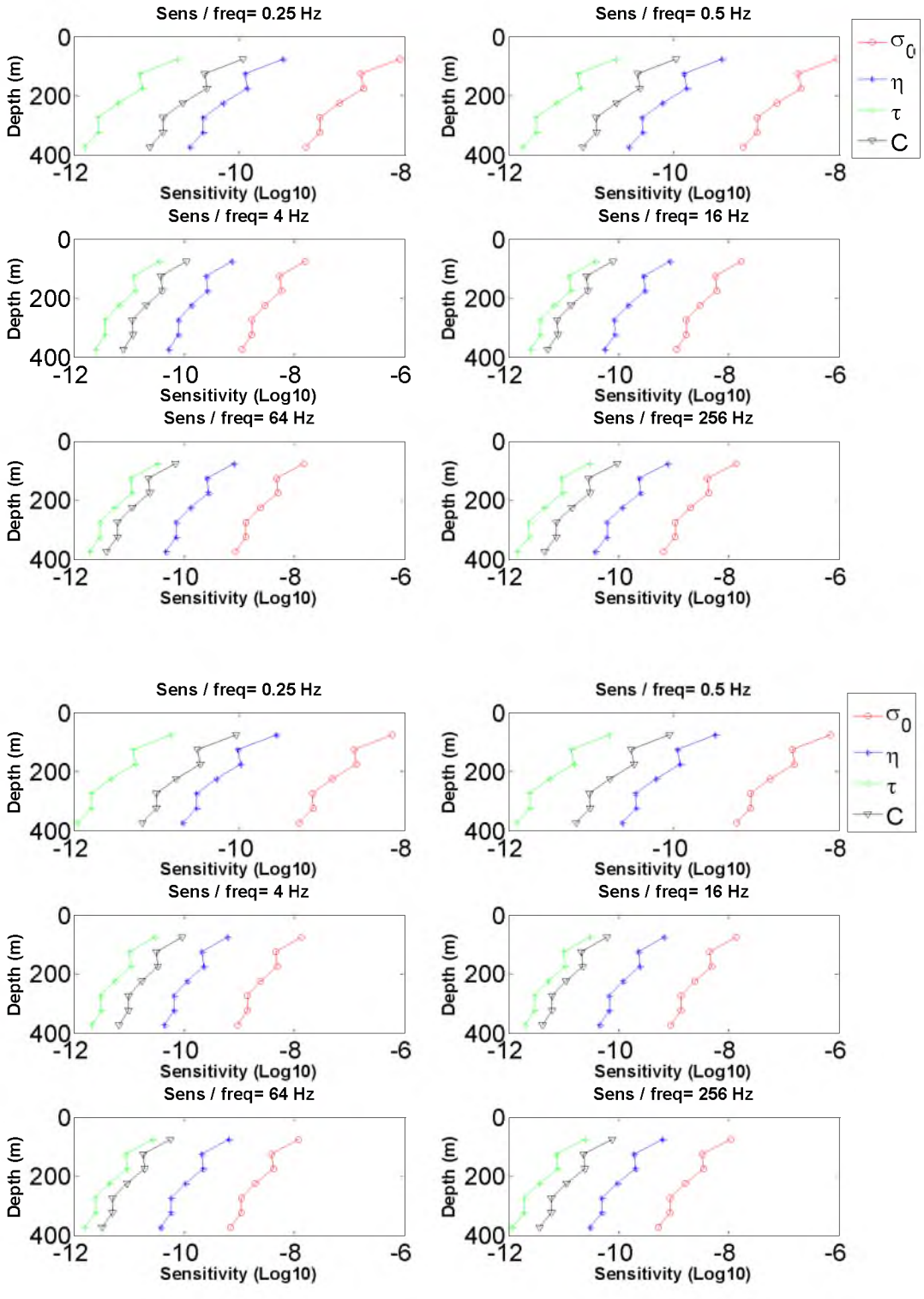

Figure 5.27 Model 3. Top panel: the first iteration non-weighted integrated sensitivity of σ_0, η, τ and C for the center column cells of resistive body. Bottom panel: conductive body based on six frequencies.

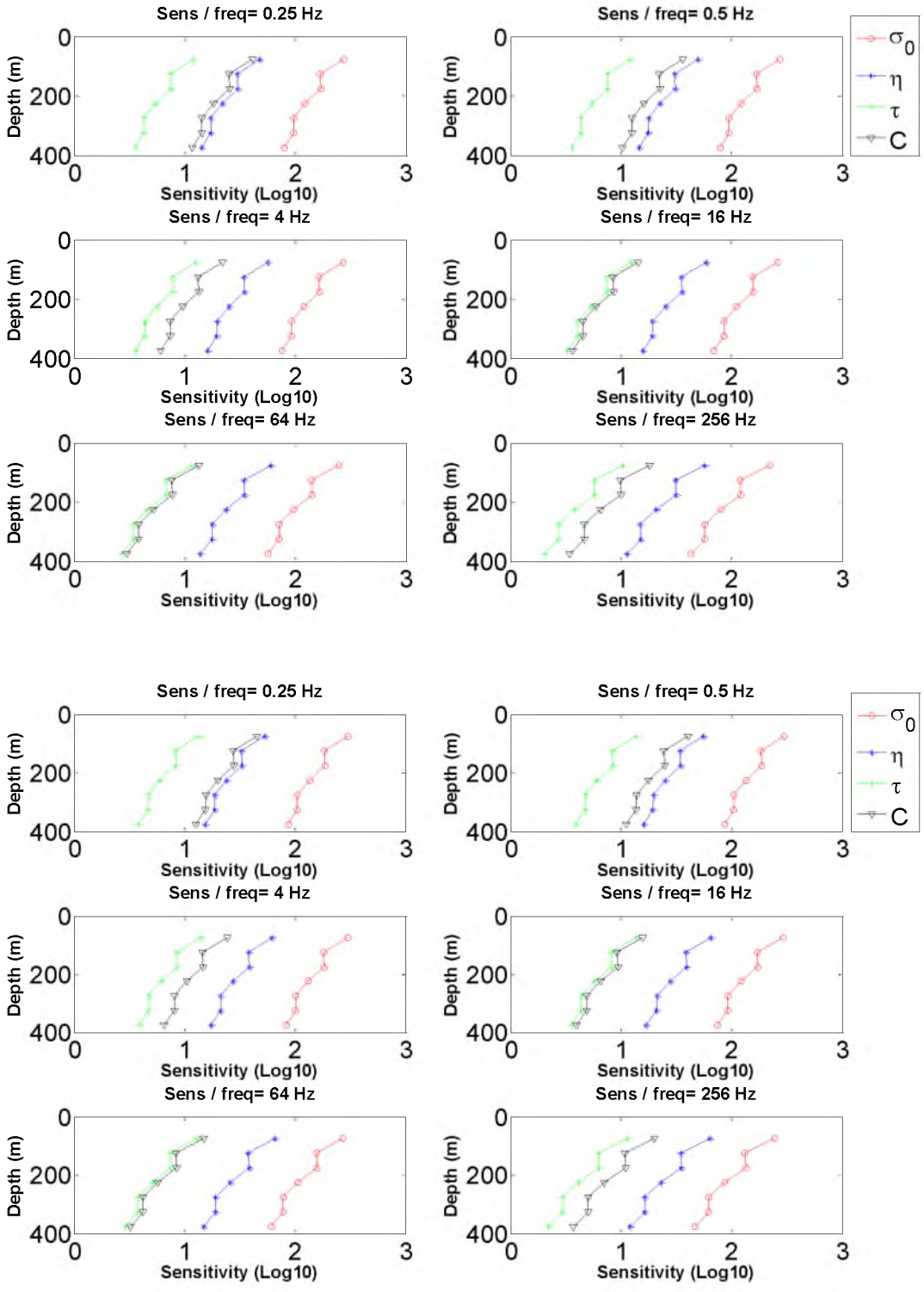

Figure 5.28 Model 3. Top panel: the first iteration weighted integrated sensitivity of σ_0, η, τ and C for the center column cells of resistive body. Bottom panel: conductive body based on six frequencies.

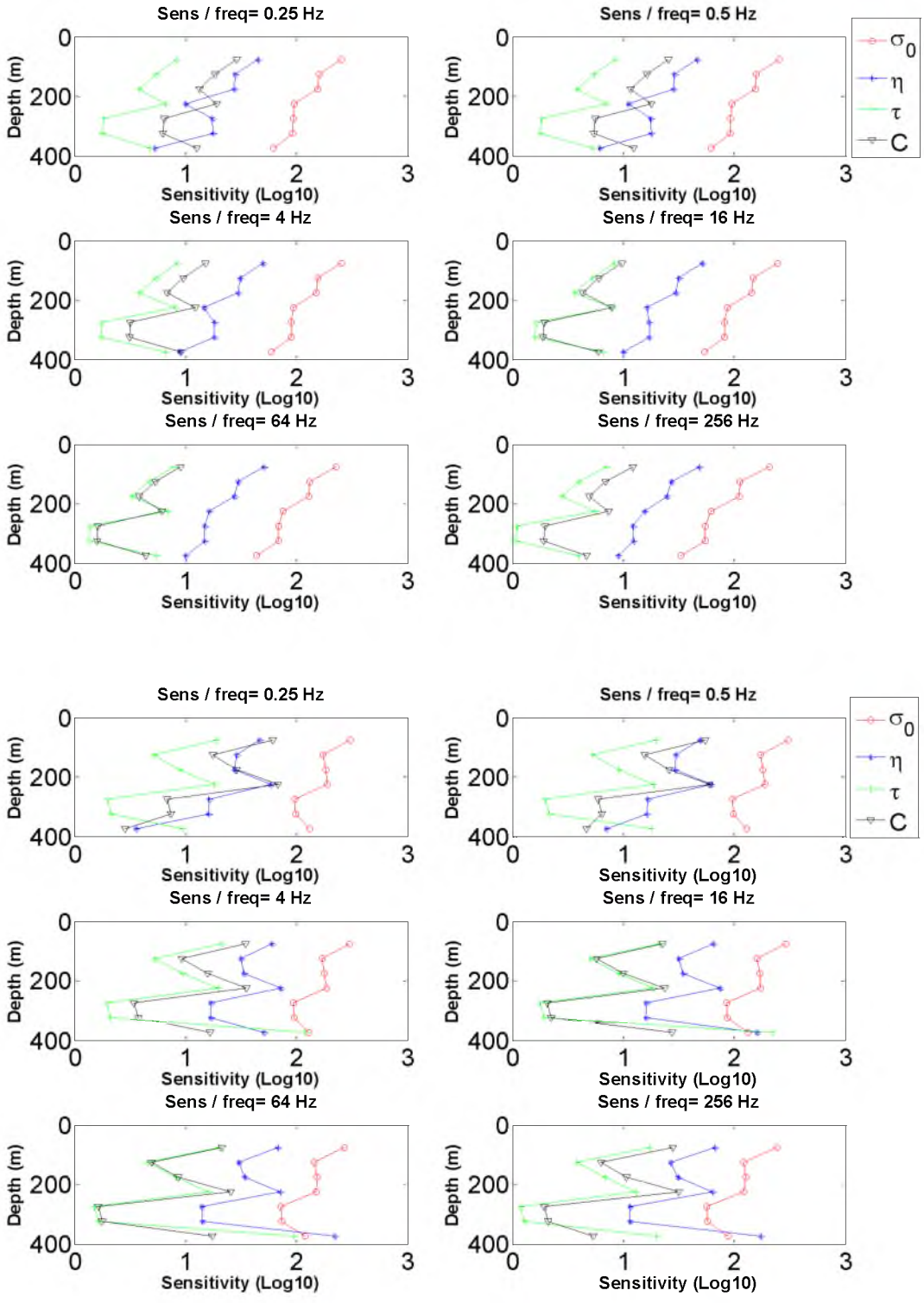

Figure 5.29 Model 3. Top panel: the last iteration weighted integrated sensitivity of σ_0, η, τ and C for the center column cells of resistive body. Bottom panel: conductive body based on six frequencies.

Fig 5.27 shows the nonweighted integrated sensitivity value of the resistive target of the first iteration, it shows that the order of the sensitivity of the four Cole-Cole parameters vary with the frequency. The value of sensitivity of σ_0 is about 30 times larger than that of chargeability (η), about 100 times larger than that of relaxation parameters (C), about 300 times larger than that of time constant (τ). After adding data weighting which is shown in Eq. 5.8, the value of sensitivity of each parameter shown in Fig 2.28 is much larger than before (Fig 5.27). This phenomenon demonstrates that the function of data weighting is not only the increasing the sensitivity value for all parameters simultaneously. It also can make inversion results much better and more stable.

Comparing with top and bottom panel in Fig 5.23, for example, for any specific frequency, the value of weighted integrated sensitivity of conductive target is relatively larger than that of resistive target, even at the first iteration. Let us move to the sensitivity at the last iteration (Fig 5.29), which shows that all the curves bend from left to right, especially the curves of chargeability (η), time parameter (τ), and relaxation parameters (C) bend much more than DC conductivity (σ_0). The depth range of serious curving part is from 150 m to 300 m which coincides with the true depth of both anomalies. In Fig 5.29, even from the last iteration, the value of τ is still relatively smaller than C, but the inversion result of τ is much better than C. One of reason is, if we look the sensitivity variation from 8Hz to 64 Hz in Fig 2.9, the curves of C can be considered as "constant" which means they vary very little as compared with that of τ. In another words, the sensitivity of τ is more sensitive than that of C for all frequency. So that is why in the Model 3, the conductive target can be recovered much better than the resistive one.

5.4.2 Sensitivity Analysis of Synthetic Model 4

Fig 5.21 to Fig 5.24 shows the result of the inversion for DC conductivity (σ_0), chargeability (η), time parameter (τ), and relaxation parameter (C) for synthetic Model 4. The inversion results of the resistive target based on σ_0, η, τ are much better than that in Model 3, especially for σ_0. In order to make the interpretation about the phenomena, I adopt the same sensitivity analysis described above. The value of Fréchet matrix of the 7 middle column cells of the resistive and conductive targets based on the first and last iteration (Fig 5.30) is picked up to use Eq. 5.8 to calculate corresponding weighted integrated sensitivity for six frequencies. Finally I plot them together shown in Fig 5.31 and Fig 5.32.

Figure 5.31 shows the weighted integrated sensitivity value of the resistive target at the first iteration. The average values of the nonweighted integrated sensitivity of the four Cole-Cole parameters varying with frequency are smaller than that in Model 3 and the ratio among them also increases. After adding data weighting, the same as sensitivity of Model 3, the value of sensitivity of each parameter increases much more large as well (Fig 5.31).

In Fig 5.31, for example, for any specific frequency, the value of sensitivity of conductive target is approximately the same as that of the resistive target, even at the first iteration. Let us move to the sensitivity at the last iteration (Fig 5.32), for resistive target, the curves of chargeability (η), time parameter (τ), and relaxation parameter (C) are bent toward the opposite direction of DC conductivity (σ_0). The curves of chargeability (η), time parameters (τ), and relaxation parameters (C) bend much more than DC conductivity (σ_0) and themselves are shown in Fig 5.32. The depth range of bent curves represents

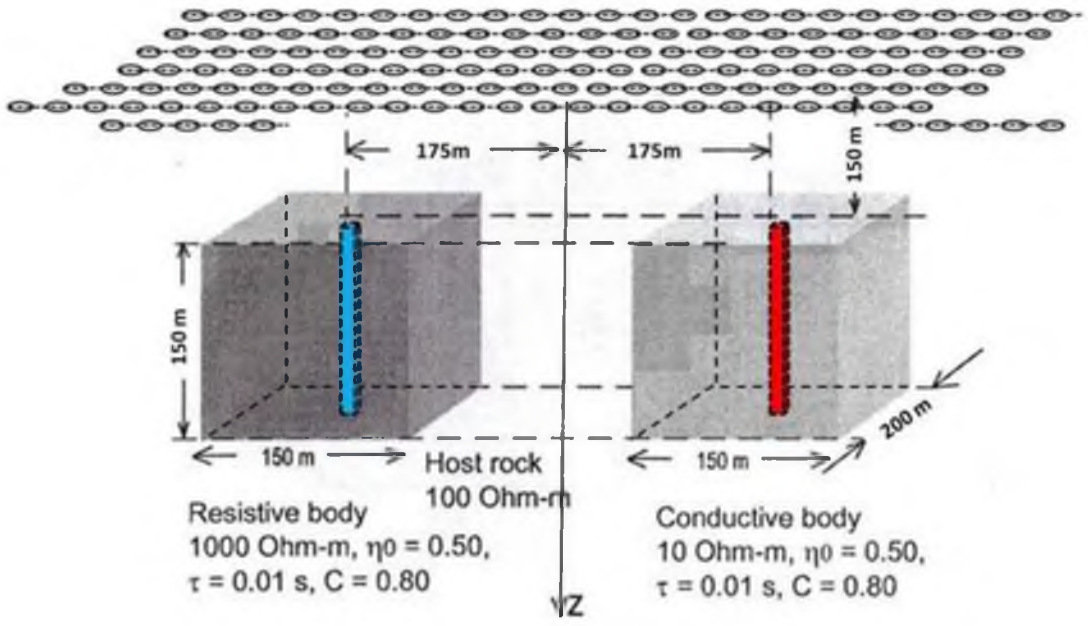

Figure 5.30 Sensitivity analysis based on synthetic Model 4. a) Center column cells (blue) of the resistive body. b) Center column cells (red) of the conductive body.

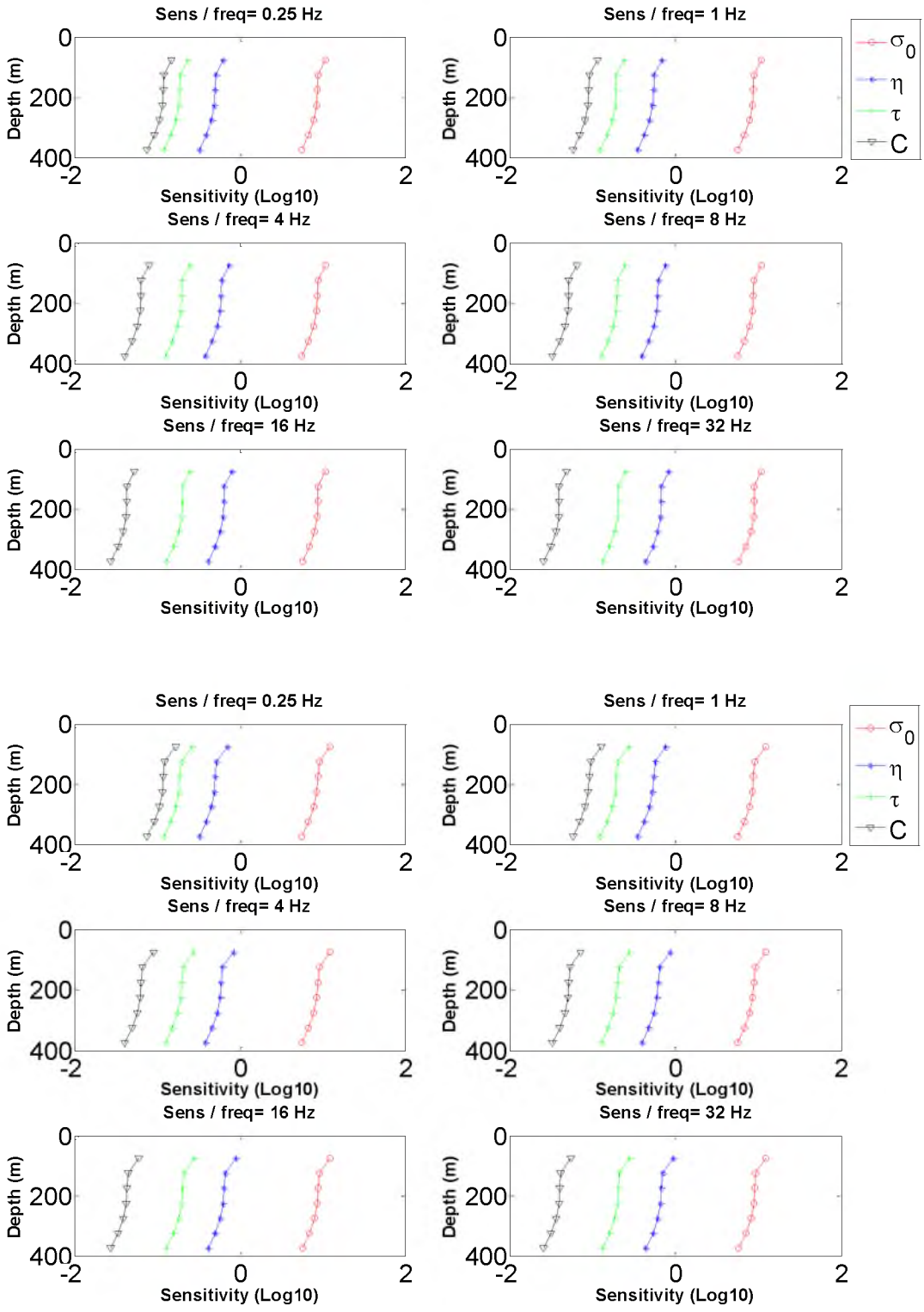

Figure 5.31 Model 4. Top panel: the first iteration weighted integrated sensitivity of σ_0, η, τ and C for the resistive body. Bottom panel: the conductive body based on six frequencies.

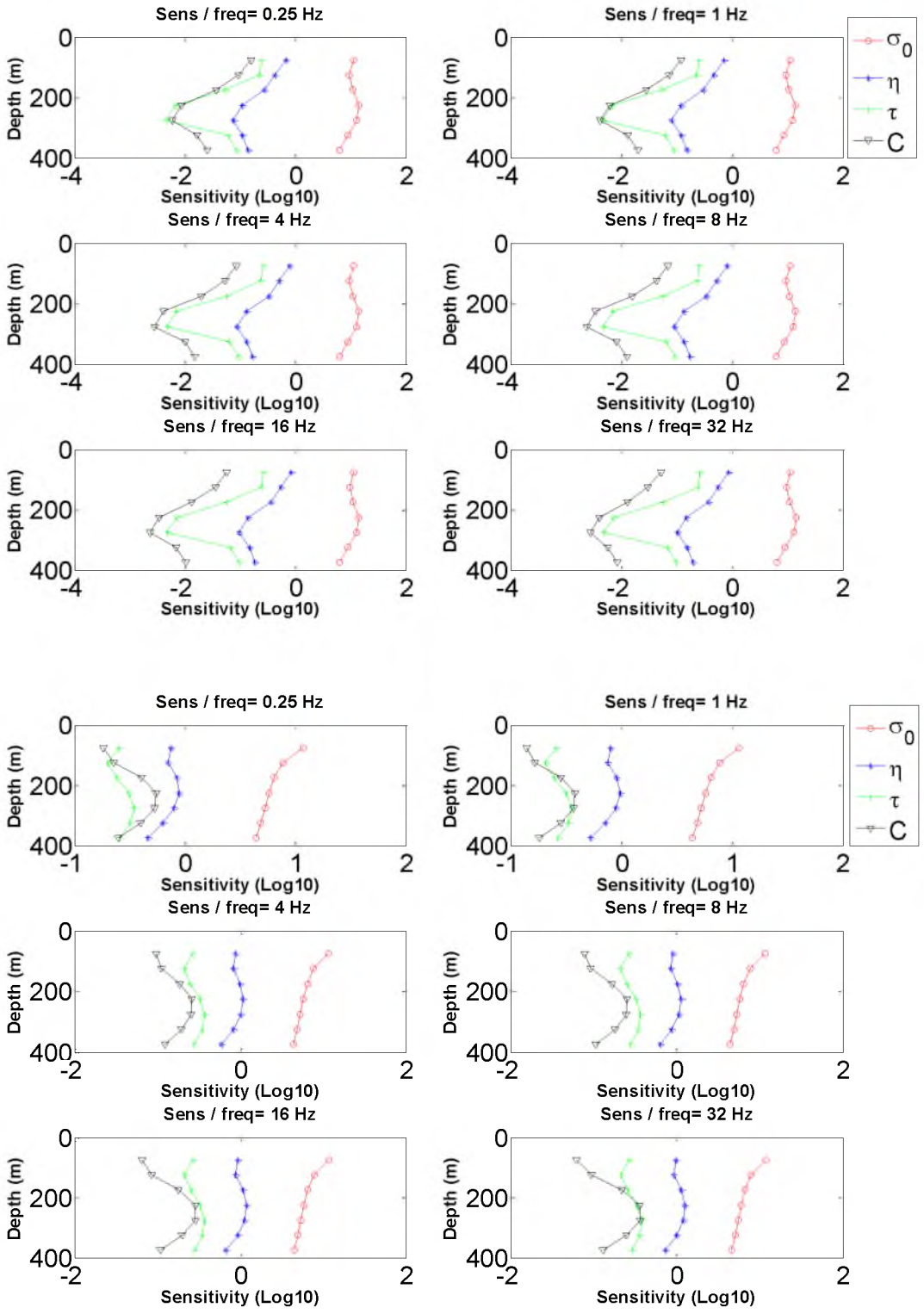

Figure 5.32 Model 4. Top panel: the last iteration weighted integrated sensitivity of σ_0, η, τ and C for the resistive body. Bottom panel: the conductive body based on six frequencies.

information about the anomaly. Since I set up 0 as initial value for chargeability (η), time parameter (τ), and relaxation parameter (C), the value of these three parameters tend to be negative during the inversion. The inversion will pull them back to the positive when it happens. That is why one sees the opposite direction against DC conductivity (σ_0). That is why it can recover resistive target in Model 4 better than that in Model 3.

On the other hand, for conductive target (Fig 5.32), curves of chargeability (η), time parameter (τ), and relaxation parameter (C) are bent toward the DC conductivity (σ_0). Unlike the case of Model 3, the value of τ is relatively larger than that of C. In other words, C has the weakest sensitivity among the four parameters. It may be one of reasons that why in the Model 4, the inversion result of C is not very good.

The depth range of largest curve part is about from 150 m to 300 m, which consists with the true depth of the resistive and conductive targets as well.

CHAPTER 6

INTERPRETATION OF IP DATA IN NORTH SILVER BELL

The Silver Bell district is within the porphyry-copper province of southwestern North America shown in Fig 6.1, located 35 miles northwest of Tucson, Arizona on the south side of the Silver Bell Mountains. Mineralization in the district consists of at least three distinct disseminated porphyry copper deposits and several skarn replacement deposits. Disseminated primary and supergene enriched porphyry copper mineralization were mined in two open pits, E1 Tiro and Oxide, by ASARCO, mainly between 1954 and 1977. Total production for that period is reported at 75.66 million tons (Mt) at 0.80% copper (Titley, 1982). The North Silver Bell deposit is located at the north end of the district and represents a leachable resource of in excess of 80 Mt at an average grade of 0.40% copper contained mostly within an enrichment blanket of chalcocite.

Geophysical surveys conducted over the deposit by Zonge Engineering and Research Organization (ZERO) included ground magnetics, dipole-dipole complex resistivity (CR), reconnaissance induced polarization (RIP), controlled source audio-frequency magnetotellurics (CSAMT) and transient electromagnetics (TEM and NanoTEM). Additional data include CR rock measurements on core specimens from drill

Figure 6.1 Location of major Porphyry Copper Deposits in Southwestern North America (adapted from Thoman et al., 1998).

holes within the deposit and airborne magnetic and EM data flown by World Geoscience in 1993. Except for the airborne data from World Geoscience, all data were processed at ZERO's office in Tucson, Arizona. TEM, IP and CSAMT data, which are not shown in this dissertation, were modeled with proprietor smooth-model inversions (Thoman et al., 1998).

6.1 Geology of North Silver Bell Area

Porphyry systems are important geologic targets for mineral exploration. Copper, gold, and molybdenum are among the important minerals extracted from these deposit. Circulating hydrothermal fluids help to concentrate economic minerals in the alteration

zones surrounding the intrusion. Further concentration of metals, principally copper, can occur from weathering forming the leached cap and enriched zone (Thoman et al., 1998).

Since the early Mesozoic, the continental margins flanking the eastern Pacific rim have been repeatedly deformed by tectonic forces acting at different rates and in different directions. The deformations have modified preexisting margins or have resulted in accretion or addition of rock to those margins which contain margins of South America, Canadian northwest and western United States. Early and sometimes continuous evolution of batholiths occurs on one side of a mobile belt, which is flanked on its other side by a craton or by an uplifted craton. Within the deformed or mobile belts, small porphyry concentrator plutons are widely emplaced. Since an earlier time in the mid Tertiary, the accreted arc of the southwestern Pacific became involved in the phenomenon of circum-Pacific deformation. Deposits of the eastern Pacific rim occur between a line of Mesozoic batholiths and either a Precambrian-lower Paleozoic craton edge or on the edge of a fragmented craton (Titley, 1982).

The porphyry copper deposits are related to volcanic processes and the intrusions represent subvolcanic pluton. Mesozoic and younger porphyry ore deposit occur in the strongly deformed, faulted, and uplifted region of the Pacific rim. Porphyry copper deposits are landward of Mesozoic batholiths of the west coast and are flanked on the northeast by uplifted Precambrian basement rock. The deposits of southeastern Arizona are in contact with middle Proterozoic metamorphic rock and younger Precambrian granitic rocks. The intrusion is in contact with a wall rock of various compositions that are formed by Precambrian metamorphic and intrusive rock, or Paleozoic craton and Mesozoic geosynclines or finally volcanic rocks. The wall rock will strongly control the

effect of the hydrothermal processes and influence flow of hydrothermal fluid (Oen, 1981). Large copper deposits are related to large intrusions or intrusive complexes. In some complexes, intrusions represent single, discrete magma bodies; in others, separate phases suggest the emplacement of one or two masses of magma. Mineralized plutons must be fractured, allowing hydrothermal fluids to alter the rock and deposit sulfide minerals. Magma pressures during the early stages of cooling are a significant mechanism in the development of fractures within the bodies. Fractures result from crystallization of water-saturated melts, which give rise to the high pressures required to fracture the pluton. The evolutionary path of the hydrothermal process, which is dominated by cooling, results in precipitation and zoning of both alteration products and metals. Zoning is centered either on intrusions, especially small ones, or on intrusion contacts with wall rock. Hypogene alteration in the porphyry copper deposits of south-western North Ameica shows that different mineral assemblages were present within individual deposits. Skinner describes the hydrothermal mineral assemblages observed in many porphyry copper deposits of the region (Skinner, 1981).

Some key requirements for the formation of most ores include a source for the metals, a mechanism for transporting the metals, and a mechanism for precipitating the ore minerals. For example, as a hot igneous magma intrudes into the rock already present, it encounters underground water derived from rainfall. The magma heats this water, and the water begins to move in large circular paths. As the water moves downward, it becomes hotter and leaches copper and other metals from the different rocks it encounters. As the metal-rich water moves back upward, it cools and changes its chemistry, so that chalcopyrite and other ore minerals are precipitated at the margin of

the intrusion. In this model, the immediate sources of the metals are the rocks surrounding the igneous magma, the circulating groundwater is the transporting mechanism, and the cooling and changing composition of the groundwater is the precipitation mechanism. In addition to forming ore deposits, this circulating water can form large bodies of altered rocks surrounding the stocks known as alteration zones.

Lowell and Guilbert (1970) compared their findings with 27 other porphyry copper deposits and developed the Lowell-Guilber model . In this fundamental work they demonstrated that the best reference framework to which we can relate all the other features of these deposits is the alteration zoning. They postulated that four alteration zones are present, as shown in Fig 6.2. The potassic zone, which is not always exposed, is characterized by the development of secondary orthoclase and hydrothermal biotite or by orthoclase-chlorite and sometimes orthoclase-biotite-chlorite. Anhydrite may be prominent in this zone. There is commonly a low grade core to this zone in which chlorite and sericite are prominent (Fig 6.2). The phyllic zone is characterized by the assemblage quartz-sericite-pyrite and usually carries minor chlorite, illite and rutile. It possesses the greatest development of disseminated and veinlet pyrite. The contact with the potassic zone is gradational over tens of meters. The argillic zone, which is not always present, is characterized by clay minerals with kaolinite being dominant nearer the orebody. Pyrite is common, but less abundant than in the phyllic zone. It usually occurs in veinlets rather than as disseminations. The propylitic zone, which is never absent, is characterized by chlorite, calcite and epidote. This zone fades into the surrounding rocks over several hundreds of meters.

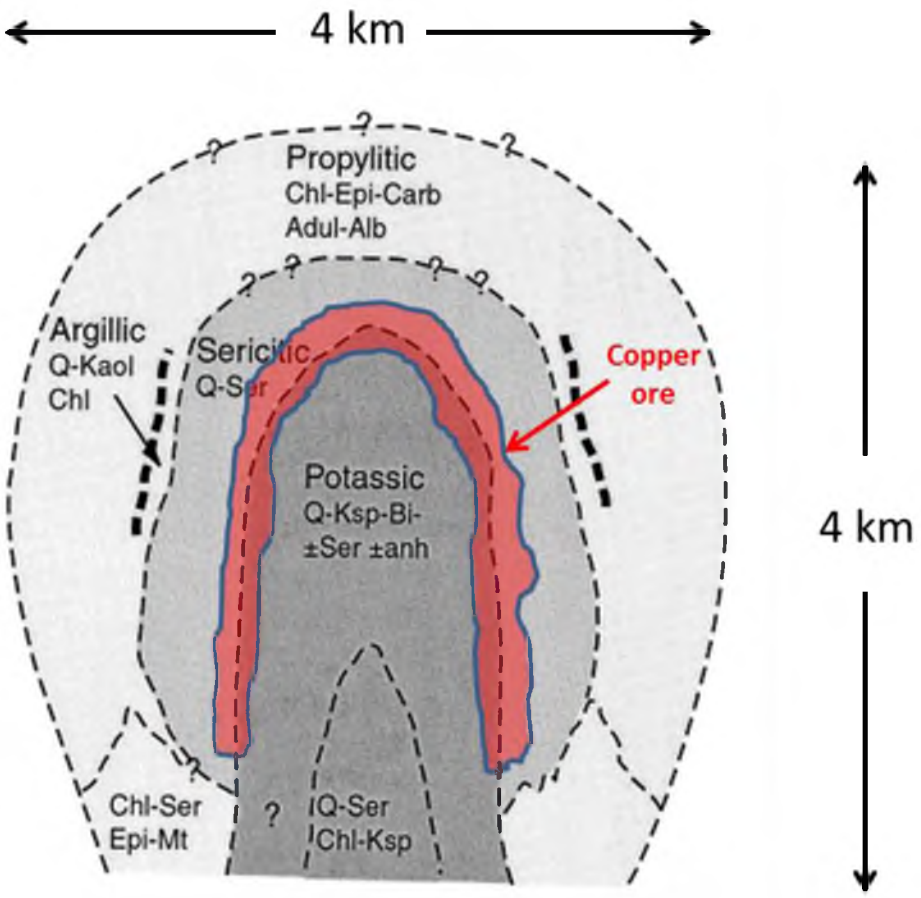

Figure 6.2 Schematic drawing of alteration zoning in typical porphyry copper deposit (adapted from Guilbert and Lowell, 1974).

Both Lowell and Guilbert (1970) and Rose (1970) have established a geometric relationship among the various alteration type in which potassic alteration is centrally located and the phyllic, argillic, and propylitic assemblages are circumferentially arranged at increasingly greater lateral distances from the potassic core. The spatial relationship among alteration types is sufficiently systematic and recurrent to warrant definition as typical alteration zoning for Arizona-type porphyry copper deposits. This spatial arrangement has been widely accepted for use in exploration since presentation of the model (Titley, 1982).

Regionally, the Silver Bell district is along the major northwest-trending the Silver Bell-Bisbee discontinuity. In the Silver Bell district, Richard and Courtright (1966) inferred a major west-northwest fault or series of faults that partially controlled the emplacement of the porphyry suites with their attendant mineralization and alteration. This west-northwest trending zone of alteration and mineralization extends from the Oxide pit on the east to the El Tiro pit on the west shown in Fig 6.3. At the El Tiro area, the trend of mineralization and alteration changes from a north-northwest to north orientation. This change in orientation reflects the presence of two or more major northwest to north-northwest faults that controlled the intrusion of the porphyry suite.

The N40°W El Tiro fault is interpreted as the original contact between the Mesozoic clastic units to the southwest and the Paleozoic units to the northeast. This major structure may have controlled the emplacement of the alaskite, the dacite porphyry and some of the quartz monzonite stocks with their mineralization and alteration shown in Fig 6.4 (Thoman et al., 1998).

A second structure oriented N5°W may be a splay off of the El Tiro fault. This

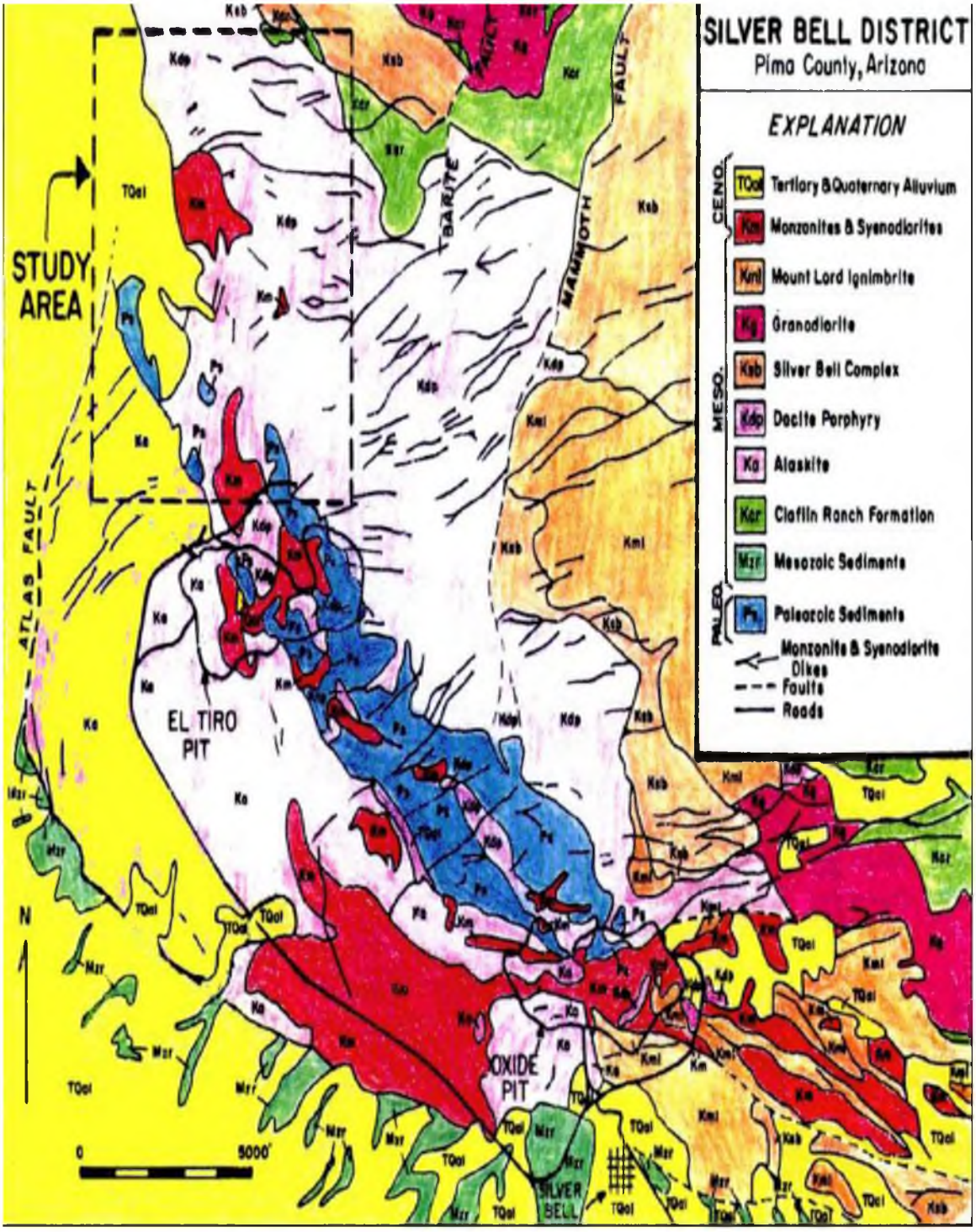

Figure 6.3 General geologic map of the Silver Bell area (adapted from Kranbegs ,1980).

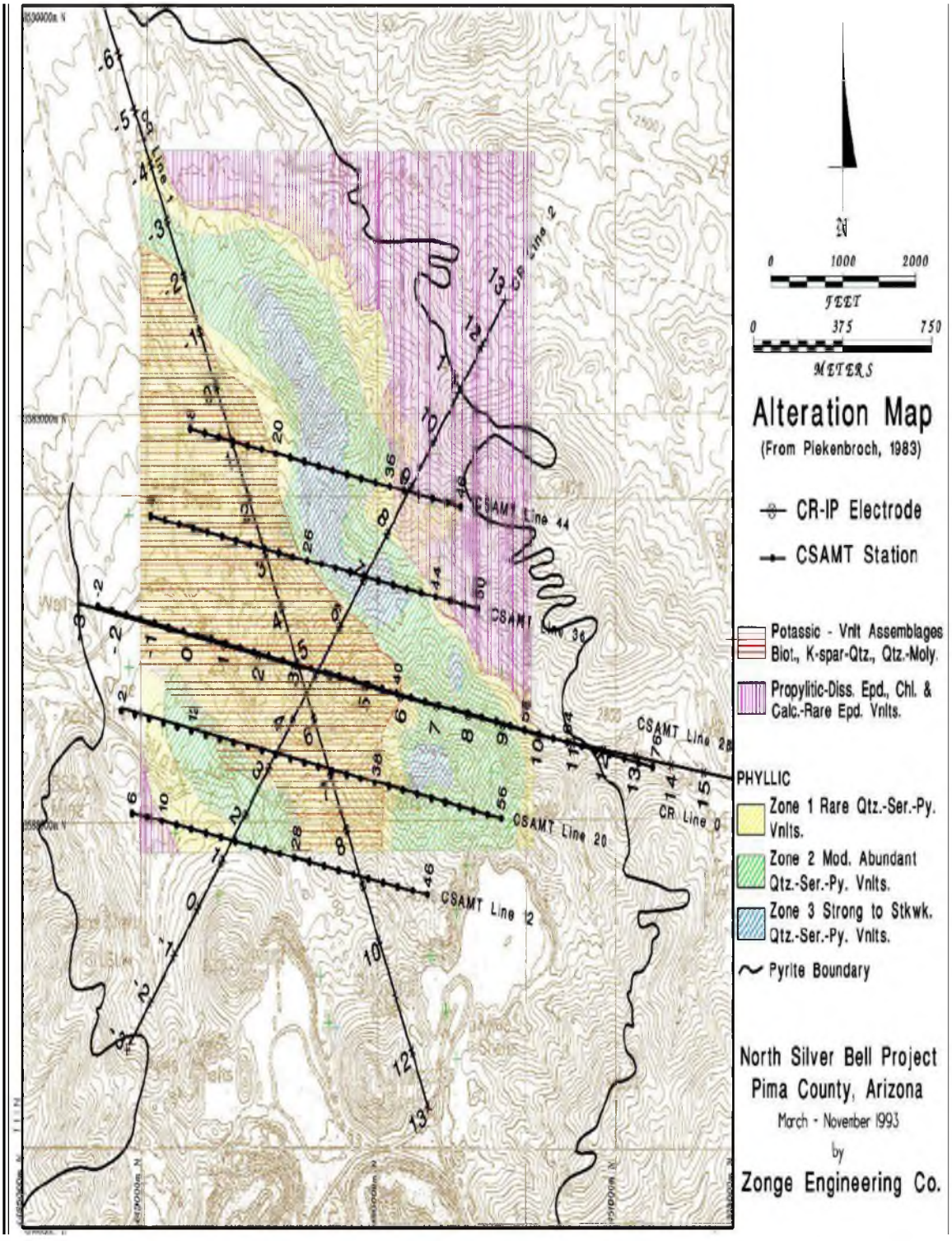

Figure 6.4 Detail geologic map of alteration zone in Silver Bell area (adapted from Thoman et al., 1998).

interpreted fault parallels the elongation of the Daisy and El Tiro stocks as well as the alignment of these two stocks and the North Silver Bell stock. To the west of this inferred fault is the north-northeast to north-northwest striking postmineral Altas Fault. This structure brings Gila Conglomerate to the west in contact with older units to the east (Thoman et al., 1998).

Numerous northeast to east-northeast to west-northwest monzonite porphyry dikes are mapped in the district, principally to the east and northeast of the El Tiro and North Silver Bell area. It is interpreted that these dikes intruded premineral structural elements that intersect the northwest El Tiro fault at the present location of the El Tiro pit. This structural intersection is interpreted by some to have localized the porphyry mineralization in that locality. Another suggested interpretation (Heidrick, 1974) is that the northeast orientations reflect hydraulic fracturing during emplacement of water-saturated magmas.

Orientations of mineralized fractures changes from dominantly north-northeast at the Oxide pit to east-northeast at the El Tiro pit. According to Grabeal (1982), mineralization is both disseminated and along fractures. Fractures host most of the mineralization away from the potassic zone and phyllic zone which is shown in Fig 6.4 (Thoman et al., 1998).

6.2 Description of the IP Data

The general IP response obtained over North Silver Bell is similar in magnitude and character to that obtained over other exposed or shallowly buried porphyry systems elsewhere. The results of the IP survey illustrate the utility of this technique in exploring

a large area for a possible porphyry system. A reconnaissance survey was conducted in the North Silver Bell area to assess the utility of this technique in defining a porphyry system within a districtwide context and how the actual response correlates with that obtained from dipole-dipole measurements.

One IP Line 0 shown in bottom panel of Fig 6.5 was surveyed at North Silver Bell using a dipole spacing of 500 ft. It served as the central line for the CSAMT and magnetic surveys. This orientation was chosen to minimize the extremes of the crossed topography and to be perpendicular to an inferred major fault. The data for Line 28 were acquired with a Zonge GDP-16 three-channel receiver in a reference complex-resistivity mode using 15 harmonic frequencies from 0.125 Hz to 72 Hz generated by three main frequencies of the current in the transmitters.

I used Eq. 2.8 and Eq. 2.9 to convert the apparent resistivity and IP phase to the real and imaginary parts of the electric field, which served as the input data for the inversion. The CR data were inverted for a 3D conductivity model with 4669 cells of size, 100 m × 300 m × 50 m. The inversion domain varied from −100 m to 2800 m along the survey line, from −1050 m to 1050 m across the survey line and from 50 m to 1200 m in the vertical direction. The initial and a priori models for 3D inversion with respect to each parameters, ρ_0, η, τ, and C were selected as follows:

$$\sigma_{init} = \sigma_{apr} = \frac{1}{500} S/m; \quad \eta_{init} = 0.01, \eta_{apr} = 0;$$

$$\tau_{init} = 0.01, \tau_{apr} = 0; \qquad C_{init} = 0.1, C_{apr} = 0;$$

The 3D inversion for the CR data converged to a final misfit of 10% from an initial misfit of 100%, without considering topography during inversion. The 3D

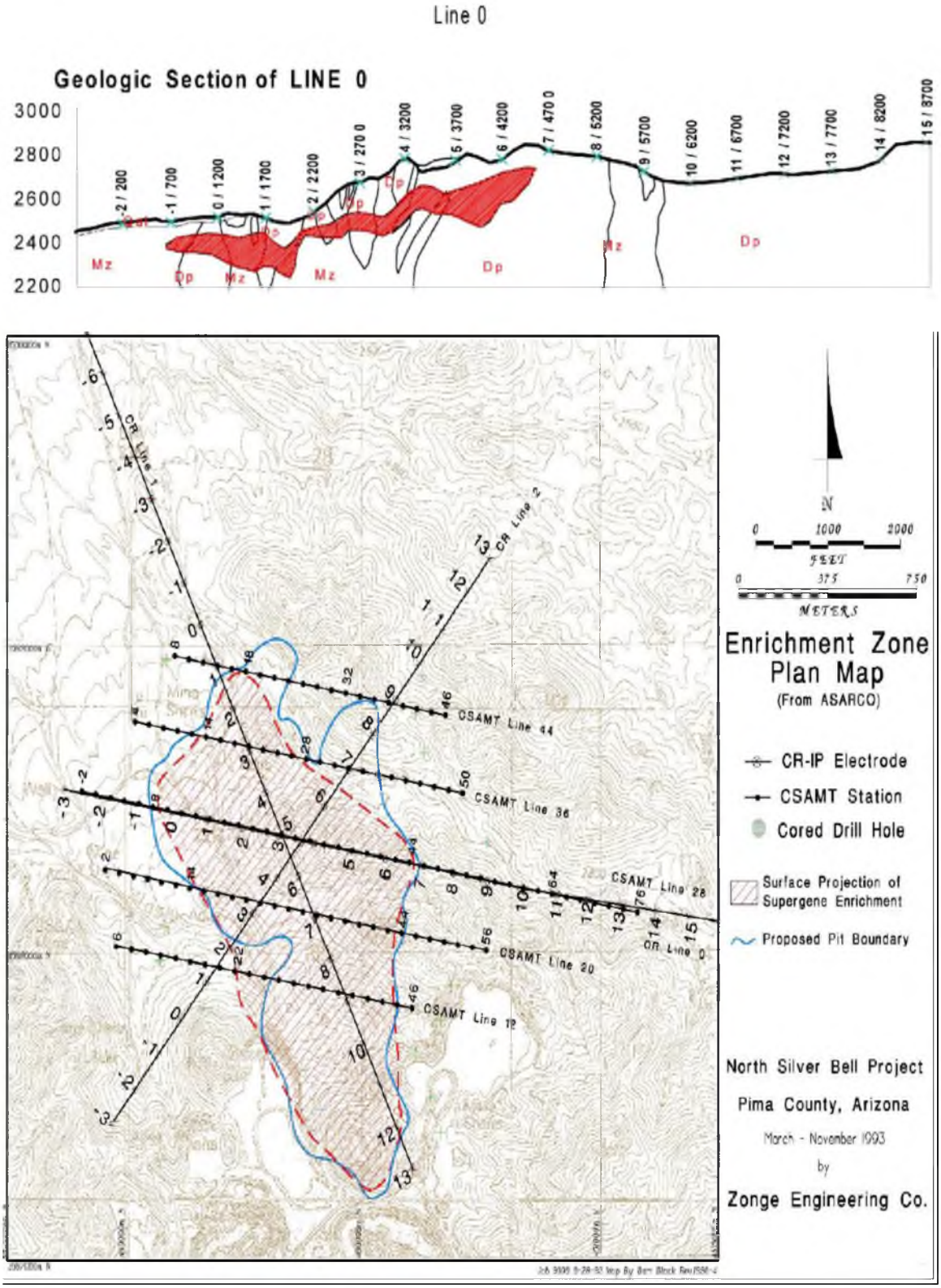

Figure 6.5 Top panel: Geological section along IP survey Line 0. Bottom panel: Plan map of the enrichment zone and the IP survey Line 0.

inversion of CR data was applied by parallel computation on a local Linux workstation using eight 2.5 GHz processors and 32 GB RAM, and it required 20 hours to complete.

6.3 Result of 3D Inversion of IP Data

The y component of the real and imaginary part of electrical field converted from the resistivity and phase data were modeled using 3D smooth-model inversion program. The predicted data in pseudo-section format are obtained from the 3D smooth-model inversions and allow a comparison with the observed data to determine the fit of the model. The smooth models permit assigning approximate depths to sources of anomalous response.

Because there is only one survey Line 0 of the CR data, I show only a vertical cross section of the 3D model beneath the survey line with respect to each parameter σ_0, η, τ, and C (Fig 6.6). Comparison with the smooth resistivity result by Zonge (Fig 6.7), shows that the parameter σ_0 matches resistivity quite well. The CR inversion results correlates well with the known geology section of the CR survey as shown in top panel of Fig 6.5. From the inversion results for σ_0, η, τ, and C, it shows that, the corresponding lateral conductive body is corresponding with the phyllic alteration zone within which it contains abundant pyrite and chalcopyrite. However, in the inversion result for C, it seems that the anomalous body of C is much deeper than those of other three parameters, but it is still in the area of the target. Note that we observed a similar result for the synthetic models. The main reason is that the sensitivity of C is the weakest among the four Cole-Cole parameters.

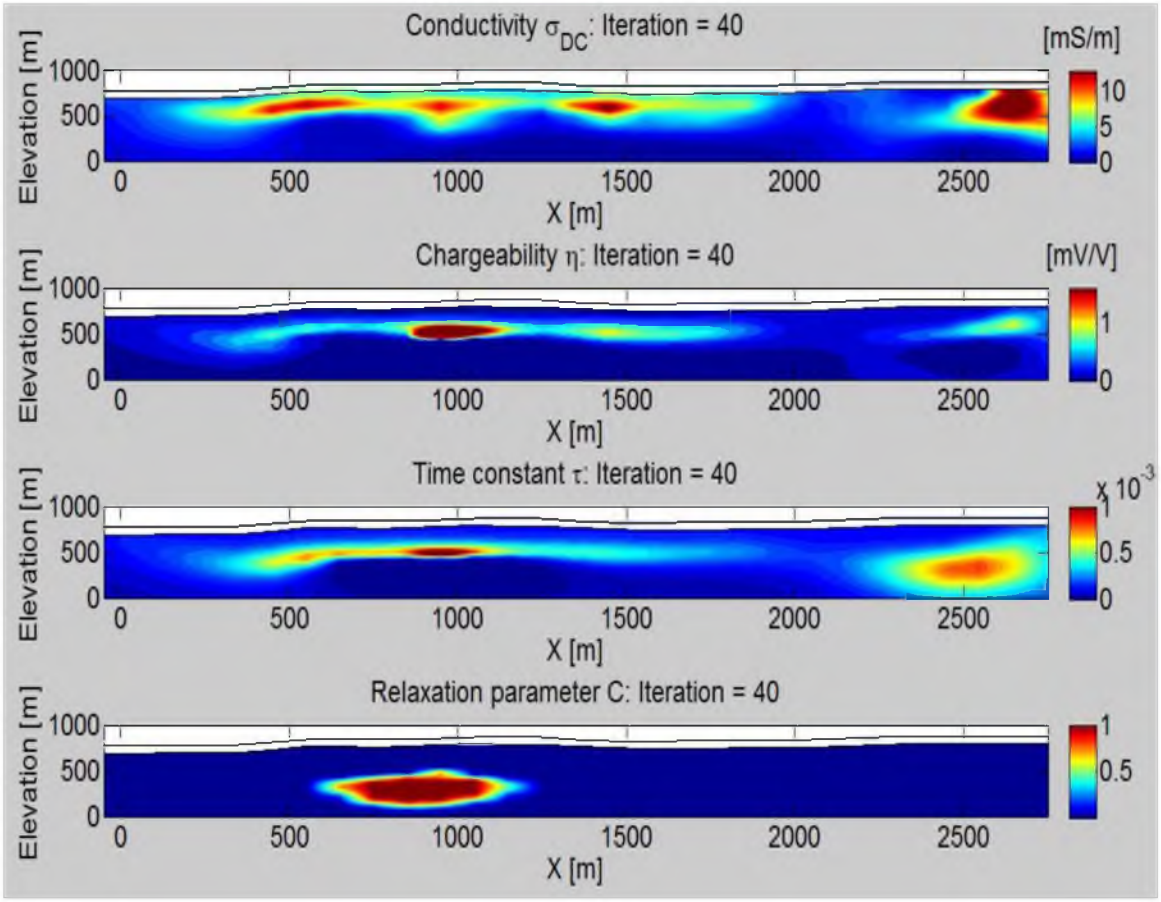

Figure 6.6 Vertical sections of 3D inversion results beneath the IP survey Line 0 with respect to each Cole-Cole model parameters, σ_0, η, τ, and C without considering topography. Note that meters were converted to feet for easier comparison.

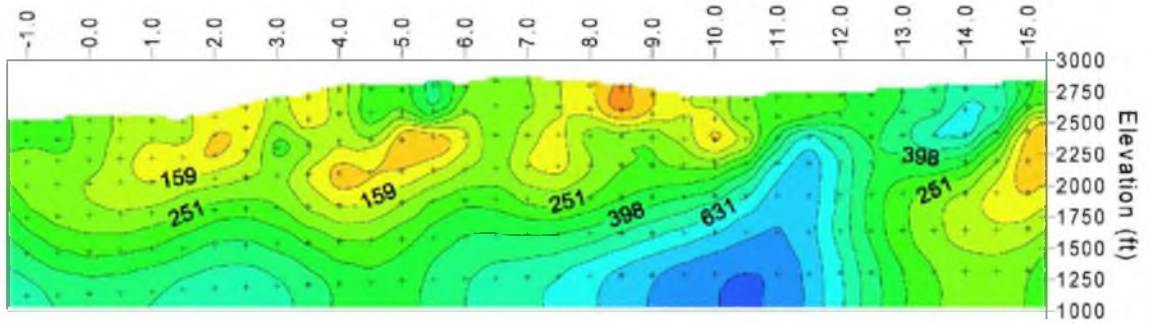

Figure 6.7 The smooth resistivity inversion beneath the IP survey Line 0 by Zonge (adapted from Thoman et al., 1998).

Except disseminated anomalies shown at a relatively shallow depth, there are no apparent anomalies in the background, because induced polarization provides a means of directly detecting disseminated sulfides, which do not appreciably affect the relatively higher resistivity of the host rock.

Fig 6.8 and Fig 6.9 show the examples of the observed and predicted apparent resistivity and IP phase for the North Silver Bell CR survey. We notice reasonable similarity between the observed and predicted apparent resistivity for all the frequencies. The observed and predicted IP phases do not fit very well. However, the fitting improves for the high frequencies in comparison with the low frequencies because the real mineral deposit is located very close to the surface, so the high frequencies are more sensitive to the deposit. The second reason is that I use real and imaginary part of electrical field converted by observed resistivity and phase as observed data to match during the inversion instead of resistivity and phases themselves. In other worlds, the inversion was supposed to match the apparent resistivity and phase instead of electric field. After inversion, the final predicted real and imaginary part of electrical field data were converted back to the apparent resistivity and phase using Eq. 2.8 and Eq. 2.9. Finally,

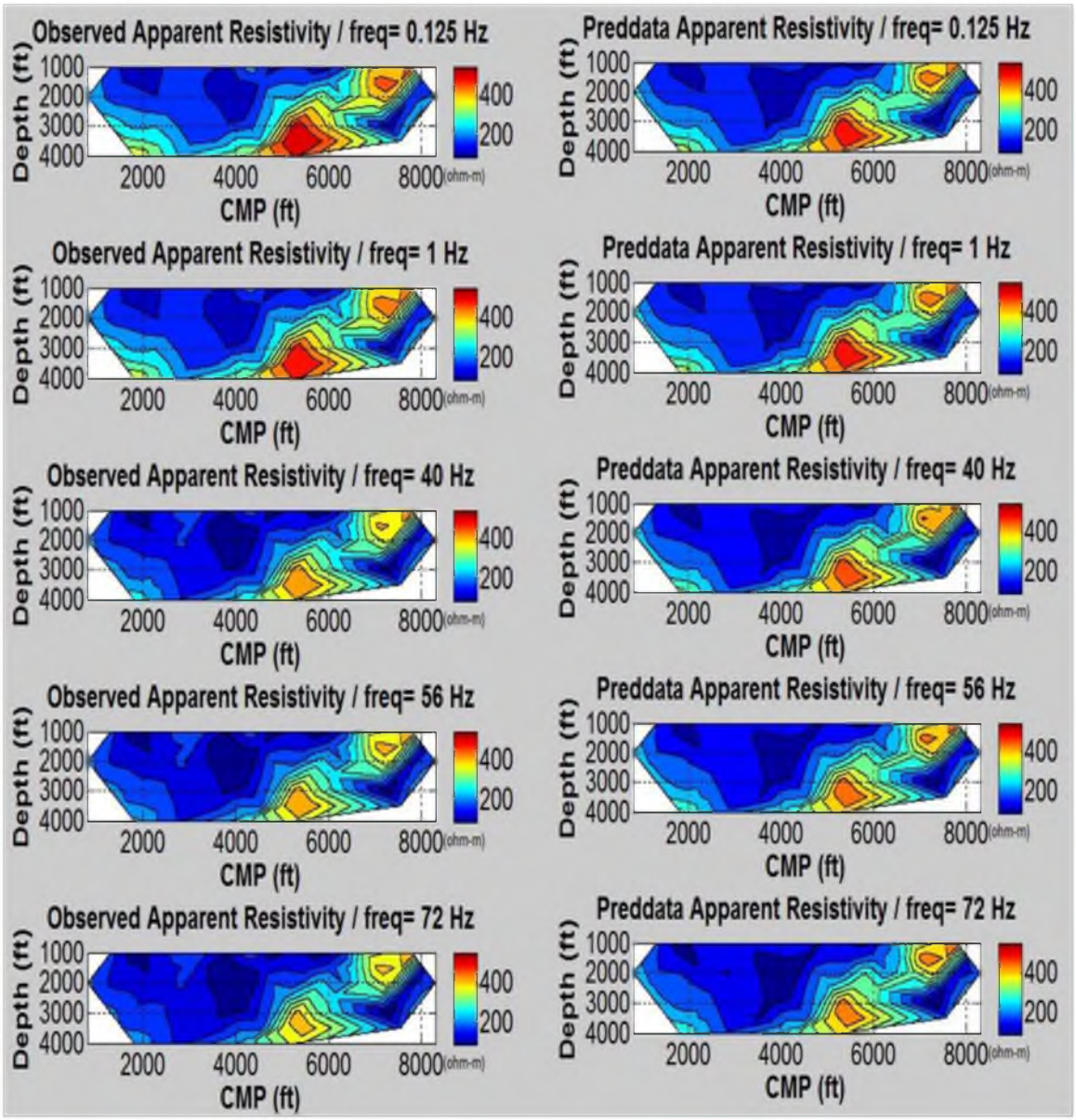

Figure 6.8 The observed (left column) and predicted (right column) apparent resistivity for the IP inverse model at different frequencies of 0.125, 1, 40, 56 and 72 Hz. Note that meters were converted to feet for easier comparison.

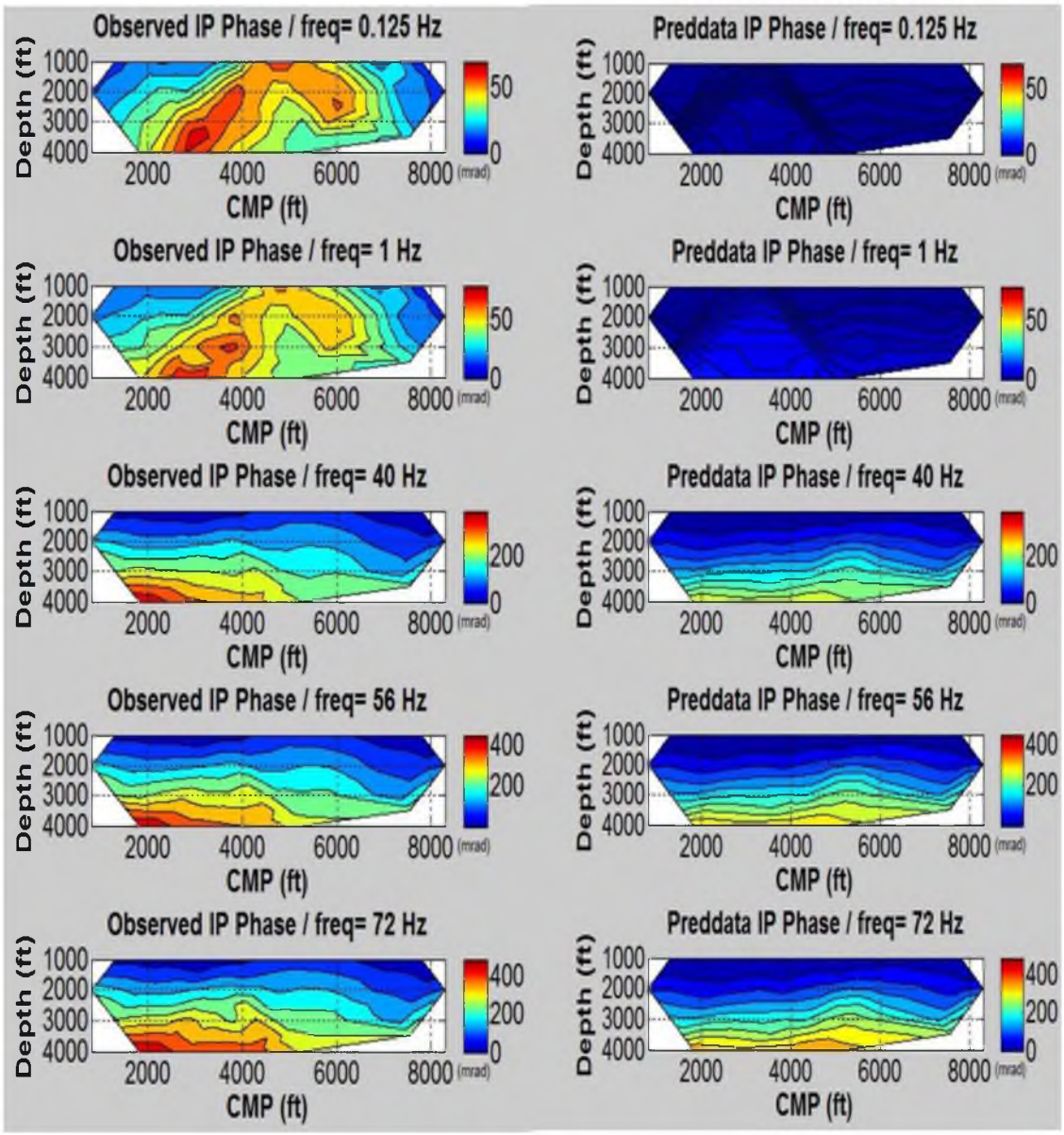

Figure 6.9 The observed (left column) and predicted (right column) IP phase for the IP inverse model at different frequencies of 0.125, 1, 40, 56 and 72 Hz. Note that meters were converted to feet for easier comparison.

according to Fig 6.8, too much noise maybe the cause that there is nothing shown in the predicted phase data especially for low frequencies.

The lowest resistivity on the line 0 can be approximately correlated with the quartz monzonite porphyry or areas of mixed quartz monzonite porphyry and dacite porphyry (Thoman et al., 1998). Some of the highest IP responses, particularly ones with a shallow component, can also be correlated with the phyllic alteration zones shown bottom panel in Fig 6.4. One would not expect very high IP responses in the potassic core zones containing primary mineralization of chalcopyrite and pyrite, as estimated total sulfides in this zone are only 2% by volume at most. Phyllic zones, however, can contain 5-7% by volume total sulfides.

From the geology section of Line 0 (Top panel of Fig 6.5), the depth of enrichment zone is about 200 ft. If we go back to the inversion results, especially for conductivity σ_0, the depth of the copper deposits is approximately about 500 ft, some positions up to 1000 ft (Fig 6.6 and Fig 6.7). The reason why the depth of targets in geology section is much more thin and clear than that in my inversion is the enrichment zone is confirmed based on some criterion by couple of wells. But I would speculate that the inversion results are worthy trust since pyrite and chalcopyrite which is below the enrichment zone can also cause the IP effect. So there should be a sort of transition zone that is corresponding to the inversion results.

CHAPTER 7

CONCLUSIONS

In this dissertation, I have developed a method for 3D simultaneous inversion of the four parameters of the Cole-Cole model, σ_0, η, τ, and C, from the surface IP data. The new method takes into account the nonlinearity of electromagnetic induction (EMI) and induced polarization (IP) and determines the Cole-Cole model parameters using the regularized reweighted conjugate gradient (RRCG) method. Three-dimensional modeling is based on the integral equation method. I have developed a computer code for parallel computation, which allocates various frequencies to multiprocessors on a local Linux workstation, which speeds up the computation and makes the code suitable for practical IP survey data interpretation.

With a synthetic model, I have shown the ability of the inversion method to accurately recover 3D distribution of the four Cole-Cole parameters σ_0, η, τ, and C. The model studies show that the inversion results for multisource data are generally better than those obtained for a fixed electrical dipole source. Based on the research about sensitivity related to the two surveys, in general, weighted integrated sensitivity is much larger than nonweighted sensitivity. During the inversion, the curves of the Cole-Cole parameters are bent toward the same direction that contains the "anomaly" information.

The method was applied to the practical 3D IP survey data from the North Silver Bell, located 35 miles northwest of Tucson, Arizona on the south side of the Silver Bell Mountains, and the results provided geo-electrical models that agree well with the published geology of the area. Thus, I demonstrates that the four parameters of the Cole-Cole model, DC electrical resistivity, ρ_0, (or electrical conductivity $\sigma_0 = 1/\rho_0$), chargeability, η, time constant, τ, and the relaxation parameter, C, can be recovered from the observed IP data simultaneously.

REFERENCES

Bleil, D. F., 1953, Induced polarization; a method of geophysical prospecting: Geophysics, v. 18, no. 3, p. 636-661.

Burtman, V., Endo, M., and Zhdanov, M. S., High-frequency induced polarization measurements of hydrocarbon-bearing rock, *in* Proceedings Consortium for Electromagnetic Modeling and Inversion Proceedings of 2003 Annual Meeting 2011, p. 3-26.

Carlson, N., Zonge, K., and MacInnes, S., 1994, Induced polarization effects in CSAMT data: Presented at the 100th Annual Mtg: Northwest Mining Assoc.

Chen, J., Kemna, A., and Hubbard, S. S., 2008, A comparison between Gauss-Newton and Markov-chain Monte Carlo–based methods for inverting spectral induced-polarization data for Cole-Cole parameters: Geophysics, v. 73, no. 6, p. F247-F259.

Cole, K. S., and Cole, R. H., 1941, Dispersion and absorption in dielectrics I. Alternating current characteristics: The Journal of Chemical Physics, v. 9, p. 341.

Commer, M., Newman, G. A., Williams, K. H., and Hubbard, S. S., 2011, 3D induced-polarization data inversion for complex resistivity: Geophysics, v. 76, no. 3, p. F157-F171.

Dey, A., and Morrison, H., 1979, Resistivity modeling for arbitrarily shaped three-dimensional structures: Geophysics, v. 44, no. 4, p. 753-780.

Fiandaca, G., Auken, E., Christiansen, A. V., and Gazoty, A., 2012, Time-domain-induced polarization: Full-decay forward modeling and 1D laterally constrained inversion of Cole-Cole parameters: Geophysics, v. 77, no. 3, p. E213-E225.

Hohmann, G., and Newman, G., 1990, Transient electromagnetic responses of surficial, polarizable patches: Geophysics, v. 55, no. 8, p. 1098-1100.

Hohmann, G. W., 1975, Three-dimensional induced polarization and electromagnetic modeling: Geophysics, v. 40, no. 2, p. 309-324.

Hursán, G., and Zhdanov, M. S., 2002, Contraction integral equation method in three-dimensional electromagnetic modeling: Radio Science, v. 37, no. 6, p. 1089.

Li, Y., and Oldenburg, D. W., 2000, 3-D inversion of induced polarization data: Geophysics, v. 65, no. 6, p. 1931-1945.

Morrison, H., and Gasperikova, E. F., Mapping of induced polarization using natural fields, *in* Proceedings 1996 SEG Annual Meeting 1996.

Oen, I. S., 1981, An introduction to ore geology: Earth-Science Reviews, v. 17, no. 3, p. 112-129.

Oldenburg, D. W., 1997, Computation of Cole-Cole parameters from IP data: Geophysics, v. 62, no. 2, p. 436-448.

Olhoeft, G., 1985, Low-frequency electrical properties: Geophysics, v. 50, no. 12, p. 2492-2503.

Pelton, W. H., 1977, Interpretation of induced polarization and resistivity data: Ph.D dissertation, University of Utah.

Phillips, C. R., 2010, Experimental study of the induced polarization effect using Cole-Cole and GEMTIP models: Master's thesis, University of Utah.

Rowston, P., Busuttil, S., and McNeill, G., 2003, Cole-Cole inversion of telluric cancelled IP data: ASEG Extended Abstracts, v. 2003, no. 2, p. 1-4.

Siegel, M., and King, R. W., 1970, Electromagnetic fields in a dissipative half-Space: a numerical approach: Journal of Applied Physics, v. 41, no. 6, p. 2415-2423.

Skinner, B. J., 1981, Economic geology, seventy-fifth anniversary volume, 1905-1980, Economic Geology Publishing Company, El Paso, Texas.

Sumner, J. S., 1976, Principles of induced polarization for geophysical exploration, Elsevier.

Telford, W. M., Geldart, L. P., and Sheriff, R. E., 1990, Applied Geophysics, Cambridge University Press, Cambridge (1990), p. 283-609.

Thoman, M., Zonge, K., and Liu, D., 1998, Geophysical case history of North Silver Bell, Pima County, Arizona-A supergene-enriched porphyry copper deposit: Northwest Mining Association, p. 42.

Tikhonov, A., and Arsenin, V. Y., 1977, Solutions of ill-posed problems: Winston & Sons, Washington, DC.

Titley, S. R., 1982, Advances in Geology of the Porphyry Copper Deposits: Southwestern North America, University of Arizona Press, Tucson, Arizona.

Van Blaricom, R., 1992, Practical geophysics II for the exploration geologist, Northwest Mining Association.

White, R., Collins, S., and Loke, M., 2003, Resistivity and IP arrays, optimised for data collection and inversion: Exploration Geophysics, v. 34, no. 4, p. 229-232.

Wightman, W., Jalinoos, F., Sirles, P., and Hanna, K., 2004, Application of geophysical methods to highway related problems, Federal Highway Administration, Central Federal Lands Highway Division, Lakewood, Publication No. FHWA-IF-04-021, September 2003.

Yoshioka, K., 3-D forward modeling and inversion of IP data, *in* Proceedings Consortium for Electromagnetic Modeling and Inversion Proceedings of 2000 Annual Meeting 2000, p. 377-404.

Yoshioka, K., and Zhdanov, M. S., 3-D Inversion of IP data based on localized quasi-linear approximation, *in* Proceedings Consortium for Electromagnetic Modeling and Inversion Proceedings of 2003 Annual Meeting 2002, p. 273-315.

Yoshioka, K., and Zhdanov, M. S., Nonlinear regularized inversion of array induced polarization data based on the Cole-Cole model, *in* Proceedings Consortium for Electromagnetic Modeling and Inversion Proceedings of 2003 Annual Meeting 2003, p. 201-224.

Zhdanov, M. S., 2002, Geophysical inverse theory and regularization problems, volume 36 of Method in Geochemistry and Geophysics: Elsevier.

Zhdanov, M. S., 2008, Generalized effective-medium theory of induced polarization: Geophysics, v. 73, no. 5, p. F197-F211.

Zhdanov, M. S., 2009, Geophysical electromagnetic theory and methods, volume 36 of Method in Geochemistry and Geophysics: Elsevier.

Zhdanov, M. S., Dmitriev, V. I., Fang, S., and Hursåan, G., 2000, Quasi-analytical approximations and series in electromagnetic modeling: Geophysics, v. 65, no. 6, p. 1746-1757.

Zhdanov, M. S., and Fang, S., 1996, Three-dimensional quasi-linear electromagnetic inversion: Radio Science-Washington, v. 31, p. 741-754.

Zhdanov, M. S., and Tartaras, E., 2002, Three-dimensional inversion of multitransmitter electromagnetic data based on the localized quasi-linear approximation: Geophysical Journal International, v. 148, no. 3, p. 506-519.

Zhu, Y., and Li, Y., 3-D inversion of induced polarization data in wavelet domain, *in* Proceedings 2004 SEG Annual Meeting 2004.

Zonge, K., 2003, State of the Art in IP and Complex Resistivity.

Zonge, K. L., and Wynn, J. C., 1975, Recent advances and applications in complex resistivity measurements: Geophysics, v. 40, no. 5, p. 851-864.